

Air Force Institute of Technology

AFIT Scholar

---

Theses and Dissertations

Student Graduate Works

---

12-8-2008

## Nondestructive Evaluation of Aircraft Composites Using Terahertz Time Domain Spectroscopy

Christopher D. Stoik

Follow this and additional works at: <https://scholar.afit.edu/etd>



Part of the [Materials Chemistry Commons](#), and the [Other Materials Science and Engineering Commons](#)

---

### Recommended Citation

Stoik, Christopher D., "Nondestructive Evaluation of Aircraft Composites Using Terahertz Time Domain Spectroscopy" (2008). *Theses and Dissertations*. 2433.  
<https://scholar.afit.edu/etd/2433>

This Dissertation is brought to you for free and open access by the Student Graduate Works at AFIT Scholar. It has been accepted for inclusion in Theses and Dissertations by an authorized administrator of AFIT Scholar. For more information, please contact [richard.mansfield@afit.edu](mailto:richard.mansfield@afit.edu).



**NONDESTRUCTIVE EVALUATION OF AIRCRAFT  
COMPOSITES USING TERAHERTZ TIME DOMAIN  
SPECTROSCOPY**

DISSERTATION

Christopher D. Stoik, Lieutenant Colonel, USAF  
AFIT/DS/ENP/09-D02

**DEPARTMENT OF THE AIR FORCE  
AIR UNIVERSITY**

**AIR FORCE INSTITUTE OF TECHNOLOGY**

**Wright-Patterson Air Force Base, Ohio**

APPROVED FOR PUBLIC RELEASE; DISTRIBUTION UNLIMITED

The views expressed in this dissertation are those of the author and do not reflect the official policy or position of the United States Air Force, Department of Defense, or the United States Government.

AFIT/DS/ENP/09-D02

**NONDESTRUCTIVE EVALUATION OF AIRCRAFT COMPOSITES  
USING TERAHERTZ TIME DOMAIN SPECTROSCOPY**

DISSERTATION

Presented to the Faculty

Graduate School of Engineering and Management

Air Force Institute of Technology

Air University

Air Education and Training Command

In Partial Fulfillment of the Requirements for the

Degree of Doctor of Philosophy

Christopher D. Stoik, BS, MS

Lieutenant Colonel, USAF

December 2008

APPROVED FOR PUBLIC RELEASE; DISTRIBUTION UNLIMITED

**NONDESTRUCTIVE EVALUATION OF AIRCRAFT COMPOSITES  
USING TERAHERTZ TIME DOMAIN SPECTROSCOPY**

Christopher D. Stoik, BS, MS  
Lieutenant Colonel, USAF

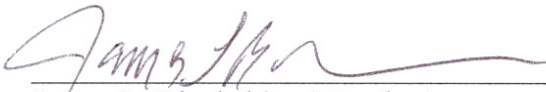
Approved:



Matthew J. Bohn (Chairman)

2 Dec 08

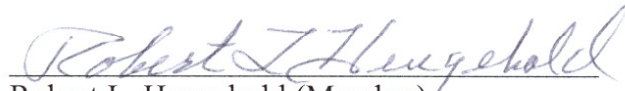
Date



James L. Blackshire (Member)

2 Dec 08

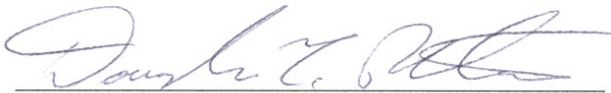
Date



Robert L. Hengehold (Member)

2 Dec '08

Date



Douglas T. Petkie (Member)

2 Dec 08

Date

Accepted:



Marlin U. Thomas (Dean)

18 Dec 08

Date

## **Abstract**

Terahertz (THz) time domain spectroscopy (TDS) was assessed as a nondestructive evaluation technique for aircraft composites. Material properties of glass fiber composite were measured using both transmission and reflection configuration. The interaction of THz with a glass fiber composite was then analyzed, including the effects of scattering, absorption, and the index of refraction, as well as effective medium approximations. THz TDS, in both transmission and reflection configuration, was used to study composite damage, including voids, delaminations, mechanical damage, and heat damage. Measurement of the material properties on samples with localized heat damage showed that burning did not change the refractive index or absorption coefficient noticeably; however, material blistering was detected. Voids were located by THz TDS transmission and reflection imaging using amplitude and phase techniques. The depth of delaminations was measured via the timing of Fabry-Perot reflections after the main pulse. Evidence of bending stress damage and simulated hidden cracks was also detected with terahertz imaging.

## Acknowledgements

First, I would like to thank my advisor, Lt Col Matt Bohn, for his guidance in this research, offering skillful advice with the laboratory experimental setup and providing expert scientific insight in helping me to resolve research issues. I would also like to thank Dr. Jim Blackshire of AFRL/RXLP for sponsoring this work and for providing us with representative aircraft composite samples which were essential to the research. In addition, I would like to thank Abel Nunez for his help with image processing and to Jeremy Johnson and AFRL/RXLP for the ultrasound and x-ray images. Thanks to Col Brent Richert and my parents for their encouragement to return to school and earn this degree and to my mother for helping to proofread this dissertation.

I would like to thank Epiphany Lutheran Church for its spiritual support along the way. I am very grateful for the birth of my two children who have been an inspiration to me and represent promise for the future. Most of all, I would like to thank my wife for her patience and understanding during the difficult days and nights when I was studying, researching, and writing. I also thank her for her strength in enduring an uncomfortable work situation for 4 years.

## Table of Contents

Abstract .....	iv
Acknowledgements .....	v
List of Figures .....	ix
List of Tables .....	xiv
1. Introduction .....	1
1.1 Background .....	2
1.2 Problem Statement .....	3
1.3 Research Objectives .....	4
1.4 Experimental Approach .....	5
1.5 Assumptions/ Limitations .....	5
1.6 Overview .....	6
2. Theory and Background .....	8
2.1 THz Pulse Generation .....	8
2.1.1 Photoconductive Antennas .....	9
2.1.2 Optical Rectification in Nonlinear Media .....	11
2.2 THz Pulse Detection .....	13
2.2.1 Photoconductive Antennas .....	13
2.2.2 Electro-Optic Sampling in Crystals .....	14
2.3 Terahertz Time Domain Spectroscopy System .....	16
2.3.1 Femtosecond Laser .....	18
2.3.2 THz Beam Optics .....	18
2.3.2.1 Substrate Lens .....	19
2.3.2.2 Off-Axis Parabolic Mirrors .....	20
2.3.2.3 Gaussian Beams .....	20
2.3.2.4 Gaussian Beam Expansion .....	22
2.3.3 Scanning Optical Delay Line .....	23
2.3.4 Raster Scanner .....	23
2.3.5 Lock-in Amplifier .....	24
2.4 THz TDS Data Analysis on Composites .....	25
2.4.1 Material Parameter Estimation .....	27
2.4.2 Drude Model .....	28
2.4.3 Scattering .....	29
2.4.4 Effective Medium Approximations .....	34
2.4.5 Imaging .....	35
2.4.6 Image Processing .....	37
2.5 THz TDS Literature Review .....	39



2.5.1	Composites.....	39
2.5.2	Ceramics .....	41
2.5.3	Paint Thickness over Metallic Surfaces .....	42
2.5.4	Semiconductors.....	43
2.5.5	Measuring Material Properties with THz Radiation.....	44
2.5.5.1	Transmission Mode Measurement Technique.....	44
2.5.5.2	Literature Summary of THz Material Parameter Measurements.....	47
2.5.6	THz TDS for NDE .....	49
3.	Material Parameter Estimation with Terahertz TDS.....	51
3.1	THz TDS System Characterization.....	51
3.1.1	THz TDS Output Specifications .....	52
3.1.2	Water Vapor Absorption Spectra.....	54
3.1.3	THz Pulse and Spectrum Modeling .....	55
3.1.4	System Setup Challenges .....	58
3.2	Transmission Mode Measurements .....	59
3.2.1	Calculation Technique .....	60
3.2.2	Measurement Results on Various Materials .....	62
3.2.3	Effective Medium Approximation and Scattering Analysis .....	66
3.2.4	Material Parameter Calibration.....	71
3.2.4.1	Drude Model Predictions.....	71
3.2.4.2	Silicon Measurements .....	73
3.2.5	Fabry-Perot Resonance Removal Techniques .....	75
3.3	Reflection Mode Material Parameter Measurements .....	79
3.3.1	Calculation Technique .....	80
3.3.2	Practical Approximation of Material Parameters .....	82
3.3.3	Other Material Parameter Measurements .....	84
3.4	Burn Diagnostics Using THz TDS .....	87
3.4.1	Transmission Mode.....	88
3.4.2	Reflection Mode.....	90
4.	THz Imaging for Nondestructive Evaluation.....	92
4.1	Sample Preparation .....	92
4.2	Transmission Mode Setup.....	93
4.3	THz Beam Propagation and Modeling .....	94
4.3.1	Spot Size Minimization.....	95
4.3.2	THz Beam Measurements.....	97
4.4	Imaging of Composites with Transmission Setup .....	99
4.4.1	THz TDS Thickness Measurements .....	99
4.4.2	Image Processing Comparison.....	100
4.4.3	2-D Imaging Results .....	102
4.4.3.1	Imaging of Burn Damage .....	104
4.4.3.2	Imaging of Bending Damage.....	108
4.4.3.3	Imaging of Hidden Defects .....	109

4.4.4	Depth of Delamination Analysis.....	110
4.5	Reflection Mode Imaging of Composites .....	113
4.5.1	Thickness Calibration .....	113
4.5.2	2-D Imaging Results .....	114
4.5.2.1	Imaging of Burn Damage .....	115
4.5.2.2	Imaging of Bending Damage.....	118
4.5.2.3	Imaging of Hidden Defects .....	118
4.5.2.4	Imaging and Analysis of Entire Panels .....	119
4.5.2.5	Paint Thickness Approximations.....	122
4.5.3	Depth of Delaminations Analysis .....	123
5.	Conclusions and Recommendations .....	128
5.1	Major Research Contributions .....	128
5.2	Conclusions.....	128
5.3	Future Work .....	132
	Bibliography .....	137
	Vita .....	145

## List of Figures

Figure	Page
1. Electromagnetic Spectrum [14].	1
2. Photoconductive switch [48].	9
3. Diagram of optical rectification.	12
4. Setup for EO detection of THz pulses.	15
5. THz TDS transmission mode setup using PC antennas.	17
6. Diagram showing the components of a Gaussian beam [14].	21
7. (a) THz pulse time waveform. (b) THz frequency spectrum [26].	25
8. Components of the THz waveform at the detector in the time and frequency domain [14].	26
9. Waveforms resulting from the collection of data at the THz detector [14].	27
10. Diagram showing incident and scattered ray upon an infinitely long cylinder.	33
11. An inhomogeneous system is replaced by a (virtual) effective medium.	34
12. Transmission and reflection of a THz wave through a planar, homogeneous material.	45
13. THz TDS setup for material parameter measurements.	52
14. THz TDS scan of ambient air: (a) THz time domain pulse, (b) THz phase spectrum, and (c) THz amplitude spectrum.	54
15. Comparison of a Gaussian modeled THz pulse through air and glass fiber compared to THz TDS measurements for air and glass fiber in the (a) time domain and (b) frequency domain.	57
16. THz pulse measured with photoconductive (PC) switch detector: (a) time domain pulse and (b) frequency domain spectrum compared to electro-optic detector.	59
17. THz TDS results through air & space shuttle tile: (a) THz pulse and (b) amplitude spectra.	63
18. Space shuttle tile calculations for (a) index of refraction and (b) absorption coefficient with a calculation for $\alpha_{\max}$ .	63
19. THz pulse measured through glass fiber: (a) time domain, (b) frequency domain, (c) index of refraction, and (d) absorption coefficient with $\alpha_{\max}$ included.	66

20. THz TDS material parameter measurements using actual thickness measurements from polyimide showing (a) index of refraction and (b) absorption coefficient. ....	67
21. Scattering coefficient calculation for glass fiber in the THz frequency range. ....	69
22. (a) Extinction coefficient estimation on glass weave assuming an air-glass index mixture. (b) Comparison of the Bruggeman EMA for glass fiber extinction using polyimide and glass weave data vs. actual glass fiber extinction data. (c) Scattering coefficient calculations for the air and glass weave mixture. (d) Comparison of EMA for glass fiber using polyimide and glass weave (scattering removed) vs. glass fiber extinction coefficient.....	70
23. Material parameter measurements on a silicon wafer: (a) THz pulse showing FP reflections, (b) THz spectrum, (c) index of refraction, and (d) absorption coefficient. ....	73
24. Material parameter measurements on high resistivity silicon: (a) THz pulse, (b) THz spectrum, (c) index of refraction, and (d) absorption coefficient. ....	74
25. Material parameter measurements on 6 mm thick float zone (FZ) silicon: (a) THz pulse, (b) THz spectrum, (c) index of refraction, and (d) absorption coefficient. ....	75
26. Diagrams showing the removal of FP oscillations in the time domain: (a) index of refraction with FP oscillations, (b) index of refraction without first 2 FP oscillations, (c) absorption coefficient with FP oscillations, (d) absorption without first 2 FP oscillations. ....	77
27. Iterative process for removal Fabry-Perot etalon effect in frequency domain described by Duvillaret et. al. ....	77
28. Fabry-Perot oscillation removal technique showing the real part of the index of refraction (a) before & (b) removal, followed by the imaginary part of the index of refraction (c) before & (d) after the Fabry-Perot removal technique was applied. ....	78
29. THz TDS reflection mode schematic.....	79
30. Material parameter measurements using reflection configuration on 6 mm thick float zone (FZ) silicon: (a) index of refraction and (b) absorption coefficient. ....	82
31. THz TDS reflection setup for thick FZ silicon: (a) pulses off front and back surface and (b) absorption coefficient using Fourier transform from each pulse. ....	83
32. Diagram showing the geometry of the first Fabry-Perot reflection from the sample in reflection configuration. ....	84
33. THz TDS reflection (a) pulse and (b) spectrum for 1.016 mm high resistivity silicon. Isolation of the (c) front reflected pulse and the (d) back side	

reflected pulse in the time domain. The (e) absorption coefficient for high resistivity silicon measured using the spectrum of the front and back pulse.....	85
34. Plot of the (a) THz pulses reflected from the front and back of a glass fiber coupon. Absorption coefficient for the glass fiber (b) without filtering and (c) with filtering. ....	87
35. THz TDS (a) pulse and (b) amplitude spectra for air reference and coated glass fiber. (c) Index of refraction and (d) absorption coefficient measurements for coated glass fiber in the THz frequency range.....	88
36. THz TDS material parameter measurements using actual thickness measurements for burn damage areas showing (a) indices of refraction and (b) absorption coefficients. ....	89
37. THz TDS material parameter measurements, assuming the same thickness, for burn damage areas showing (a) indices of refraction and (b) absorption coefficients.....	90
38. Comparison of the reflected signal from a coated and uncoated sample, showing the (a) time domain and (b) frequency spectrum returns. ....	91
39. Photograph showing the 5 glass fiber samples: (1) thickness calibration sample, (2) & (3) burn samples, (4) mechanical stress sample, and (5) hidden defect sample showing the hidden location of two of the eight defects. ....	93
40. THz TDS Setup for Imaging Composites in Transmission Mode.....	94
41. Diagram showing the transmission optical system with THz beam focusing on sample at 1 THz. ....	96
42. Diagram showing the reflection optical system with THz beam focusing on sample at 1 THz. ....	97
43. Diagram showing the geometry of the incident and reflected beam off the apparatus for measuring the THz spot size in TDS reflection configuration. ....	99
44. Relative delay of THz pulses for various thicknesses of glass fiber sample, including those that were etched (*). ....	100
45. THz image of a 12.5 mm diameter circle etched in glass fiber showing (a) the original 1X1 mm pixel image, (b) image after MATLAB 'interp' function, (c) image after zero-padding 10 times in the spatial frequency domain, and (d) final image after applying MATLAB 'interp' function to part (c). (e) Comparison of (c) with 1/10 <sup>th</sup> scale pixel image. ....	101
46. Image comparison showing the (a) the zero-padding technique (10 times) and the (b) zero-padding technique (4 times) with the addition of a Wiener filter. ....	102
47. THz TDS transmission images showing a section of the glass fiber that had been milled to two different thicknesses using peak pulse amplitude (a) and peak pulse position (b) techniques. A picture of the scan area on the calibration sample (c). ....	103

48. THz images formed by summing the area under the curve of the amplitude spectrum within a given frequency range for each pixel: (a) 0.1 – 1.3 THz, (b) 0.5 – 0.7 THz, (c) 0.7 – 0.9 THz. ....	104
49. THz TDS images and photos for three burn areas on glass fiber samples: (a), (d) 440°C for 4 minutes; (b), (e) 430°C for 6 minutes; and (c), (f) 425°C for 20 minutes. ....	105
50. THz TDS (a) pulse image and (b) amplitude spectra for undamaged glass fiber sample and for an area with burn damage (440°C for 4 minutes). (c) THz TDS amplitude image of high resistivity silicon. ....	106
51. THz TDS image showing bend damage across the central bend axis (a). Photographs of the (b) front side of the composite strip showing the scan area with the location of the taped 'X' and the (c) back side showing the location of the cracking and buckling and the hexagonal structure. (d) Ultrasound image of the bend damage. ....	108
52. THz TDS images showing 3 mm diameter milled area hidden between two glass fiber strips using (a) peak pulse amplitude and (b) peak pulse position. Linear slit void (6 mm length) (c) also hidden between two strips of glass fiber. The final picture is an x-ray computed tomography scan of the laminated sample showing the hidden circular and slit voids in the sample. ....	109
53. THz pulses after propagating through (a) laminated and delaminated portions of a glass fiber strip. (b) Autocorrelation of each of the two pulses showing the approximate location of Fabry-Perot reflections. Thz pulse propagation in the opposite direction showing pulses and their autocorrelations (c), (d). ....	111
54. (a) Diagram showing the main pulse and the first Fabry-Perot reflection in transmission configuration. (b) A chart showing the relative amplitude of the first Fabry-Perot reflection to the main pulse after traveling through various thicknesses of composite. (c) A photograph showing the delamination. ....	112
55. THz TDS reflection images showing a section of the glass fiber that had been milled to two different thicknesses using peak pulse amplitude (a) and peak pulse position (b) techniques. The final image (c) shows a thickness estimation for a separate scan. ....	114
56. THz TDS reflection images for burn damage from heating at 440°C for 4 minutes for (a) peak pulse amplitude and (b) peak pulse position. Pulse return from the right side of the bubble showing the double pulse return (c). X-ray computed tomography image showing a side profile of the large burn blister (d). ....	116
57. THz TDS reflection images showing the (a) minimum peak amplitude for burning at 430°C for 6 minutes and the (b) peak pulse amplitude for burning at 425°C for 20 minutes. ....	117
58. THz TDS reflection image using the amplitude of frequencies (1.2 – 1.4 THz) showing bend damage across the central bend axis. ....	118

59. THz TDS reflection image showing 3 mm diameter milled area hidden between two glass fiber strips using the amplitude of the Fabry-Perot reflection from the void. ....	119
60. THz TDS reflection setup scan on entire panel with puncture hole (4.5 mm diameter) and two burn blisters. Images were constructed using the (a) minimum peak pulse amplitude, (b) maximum peak pulse position, and (c) the frequency spectrum amplitude added under the curve (1.4 – 1.6 THz). THz pulses reflected from coated surface and partially uncoated burn blister (d).....	120
61. THz images constructed using the (a) peak pulse amplitude and (b) peak pulse position of a panel with its coating dissolved away by butanone. ....	121
62. THz TDS (a) time domain plots and (b) frequency spectra for a coated and uncoated surface of an aircraft panel. ....	122
63. THz TDS reflection configuration plots showing the (a) time domain pulse with a double peak and the (b) THz amplitude spectrum. ....	123
64. (a) Diagram of a delaminated sample showing the first Fabry-Perot reflection in reflection configuration. (b) A chart showing the relative strength of the first Fabry-Perot reflection after traveling through various thicknesses of glass fiber composite before the delamination. (c) A chart showing the relative strength of the first Fabry-Perot reflection from discontinuities including both glue-glass fiber (G-GF) and air-glass fiber (A-GF). ....	124
65. THz TDS time domain plots showing reflections from discontinuities: (a) air and (b) adhesive. ....	125
66. Fourier deconvolution of the discontinuities present in a glass fiber sample laminated at various thicknesses: (a) 0.23 mm, (b) 0.46 mm, (c) 0.69 mm, (d) 0.92 mm, (e) 0.92 mm delaminated, and (f) no lamination. Fourier deconvolution with the TDS system characteristics subtracted are shown next. The various thicknesses were measured in the opposite direction: (g) 0.23 mm, (h) 0.23 mm delaminated, (i) 0.46 mm, (j) 0.69 mm, (k) 0.92 mm, and (l) no lamination. ....	126
67. Comparison of the calculated time for F-P reflections through glass fiber to the measured autocorrelation values measured in both transmission and reflection configuration. ....	127
68. Summary charts showing the relative amplitude of the first Fabry-Perot reflection to the main pulse after traveling through various thicknesses of glass fiber composite in (a) transmission configuration and (b) reflection configuration. ....	132
69. Comparison of various types of glass fiber damage/alterations between transmission and reflection configuration. ....	133

## List of Tables

Table	Page
1. THz Time Domain Spectrometer specifications and measurements. ....	53
2. Absorption spectrum rotational transitions for water vapor between 0.2 – 2.4 THz [82].....	55
3. List of Specifications for Ekspla photoconductive switch components. ....	58
4. Sources of error for THz material parameter measurements. ....	62
5. Summary of results for effective medium approximations on space shuttle tile at 0.5 THz. ....	64
6. Drude Model parameters and predictions for Silicon at 1 THz. ....	72
7. Ekspla measurements at the exit of the silicon hemispherical lens. ....	95
8. Comparison of diffraction-limited spot sizes with THz beam optical design focus spot sizes for the transmission configuration. ....	96
9. Comparison of diffraction-limited spot sizes with THz beam optical design focus spot sizes for the reflection configuration. ....	97



# Nondestructive Evaluation of Aircraft Composites Using Terahertz Time Domain Spectroscopy

## 1. Introduction

Terahertz (THz) radiation can be defined as the region of the electromagnetic spectrum with frequencies between 0.1 THz and 10 THz or with wavelengths between 3 mm and 30  $\mu\text{m}$ . The THz “gap”, as shown in Figure 1, falls between the microwave region and the infrared/optical region. Microwave electronic devices are typically comparable in size to the wavelength of the radiation and support single-mode or low-order mode guided waves. In contrast, optical and infrared devices have dimensions much larger than a wavelength and often support beams containing many modes. The merging of laser and optics technology with micro chip electronics technology has been instrumental in the development of THz devices and the advancement of THz research.

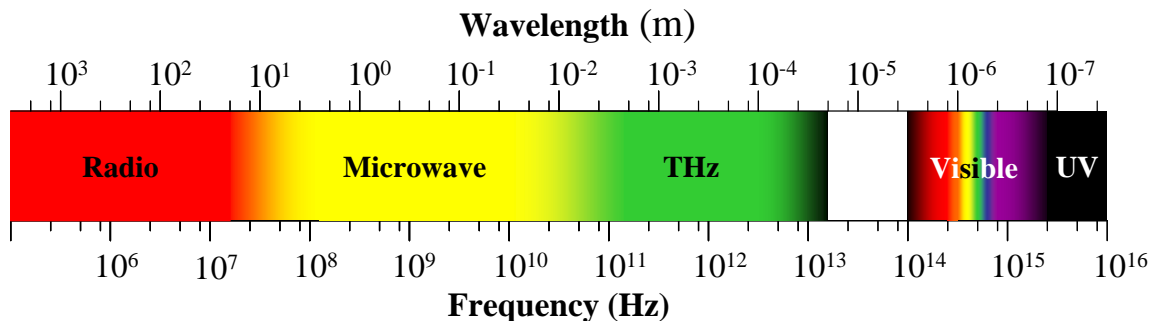


Figure 1. Electromagnetic Spectrum [14].

## 1.1 Background

With the rapid advances in the development of laser technology, nonlinear optics and optoelectronic techniques for the production and measurement of terahertz radiation have proliferated. One of the earliest and most promising of these techniques is terahertz time-domain spectroscopy (THz TDS), a method which relies on the generation of broadband electromagnetic transients using ultrafast laser pulses. Several novel measurement capabilities have become practical, including time-resolved techniques like the optical pump – THz probe measurement, THz emission spectroscopy, and THz correlation spectroscopy. The first reported use of THz TDS for imaging was reported in 1995 and this work has sparked a flood of interest and suggested a range of new applications for THz “T-ray” imaging [48]. It has even received media attention recently in the novel *Games of State*, by Tom Clancy [15].

Composite materials such as fiberglass, Kevlar, and carbon fiber have high strength to weight ratios and are increasingly being used as structural components in high performance military aircraft [89]. The navy’s F/A-18A/B and the F/A-18E/F structural weights are composed of 10% and 19% composites, and approximately 24% of the F-22’s structural weight is composite in origin. The F-35 Joint Strike Fighter will also have a high percentage of its weight made up of composites.

Fiber composites not only impart increased strength to aircraft structures, but also improve aerodynamic performance, increase safety, and reduce corrosion. However, composites can be weakened by various defects that are created during either fabrication or during the lifecycle of the aircraft. In the layer build-up stage of the manufacturing process, foreign debris can become embedded within the composite layers, and voids can

be formed by air bubbles or large gaps between the fiber weave. Defects that are caused by foreign debris or voids decrease the layer adhesion and the overall strength of a composite component. Current quality control methods are incapable of finding these defects until curing has been completed, requiring that the component be reworked or thrown out and increasing the cost of part production. Additionally, routine maintenance of in-service composite materials requires the application of relatively complex inspection and repair techniques, which often have to be performed in the field.

New techniques are being explored to improve the efficiency of composite part inspection during construction and repair. THz radiation offers potential efficiency improvements, because it has the unique ability to penetrate composites and identify foreign debris and other defects such as delaminations, air bubbles, and heat damage. THz would offer a non-invasive, non-contact, non-ionizing way of assessing composite part condition and could help overcome the shortcomings of other nondestructive evaluation (NDE) techniques such as x-rays, ultrasound, video inspection, eddy currents, and thermographic techniques.

## **1.2 Problem Statement**

Significant progress has been made recently in the development of the sources and technology for THz imaging, sensing, and spectroscopic and communications applications, but the technology still remains limited compared to that used for the microwave and optical regions of the spectrum. THz technology is being used in an increasingly wide variety of applications including: information and communications technology; biology and medical sciences; homeland security; quality control of food and

agricultural products; global environment monitoring; ultrafast computing; and NDE among others. Effective NDE can be performed with a THz imaging system; however, a THz imaging system demands a high repetition scan rate and a high average power for favorable signal-to-noise ratios. To fully take advantage of this emerging technology will require more compact, efficient, and higher power sources. This research effort attempts to take advantage of commercially available THz sources in an effort to more effectively characterize and image composite materials.

Innovative solutions for quality control of composite materials during the manufacturing process and subsequent routine maintenance are needed by the Air Force to save time and lower cost. As a NDE technique, THz imaging has the potential to be an effective method of quality control and maintenance inspection of composites. Although techniques have been developed to measure material properties at THz frequencies, work still needs to be done to understand and characterize the electromagnetic interaction of THz with various materials. The optical and electrical properties of composites need to be fundamentally understood to improve imaging techniques for NDE. Additionally, the capability of THz TDS in both transmission and reflection configuration should be tested on representative damage samples for effectiveness.

### **1.3 Research Objectives**

The objective of this dissertation is to evaluate THz TDS for nondestructive testing and evaluation of aircraft composites by using theory, modeling, and experimentation to analyze the interaction of THz radiation with composite materials. An additional objective is to show that THz imaging shows promise for NDE, especially

when imaged with a high average power, high repetition rate source and a fast scanning and collection technique for inspecting the sample.

## **1.4 Experimental Approach**

The first step of this research was to set up a THz TDS system in transmission configuration using a photoconductive switch for the transmitter and an electro-optic crystal for the receiver. Using this setup initially, data was collected to make estimates of optical and electrical parameters for semiconductors and various composite materials, such as space shuttle foam insulation and aircraft glass fiber composites. The composite material parameters could then be used, along with effective medium theory and scattering theory, to describe the interaction of the THz radiation with the sample. Then a series of THz images, formed with a raster scan pattern, and depth measurements were collected on samples prepared with various forms of representative damage.

The next step in the experiment was to change the THz TDS system to a reflection configuration. With this setup, the material parameter measurements were measured on the same samples used in the transmission experiments. Finally, reflection mode images and depth measurements were taken on the same damage samples for a comparison of the two scan methods.

## **1.5 Assumptions/ Limitations**

The variety of aircraft composite samples available for this research was somewhat limited, but encompassed a representative set of damages that aircraft composites could encounter. Additionally, the ability to obtain the limited set of

representative aircraft damage samples allowed this research to be unique and interesting. The research was restricted to glass fiber composites, however, because of the inability of THz radiation to penetrate other composites like carbon fiber. It was also difficult and expensive to obtain semiconductor samples with low resistivities, due to the manufacturers' reluctance to sell wafers in small quantities. The assumption was made that a high resistivity wafer was sufficient to calibrate a THz TDS system. Another of our limitations was that we had limited knowledge about the properties, structure, and volume concentration of the composite constituents. This resulted in making assumptions for the effective medium and scattering approximations.

The lab setup that was used was limited in its ability to collect THz TDS data at a fast enough rate to be considered operationally useful. The assumption was made that the data we collected to make material parameter measurements and to form images was for a proof of concept demonstration and that other organizations are developing the means to rapidly scan large samples in short amounts of time. Commercially available THz, optical, and mechanical components were sufficient to conduct this research, but customized components and techniques could allow the THz beam to be more tightly focused onto the sample and scanned at a faster rate to maximize defect detection.

## **1.6 Overview**

The following chapters of this dissertation outline the theory, literature review, experimental setups, data collection and analysis, and imaging of composite materials with THz TDS in various configurations. Chapter 2 begins by describing the theory for the emitter and detector technology used in this research, followed by a description of the

components of the THz TDS system. The next section describes data analysis, including material parameter estimation, scattering, and imaging. The chapter closes with a summary of some of the recent findings in the literature regarding the use of THz for NDE.

Chapter 3 describes the data collection, analysis, and results of the material parameter estimation of the composite materials studied in this dissertation. The first section explains the setup and characterization of the THz TDS data collection system. This is followed by the analysis of material parameters collected using the transmission mode, including a comparison with the Drude Model, Fabry-Perot cancellation techniques, and effective medium and scattering approximations. The next section is dedicated to making the same material parameter calculations using THz TDS in reflective mode. The last section concludes with an analysis of THz TDS material parameter measurements on burn damage as a potential NDE technique.

In chapter 4, the imaging and analysis of composite damage is the focus, using both transmission and reflection configurations. The first section explains the optimization of the THz optical system design for a minimized spot size and the image processing technique used during post processing. The next section shows the results of transmission mode imaging of the damage samples and a depth of delamination analysis. The last section of chapter 4 shows the results of 2-D imaging and depth analysis on the same samples using the reflection setup. The last chapter shows a summary of the results and recommendations for future THz research.

## 2. Theory and Background

In order to estimate the optical and electrical parameters of a material using THz TDS or image that material using THz TDS, it is necessary to establish the theoretical background on the generation and detection of THz radiation as well as measurement techniques. This chapter lays the foundation required to explore the properties of composite materials at THz frequencies and the insight to investigate THz TDS as a NDE technique.

### 2.1 THz Pulse Generation

In recent years scientists have developed numerous techniques for generating THz radiation in an effort to explore this spectral region. This research dealt solely with pulsed THz sources instead of continuous wave sources. A traditional, transient current technique using a photoconductive switch was used exclusively as the THz emitter. Optical rectification, a traditional nonlinear technique, was also demonstrated in the lab as a means to generate THz, but was not used in data collections for this research. Currently, the average power generated from a typical photoconductive switch is less 1  $\mu\text{W}$ , while the peak power from optical rectification may reach up to 1  $\mu\text{W}$  [81]. Larger area photoconductive switching devices have yielded electric fields as high 150 kV/cm and a new technique, using a four-wave mixing process, showed a record high field strength of 400 kV/cm [7, 88]. A recent publication demonstrated a high average power of 0.25 mW from a single cycle THz pulse using an optical rectification technique with a lithium niobate crystal [31].



## 2.1.1 Photoconductive Antennas

Photoconductive (PC) switches are composed of metallic striplines deposited on a semiconductor material. PC switches, also called Auston switches, are based on the pioneered work by Auston in the mid-1970s, using a mode-locked Nd:glass laser to pump high-resistivity silicon [48]. When an optical pulse, such as a femtosecond laser, strikes the semiconductor at a wavelength above the bandgap, electron (holes) are generated in the conduction (valence) band. The carriers are then accelerated in phase by the bias field toward the anode, resulting in a pulsed photocurrent in the PC antenna. Time-varying current occurs in the subpicosecond regime and thus emits a subpicosecond electromagnetic transient or THz pulse [48]. A diagram of a photoconductive switch is shown in Figure 2.

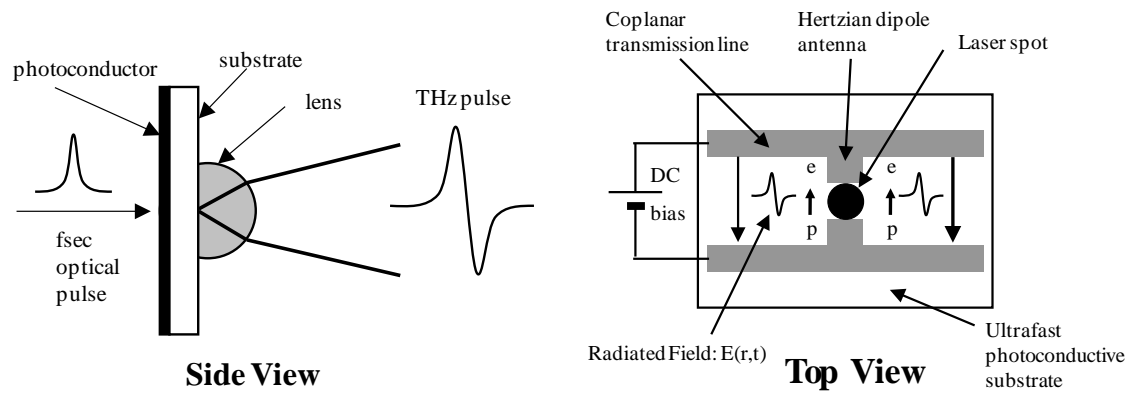


**Figure 2. Photoconductive switch [48].**

For an elementary dipole antenna in free space, the radiated electric field  $E(r, t)$  at a distance  $r$  and the time  $t$  are described by

$$E(r, t) = \frac{l_e}{4\pi\epsilon_0 c^2 r} \frac{\partial J(t)}{\partial t} \sin \theta \quad (1)$$

where  $J(t)$  is the current in the dipole,  $l_e$  is the effective length of the dipole,  $\epsilon_0$  is the dielectric constant of free space,  $c$  is the speed of light in a vacuum, and  $\theta$  is the angle from the direction of the dipole. The THz radiation amplitude is proportional to the length of the dipole and the time derivative of the transient photocurrent. The photocurrent density is described by

$$j(t) \propto I(t) \otimes [n(t)qv(t)] \quad (2)$$

where  $\otimes$  denotes the convolution product,  $I(t)$  is the optical intensity profile, and  $q$ ,  $n(t)$ , and  $v(t)$  are the charge, density, and velocity of photocarriers. The dynamics of photogenerated free carriers in a semiconductor is well described by the classical Drude model. According to the Drude model, the average velocity of free carriers follows the differential equation

$$\frac{d v(t)}{dt} = -\frac{v(t)}{\tau} + \frac{q}{m} E(t) \quad (3)$$

where  $\tau$  is the momentum relaxation time and  $m$  is the effective mass of the carrier. The current density is represented by  $n(t)qv(t)$  which is the impulse response of the PC antenna. Most of the THz pulse is emitted from the substrate side. This is based on the antenna theory that shows that a dipole antenna on the surface of a dielectric material emits roughly  $\epsilon^{3/2}/2$  times more power to the dielectric material than to the air, where  $\epsilon$  is the relative dielectric constant of the substrate [67].

In a PC antenna, properties such as a high electron mobility and a high breakdown voltage should be maximized. Using a semiconductor source with a short carrier lifetime is not a requirement to generate THz. Materials are desired which have a high resistivity because a high voltage is applied across the striplines and a low current is important to

minimize the heat. Faster electron mobilities lead to faster accelerations and higher THz fields. Two of the most often used substances are low temperature grown gallium arsenide (LT-GaAs) and radiation-damaged silicon-on-sapphire (RD-SOS). The PC switch design used for this research is LT-GaAs, which has a high electron mobility, high resistivity, and high breakdown voltage. The amount of excess arsenic in the GaAs can be controlled during epitaxial growth to regulate the carrier lifetimes (0.3 -100 ps), and longer carrier lifetimes result from using a higher temperature during growth [67].

### 2.1.2 Optical Rectification in Nonlinear Media

Optical rectification was one of the first techniques used to generate THz and has the advantage over photoconductive switches in that its output saturates at much higher pump powers. Optical rectification is a nonlinear optical effect caused by the second order susceptibility  $\chi^{(2)}$  that produces a polarization  $P(t)$  in the material:

$$P(t) = \varepsilon_0 \chi^{(1)} E(t) + \varepsilon_0 \chi^{(2)} E(t) E^*(t) + \varepsilon_0 \chi^{(3)} E^3(t) + \dots \quad (4)$$

where  $\varepsilon_0$  is the dielectric constant in free space and  $E(t)$  is the electric field of the incident light [86]. The electric field can be represented by an amplitude and phase component and its complex conjugate where  $\omega$  is the frequency of the light:

$$E(t) = E_0 e^{i\omega t} + c.c. \quad (5)$$

This second order effect causes the creation of a second harmonic component and a DC component. If the nonlinear material is not phase-matched for the second harmonic then the second harmonic output intensity is low. Since the pump input is pulsed, the DC component will have a broad spectral output which is proportional to the inverse of its

pulse width. For a femtosecond laser this falls in the THz range [67]. An optical rectification diagram is shown in Figure 3.

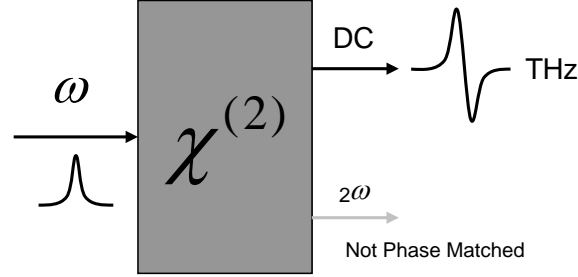


**Figure 3. Diagram of optical rectification.**

The nonlinear material used for optical rectification was zinc telluride (ZnTe). ZnTe is phase matched at the frequency of the Ti:Sapphire laser and at THz frequencies; however, it experiences strong absorption from transverse optical phonons at around 5.3 THz and 11 THz. Optical rectification offers a potentially larger emitted radiation bandwidth than the photoconductive switch. With the optical rectification technique, the generated THz radiation is proportional to the second-order time derivative of the nonlinear polarization  $P(t)$ , and therefore is also proportional to the second-order time derivative of the pump intensity  $I(t)$ . A Fourier transform gives the relationship between the bandwidth of the THz radiation  $\omega$  and frequency distribution of the laser pulse  $I(\omega)$

$$E^{NL}(\omega) \propto \omega^2 G(\omega) P(\omega) \propto \omega I(\omega) \quad (6)$$

where  $G(\omega)$  is the phase matching condition. In the third term of the equation,  $G(\omega)$  is approximated to be proportional to  $1/\omega$  in the high frequency region.

On the other hand, THz generated from a PC switch is proportional to the first order time derivative of the transient current  $J(t)$  and photocarrier density  $N(t)$

$$E^{PC}(t) \propto \frac{\partial J(t)}{\partial t} \propto \frac{\partial N(t)}{\partial t} \propto \frac{\partial \left( \int I(t) dt \right)}{\partial t} \propto I(t). \quad (7)$$

After taking a Fourier transform of the pump intensity term  $I(t)$  in equation 7, a comparison with equation 6 shows that the radiation bandwidth of optical rectification is proportionally larger than a PC switch by the laser pump frequency  $\omega$  [67].

## 2.2 THz Pulse Detection

The two traditional methods of THz pulse detection that were considered for this research were the photoconductive switch and the electro-optic (EO) sampling technique. For this research, we initially tried using LT-GaAs for the THz detector, but then used a ZnTe (110) crystal as an EO detector when the LT-GaAs detector malfunctioned.

### 2.2.1 Photoconductive Antennas

The detection principle of a PC antenna is the inverse process of the THz pulse generation process. In the detection of THz radiation with PC antennas, a current meter is connected instead of a bias voltage. Photocarriers created by a probe pulse are accelerated by the electric field of the incident THz radiation and are detected as current. This temporal change of the input pulse can be traced by changing the arrival time of the optical gate pulse.

The photocurrent  $J(t)$  of the incident radiation at a time delay  $t$  is described by the following equation:

$$J(t) = e\mu \int_{-\infty}^{\infty} E(t')N(t'-t)dt' \quad (8)$$

where  $E(t')$ ,  $N(t')$ ,  $e$ , and  $\mu$  are the incident electric field of the THz radiation, number of photocarriers created, elementary electric charge, and electron mobility, respectively [67]. When the PC antenna is considered as a sampling detector, the temporal increase and decrease of  $N(t)$  should be as short as possible.  $J(t)$  would directly follow  $E(t)$ , as the delay time  $t$  of the optical gate pulse were being scanned, if  $N(t'-t)$  were a delta function.  $N(t)$  can be restricted by numerous factors, such as the gating pulse width and the carrier lifetime and momentum relaxation of photocarriers. This is one of the reasons for selecting semiconductor materials with short carrier lifetimes. The equation for the photocurrent can be transformed into the frequency domain according to the convolution theorem of the Fourier Transform:

$$J(\omega) \propto N(\omega) \cdot E_{THz}(\omega) \quad (9)$$

The terms  $J(\omega)$ ,  $N(\omega)$ , and  $E_{THz}(\omega)$  are Fourier Transforms of each of the components  $J(t)$ ,  $N(t)$ , and  $E(t)$  respectively.

### 2.2.2 Electro-Optic Sampling in Crystals

The coherent detection of a THz pulse with EO crystals is based on the linear EO effect, also known as the Pockel's Effect. The incident THz pulse modifies the refractive index ellipsoid of the EO crystal creating a phase retardation of the linearly polarized optical probe beam. The field strength of the THz pulse can be detected by monitoring the phase retardation of the probe beam. A typical setup for EO detection of THz pulses is shown in Figure 4.

A pellicle beam splitter combines the THz beam and the probe beam so that the polarizations of the THz and probe beam are aligned parallel to the (110) direction of the ZnTe sensor crystal. The phase retardation induced in the EO crystal is given by:

$$\Delta\Gamma = \frac{2\pi}{\lambda} dn_{opt}^3 r_{41} E_{THz} \quad (10)$$

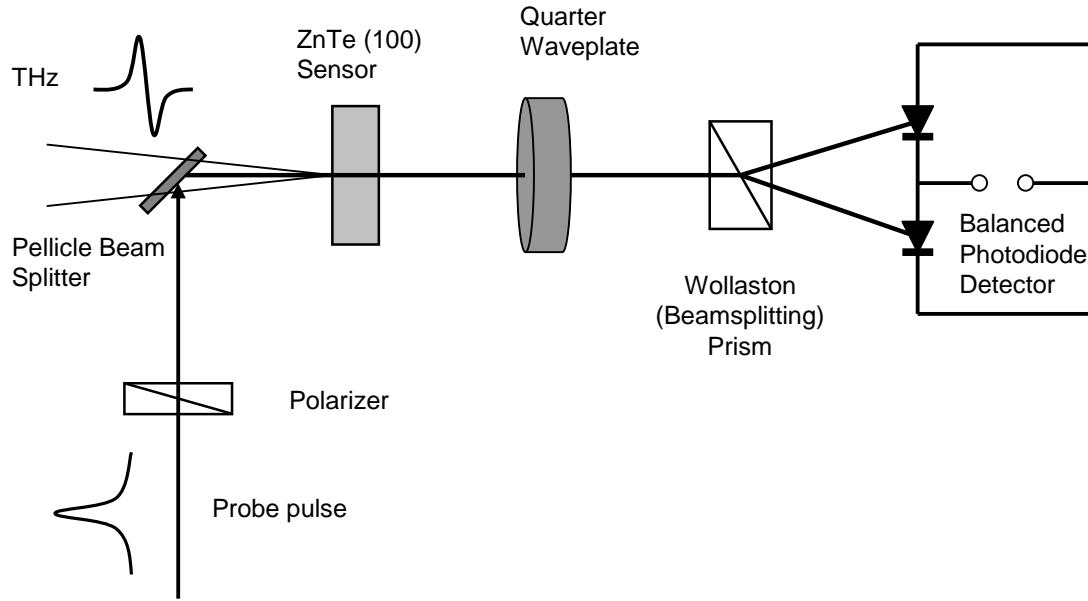


**Figure 4. Setup for EO detection of THz pulses.**

where  $d$  is the EO crystal thickness,  $n_{opt}$  is the group refractive index of the EO crystal at the wavelength of the probe beam, and  $r_{41}$  is the EO coefficient [67]. After the sensor crystal, a quarter-wave plate is used to apply a  $\pi/4$  optical bias to the probe beam. A Wollaston polarizer is then used to convert the THz-radiation-field-induced phase retardation of the probe beam into an intensity modulation between the two mutually orthogonal, linearly polarized beams. A pair of balanced silicon p-i-n photodiodes is fed to a lock-in amplifier referenced to the chopping frequency, which has been generated by turning the emitter on and off at a high frequency ( $\sim 50$  kHz). This technique is called EO

sampling because of the sampling behavior exhibited by the instantaneous response of the Pockel's Effect [67].

### **2.3 Terahertz Time Domain Spectroscopy System**

A THz TDS system is a coherent emission and detection system that emits single-cycle THz pulses and detects them at repetition rates on the order of 100 MHz. The signal is detected in the form of an electric field and the Fourier transform of the pulse signal results in both amplitude and phase spectra over a wide spectral range. It has been recognized that THz TDS is advantageous over Fourier Transform Spectroscopy (FTS), since it gives both phase and amplitude information and avoids the uncertainties caused by the Kramers-Kronig analysis. Additionally, THz TDS can operate with a higher signal-to-noise ratio than FTS, with better time resolution, and with a lower minimum detectable power [67].

The first use of THz TDS for imaging was reported by Hu and Nuss in 1995 [33]. THz TDS, which can be used to probe samples for NDE, can be scanned in two dimensions, in either reflective or transmissive mode. If one adds time information with full field measurements of both phase and amplitude, then samples can be scanned in three dimensions, or what is called THz tomography. In the next sections, the components of a typical THz TDS imaging system will be described.

A diagram of a typical setup for THz TDS in transmission mode using photoconductive switches is shown in Figure 5. A THz TDS system consists of a femtosecond laser, an optical delay line, an optically gated THz transmitter, optics for collimating and focusing the THz beam, the sample to be imaged, an optically gated THz



receiver, and a lock-in amplifier. Various laser optics, including thin lenses and highly reflective metallic-coated mirrors, were chosen to minimize dispersion effects.

The diagram in Figure 5 shows that PC switches can be used for both the THz transmitter and receiver. One could also use a ZnTe crystal for optical rectification for the THz transmitter and the EO sampling technique from Figure 4 for the receiver. The technique of chopping the pump beam increases the signal to noise ratio of the output,

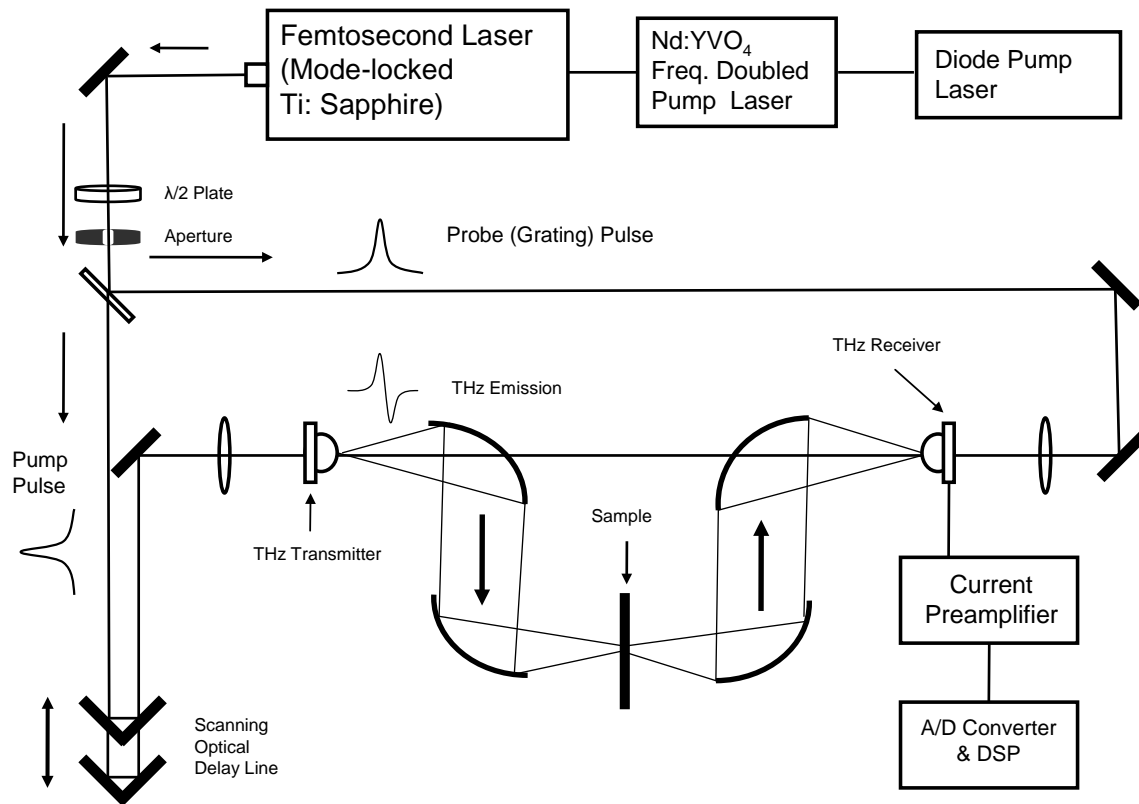


**Figure 5. THz TDS transmission mode setup using PC antennas.**

but also is a source of additional loss to the pump beam. For this experiment we have chosen to use a switching power supply (~50 kHz) for the THz emitter, rather than chopping the pump beam, so that we can operate at a higher frequency and reduce the noise that is experienced at lower frequencies.

### 2.3.1 Femtosecond Laser

A Coherent Mira Model 900-F, Ti:Sapphire, mode-locked laser that operates around 800 nm wavelengths was used for this research. It is optically pumped with a diode-pumped, frequency-doubled Nd:YVO<sub>4</sub> laser. The Ti:Sapphire laser operates with a pulse repetition rate of 76 MHz and has an output power of over 500 mW. The pulse width of the Ti:Sapphire laser was measured with a Pulse Check autocorrelator and autocorrelation widths ranged between 150 – 170 femtoseconds. Since Mira pulses are best described by a  $\text{sech}^2$  function, a factor of 0.648 should be applied to convert observed autocorrelation widths to actual pulse widths. This converts the observed pulse width to between 97 – 110 femtoseconds.

Dispersion of the Ti:Sapphire laser beam was also a setup consideration, especially when using femtosecond pulses. Lenses had to be chosen that were both thin and had material that provided the minimum amount of dispersion. Mirrors had to have a reflective coating which had the maximum amount of reflectivity and the minimum amount of dispersion.

### 2.3.2 THz Beam Optics

A set of THz beam optics was used to collimate the output from the emitter, focus the THz on to the sample, and then focus the THz on to the detector. A key ingredient to a high performance THz TDS system is an optical system that allows one to focus the THz waves to a diffraction-limited focal point at the object while allowing the highest possible transmission. At THz frequencies, the wavelength is not negligible compared with the size of the optical elements, and diffraction effects can dominate ray

propagation. Additionally, because of the large spectral bandwidth of THz emitters, the optical system needs to be achromatic and exhibit a flat phase response over the frequency range of the pulse.

### 2.3.2.1 Substrate Lens

A hyperhemispherical substrate lens design made of silicon was used to direct the THz radiation to or from the substrate. Silicon has practically no dispersion over the entire THz frequency range and therefore is achromatic. There are two types of hyperhemispherical designs that are typically used for the substrate lenses: collimating and aplanatic. In a collimating lens, the rays emitted near the optic axis emerge as a collimated beam, while the rays emitted at larger angles emerge at substantial angles or are internally reflected and lost. The aplanatic hyperhemispherical lens design, which ensures that the critical angle for emerging rays is at 90 degrees, causes rays to diverge as a Gaussian beam with a half-angle of  $\sin^{-1}(1/n)$  ( $\sim 15^\circ$  for silicon). It has three advantages over the collimated lens. It exhibits no astigmatism, it suffers from no losses due to internal reflection, and it allows for a larger effective aperture for the lens and no additional diffraction of the emerging beam [48].

For this research project, only the collimating lens was available, since it was manufactured as one assembly with the Ekspla photoconductive antennas, although the output beam wasn't really collimated in that it initially converged to a minimum spot and then diverged. Either one of the two substrate lens designs can be employed effectively, and can be useful depending on the type of application. The collimating lens can be more

useful in imaging applications, since the focal spot of a THz TDS system can be frequency-independent when re-imaged through a second lens or parabolic mirror.

### 2.3.2.2 Off-Axis Parabolic Mirrors

A series of off-axis parabolic mirrors can be used to collimate and/or focus the THz beam once it departs the silicon lens. For this research, gold coated were chosen initially to maximize reflectivity, but aluminum also worked effectively later in the research. THz beams can be considered Gaussian in nature and can therefore be numerically modeled as Gaussian beams. The effective diameter of a focused Gaussian beam can be defined in terms of the diameter which contains 86% of the focused energy and at the edges of which the focused intensity is already down to  $1/e^2$  of its peak value. Based on this criteria, the effective diameter of the focused Gaussian spot,  $d$ , is given by

$$d \approx \frac{2f\lambda}{d_0} \quad (11)$$

where  $\lambda$  is the wavelength,  $f$  is the focal length of the focusing element, and  $d_0$  is the diameter of the collimated beam [72]. This diameter is an approximation of the diffraction limit of the THz imaging system. Corrections must be applied if the THz beam incident on the focusing mirror is not collimated.

### 2.3.2.3 Gaussian Beams

Terahertz radiation can be modeled as a Gaussian beam, with a representation of that beam shown in Figure 6. The equation for the electric field  $E(\omega, r, z)$  of a Gaussian beam in the TEM<sub>00</sub> mode can be expressed as

$$E(\omega, r, z) = E_0(\omega) \frac{w_0}{w(\omega, z)} \exp\left[\frac{-r^2}{w^2(\omega, z)}\right] \exp\left\{-j\left[\frac{z\omega}{c} - \tan^{-1}\left(\frac{z}{z_0(\omega)}\right)\right]\right\} \exp\left[-j\frac{r^2\omega}{2cR(\omega, z)}\right]. \quad (12)$$

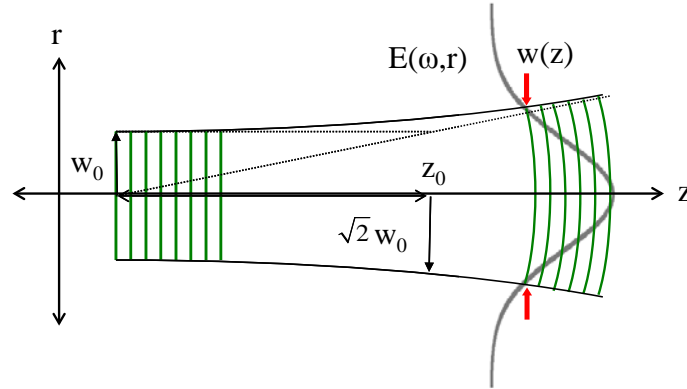


**Figure 6. Diagram showing the components of a Gaussian beam [14].**

In this equation,  $w(\omega, z)$  is the spot size of the beam ( $e^{-1}$  point of the electric field),  $w_0$  is the beam waist,  $R(\omega, z)$  is the curvature of the phase front, and  $z_0$  is the Rayleigh range. The spot size, radius of curvature, and Rayleigh range are defined as

$$w(\omega, z) = w_0 \sqrt{1 + \left(\frac{z}{z_0(\omega)}\right)^2} \quad (13)$$

$$R(\omega, z) = z(\omega) \left[1 + \left(\frac{z_0(\omega)}{z(\omega)}\right)^2\right] \quad (14)$$

$$z_0 = \frac{\pi w_0^2}{\lambda} \quad (15)$$

A THz beam is quasi-optical and is strongly impacted by diffraction, since the Rayleigh range at 0.3 THz is only 3 cm and at 1.0 THz it is 10 cm. Characterizing THz radiation as a Gaussian beam is important because it allows one to numerically propagate the beam

through a system of lenses given an initial spot size and radius of curvature at the exit of the emitter's hemispherical lens.

### 2.3.2.4 Gaussian Beam Expansion

A Gaussian beam can be represented in terms of the curvature of its phase front  $R$  and the spot size of the beam  $w$  by the complex beam parameter  $q$ . The equation for this relationship is

$$\frac{1}{q(\omega, z)} = \frac{1}{R(\omega, z)} - j \frac{2c/\omega}{w^2(\omega, z)}. \quad (16)$$

The complex beam parameter can then be used to propagate the Gaussian beam through an optical system by the use of the ABCD matrix formalism. The output complex beam parameter  $q_{out}$  can be represented in terms of the input  $q_{in}$ :

$$\frac{1}{q_{out}} = \frac{C + D \left( \frac{1}{q_{in}} \right)}{A + B \left( \frac{1}{q_{in}} \right)}. \quad (17)$$

The ABCD matrix has the following format for propagation:

$$\begin{pmatrix} A & B \\ C & D \end{pmatrix} = \begin{pmatrix} 1 & d \\ 0 & 1 \end{pmatrix} \quad \left| \begin{array}{c} \longleftrightarrow \\ \mathbf{d} \end{array} \right| \text{ free space} \quad (18)$$

$$\begin{pmatrix} A & B \\ C & D \end{pmatrix} = \begin{pmatrix} 1 & 0 \\ -1/f & 1 \end{pmatrix} \quad \left( \text{Oval} \right) \text{ lens or mirror} \quad (19)$$

The ABCD matrix formalism allows one to represent an entire optical system by multiplying a series of propagation matrices together.

### 2.3.3 Scanning Optical Delay Line

The THz TDS system requires a means of varying the delay of one optical beam relative to a second beam in order to move the sampling gate across the waveform to be sampled. This is accomplished by varying the optical path length traversed by the two beams by using a scanning optical delay line on one of them. The optical delay is achieved by mounting a retro-reflective mirror on a mechanical scanner. For this application, a Newmark NLS4 mechanical stage, remotely controlled by a computer, was used to scan an 8 cm diameter retro-reflective mirror. The delay line has a maximum speed of 2 inches/second, a resolution of 0.125  $\mu\text{m}$ , and a repeatability of 5  $\mu\text{m}$ .

In many imaging applications it is desirable to scan the optical delay as rapidly as possible in order to increase the waveform acquisition rate. However, there are not many mechanical devices that can scan faster than a few tens of Hertz. Typical point-by-point images formed by imaging systems have a data acquisition rate of 20 pixels per second, which translates to a few minutes per image, if one uses a raster scanner to move the sample through the THz beam [48].

### 2.3.4 Raster Scanner

A Newmark NLS4-x-25 horizontal and an NLS4-x-16 vertical stage were connected to form an X-Y stage used to perform a raster scan on various samples for imaging. The X-Y stage was computer-controlled and could be synchronized with the scanning optical delay line through the Galil motion control software. The vertical component had a maximum speed of 0.5 inches/second, a resolution of 0.06  $\mu\text{m}$ , and a

repeatability of 5  $\mu\text{m}$ , while the horizontal component had the same specifications as the scanning optical delay line.

### 2.3.5 Lock-in Amplifier

A Stanford Research Systems Model SR850 DSP lock-in amplifier was used to collect electronic data off of the THz detector. The time domain data of the THz pulse could be measured with either current or voltage. The lock-in amplifier time constant and optical delay line speed had to be carefully chosen so that the TDS system could accurately collect the entire pulse, maximize the signal-to-noise ratio, and minimize the total scan time. The sensitivity and dynamic reserve had to be chosen to maximize the dynamic range of the lock-in amplifier. Furthermore, the data collection rate and the optical delay line had to be synchronized to control the bandwidth and frequency resolution of the THz TDS system. The bandwidth,  $B$ , is determined by

$$B = (2\Delta t)^{-1} \quad (20)$$

in which  $\Delta t$  is the time step between data points collected in the THz pulse. The frequency resolution  $\Delta f$  is given by

$$\Delta f = (2\Delta t N)^{-1} = (2T)^{-1} \quad (21)$$

where  $N$  is the total number of points and  $T$  is the total time of the scanned pulse.

Finally, “auto-phase” was chosen when collecting the pulse data to adjust the reference phase shift to eliminate any residual phase error and eliminate the imaginary component.

This maximized the amplitude of the peak of the THz pulse. Data collection could be



accomplished by either manual entry of the data through the interface on the front panel of the lock-in amplifier or through a computer interface using LabView.

## 2.4 THz TDS Data Analysis on Composites

After the data has been collected from the lock-in amplifier, various mathematical software tools to analyze that data. Figure 7a shows the time domain response of a typical THz TDS system transmitting through ambient air as the optical delay line is scanned. The time domain data can then be transformed into the frequency domain via a numerical fast Fourier Transform (FFT). A FFT uses an algorithm to solve a discrete Fourier Transform (DFT) more quickly. A DFT is given by

$$E(\omega) = \sum_{t=0}^{N-1} E(t) e^{-\frac{2\pi i}{N} \omega t} \quad k = 0, 1, \dots, N-1 \quad (22)$$

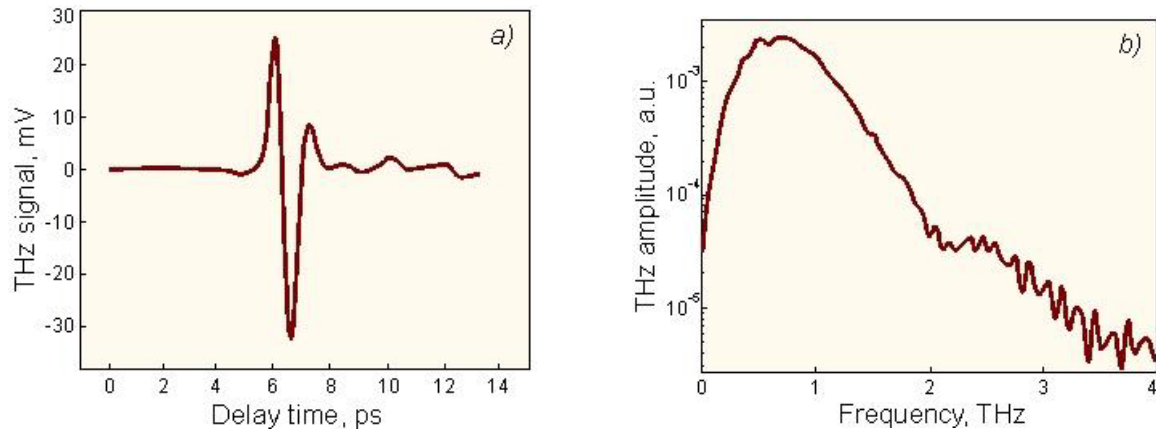


**Figure 7. (a) THz pulse time waveform. (b) THz frequency spectrum [26].**

where  $E(\omega)$  is the frequency response of the received THz signal,  $E(t)$  is the time domain response of the received THz signal, and  $N$  is the total number of samples. A discrete FFT is equivalent to a plane wave expansion that returns the complex amplitude

of the discrete frequency components  $\omega_n$  of the THz pulse. This representation of the THz electric field  $E(\omega_n)$  can be written as

$$E(\omega_n) = E_0(\omega_n) e^{-i(k(\omega_n)x + \omega_n t)} \quad (23)$$

where  $E_0$  is the amplitude and  $k$  is the wave number. Figure 7b represents the magnitude of the Fourier transform of the THz pulse signal in 7a.

In THz TDS, one measures a sample  $E_{\text{sample}}(t)$  and a reference pulse  $E_{\text{ref}}(t)$  in the time domain and then converts them both into the frequency domain,  $\tilde{E}_{\text{sample}}(\omega)$  and  $\tilde{E}_{\text{ref}}(\omega)$ , with an FFT. The pulse that is measured at the receiver is a convolution of the transfer functions of the emitter  $R(t)$  and the receiver  $S(t)$ . The sample also imparts a transfer function  $H(t)$  to the measured THz pulse when it is included in the THz path. A diagram showing the effect of the sample on the transfer functions in the time and frequency domains is shown in Figure 8. The convolution of the sample transfer function in the time domain equates to a multiplication in the frequency domain. An example of the resulting waveforms in the time and frequency domain is illustrated in Figure 9.

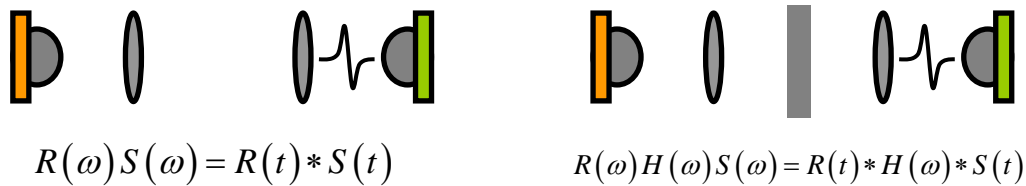


**Figure 8. Components of the THz waveform at the detector in the time and frequency domain [14].**

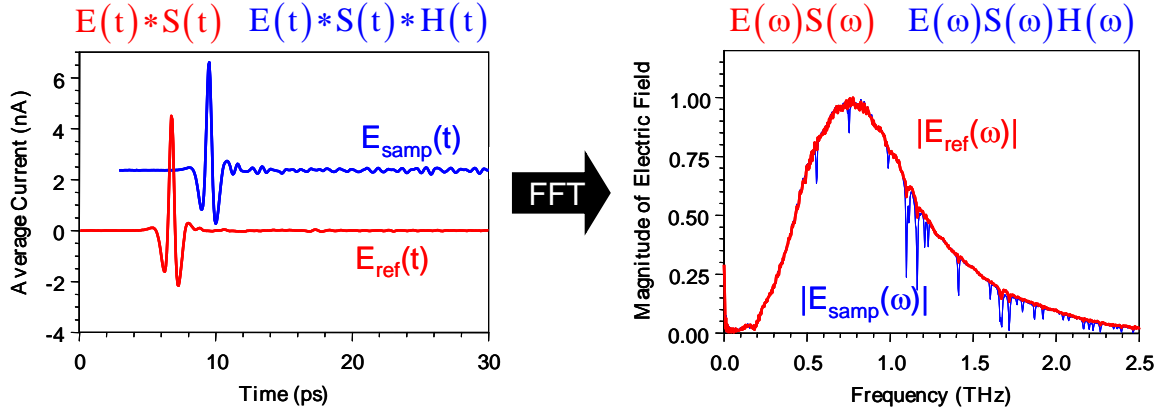


Figure 9. Waveforms resulting from the collection of data at the THz detector [14].

## 2.4.1 Material Parameter Estimation

Material parameters, like the index of refraction and the absorption coefficient, can be measured using a THz waveform. The THz system response of a sample can be determined by dividing the frequency response of system with a sample  $\tilde{E}_{samp}(\omega)$  by the system response of the reference  $\tilde{E}_{ref}(\omega)$ . The system response can be shown with the following equation

$$\frac{E_{samp}(\omega)}{E_{ref}(\omega)} = \frac{R_0(\omega)S(\omega)e^{i(\omega t - k(\omega)x)}}{R_0(\omega)S(\omega)e^{i(\omega t - k_0x)}} = e^{-i(k(\omega) - k_0)x} \quad (24)$$

in which  $R_0$  is the amplitude of the THz emitter transfer function,  $k_0$  is the wave number in free space,  $k(\omega)$  is the wave number for the sample material, and  $x$  is the length propagated. The value for  $k(\omega)$  can be written in terms of its complex parts

$$k(\omega) = \frac{\omega}{c} [n'(\omega) - in''(\omega)] \quad (25)$$

and then added to the version of the sample THz system response given in terms of amplitude  $A$  and phase  $\phi$

$$\frac{E_{sample}(\omega)}{E_{ref}(\omega)} = e^{-\omega/c n''(\omega)x} e^{-i[\omega/c(n'(\omega)-1)]x} = A e^{-i\phi}. \quad (26)$$

## 2.4.2 Drude Model

By measuring the THz system response in either transmission or reflection mode, one can obtain the complex index of refraction of the material. The complex index of refraction  $\tilde{n}(\omega)$  can be written as

$$\tilde{n}(\omega) = n(\omega) - i\kappa(\omega) \quad (27)$$

where  $n(\omega)$  represents the real refractive index and  $\kappa(\omega)$  is the extinction coefficient and is proportional to the absorption coefficient  $\alpha(\omega)$ , which in cgs units is

$$\kappa(\omega) = \frac{\alpha(\omega)c}{2\omega}. \quad (28)$$

One of the ways of predicting the optical properties of a THz TDS system is to use the Drude Model. The Drude Model offers one method of calibrating a THz TDS system so that the accurate performance of the system can be verified.

Usually the optical constants of a semiconductor in the far-infrared region are analyzed with the Drude model. According to the Drude model, the complex conductivity is expressed as

$$\tilde{\sigma}(\omega) = \varepsilon_0 \frac{\omega_p^2}{i\omega + \frac{1}{\tau}} \quad (29)$$

and in this expression  $\tau$  is the momentum relaxation time of free carriers and  $\omega_p$  is the plasma angular frequency defined by  $\omega_p = \sqrt{n_c e^2 / \varepsilon_0 m^*}$ . In this plasma frequency

expression  $n_c$  is the carrier density,  $e$  is the charge of an electron, and  $m^*$  is the effective mass [67]. The complex electrical conductivity can be written in terms of its real and imaginary parts:  $\tilde{\sigma}(\omega) = \sigma_1(\omega) - i\sigma_2(\omega)$  and

$$\sigma_1(\omega) = \varepsilon_0 \omega \varepsilon_2(\omega), \quad (30)$$

$$\sigma_2(\omega) = -\varepsilon_0 \omega [\varepsilon_1(\omega) - \varepsilon_\infty] \quad (31)$$

with  $\varepsilon_\infty$  being the relative dielectric constant of the undoped semiconductor and  $\varepsilon_0$  being the permittivity of free space [67]. In a nonmagnetic medium, the complex dielectric constant  $\tilde{\varepsilon}(\omega)$  is given as

$$\tilde{\varepsilon}(\omega) = \tilde{n}^2(\omega) = \varepsilon - i \frac{\tilde{\sigma}(\omega)}{\omega \varepsilon_0} \quad (32)$$

and  $\tilde{\sigma}(\omega)$  is the complex conductivity.

### 2.4.3 Scattering

Scattering is the process by which electromagnetic radiation is forced to deviate from a straight trajectory by one or more localized non-uniformities in the medium through which it passes. There are two types of elastic scattering: Rayleigh scattering and Mie scattering. Rayleigh scattering is the process by which radiation is scattered by a small element, treated as a small sphere, in which the diameter  $d$  of the sphere is much smaller than the wavelength  $\lambda$  of the radiation. The upper limit for scattering of this type is  $d/\lambda \sim 1/10$ . For elements with diameters comparable to the wavelength, Mie scattering describes the scattering process, and the shape of the scattering elements becomes more relevant. The study of the propagation and scattering of THz pulses through media has

been studied recently [13, 27, 55, 56, 57, 58, 60, 71]. For nondestructive evaluation of composites with THz radiation, one would be interested in isolating air bubbles, voids, and delaminations in the material. One could look at the scattering properties of thin samples and study the multiple-scattering, diffusive, phenomena that can be measured with coherent pulses. Additionally, the scattering effects of the glass fibers and bundles within the composite could be studied.

The scattering of coherent THz radiation  $E_{coh}(\omega)$  can be described using the scattering mean free path  $l_s(\omega)$  as a function of frequency is given by the equation:

$$\frac{|E_{coh}(\omega)|}{|E_{in}(\omega)|} = \exp\left[\frac{-z}{2l_s(\omega)}\right] \exp\left[\frac{-\alpha(\omega)z}{2}\right] \frac{4n}{(n+1)^2} \quad (33)$$

where  $\alpha$  is the absorption coefficient and  $z$  is the thickness of the sample. The scattering mean free path is the inverse of the scattering coefficient  $\mu_s$ . In order to make predictions about scattering of THz radiation from particles one would attempt to determine the scattering cross section  $\sigma_s(\omega)$  of the scattering centers:

$$l_s(\omega) = [n_0 \sigma_s(\omega)]^{-1} \quad (34)$$

in which  $n_0$  is the number density of the scatterers in the material.

If the scattering centers are much smaller than the THz wavelength then the Rayleigh approximation can be used. The scattering cross section for Rayleigh scattering is independent of the particle shape and is given by

$$\sigma_s = \frac{2\pi^5 d^6}{3\lambda^4} \left(\frac{n^2 - 1}{n^2 + 2}\right)^2 \quad (35)$$

where  $n$  is the index of refraction of the scattering centers and  $d$  is the diameter of the spheres. The intensity scattered per unit volume for an unpolarized electromagnetic wave is given by the following:

$$I_s = I_0 \frac{\pi^4 d^6}{8r^2 \lambda^4} \left( \frac{n^2 - 1}{n^2 + 2} \right)^2 (1 + \cos^2(\theta)) \quad (36)$$

where  $\theta$  is the angle measured from the direction of propagation and  $r$  is the distance to the particle. The scattering efficiency  $Q_{eff}$  is commonly used in place of the cross section and is related by

$$Q_{eff} = \sigma_s / A \quad (37)$$

in which  $A$  is cross sectional area of the scattering center. The equation for spheres is more complicated when the size of the scatterers are closer in size to the wavelength of the radiation [42].

In composites, there are strands of fiber woven together and then held together using a resin. The fibers most closely resemble an infinitely long circular cylinder. When the diameter of the cylinder is sufficiently small compared to the wavelength, certain approximations can be used for the scattering coefficients. The scattering cross section per unit length for the TE and TM modes are

$$\sigma_{TM} = \frac{2\pi^5 a^4}{\lambda^3} (m^2 - 1)^2 \quad (38)$$

$$\sigma_{TE} = \frac{4\pi^5 a^4}{\lambda^3} \left( \frac{m^2 - 1}{m^2 + 1} \right)^2 \quad (39)$$

where  $a$  is the radius of the cylinder and  $m$  is the ratio of the index of refraction of the scattering center to the index of refraction of the containing medium. The samples tested

in this research had an overlapping weave pattern of glass strands with all of the strands oriented in one of two directions at 90° angles to each other. The assumption was made that the overlapping pattern would result in an average of the scattering cross section of the TE and TM components,  $\bar{\sigma} = (\sigma_{TM} + \sigma_{TE})/2$ . The intensity of the TE and TM modes at normal incidence are given by

$$I_{TM} = I_0 \frac{2\pi^4 a^4}{\lambda^3 r} (m^2 - 1)^2 \quad (40)$$

$$I_{TE} = I_0 \frac{4\pi^4 a^4}{\lambda^3 r} \left( \frac{m^2 - 1}{m^2 + 1} \right)^2 \cos^2(\theta) \quad (41)$$

when the imaginary portion of the refractive index is small compared to the real part. This illustrates that the intensity of the scattered radiation from infinitely long circular cylinders varies as the fourth power of the cylindrical radius and inversely as the cube of the wavelength. This limiting case for infinite cylinders is compared to the intensity of Rayleigh scattering from small spheres, which varies as the sixth power of the radius and inversely as the fourth power of the wavelength [42].

The radiation from a photoconductive switch is linearly polarized according to the orientation of the emitter dipole. For this research, the emitter was oriented for vertical polarization. If the orientation of the glass fibers is known, then one could predict the intensity of THz radiation scattering from the glass fiber composite. The TM mode has its electric field parallel to the axis of the cylinder while the TE mode has its axis perpendicular to the axis of the cylinder. Using this orientation where the axis of the cylinder is vertical, one can determine the intensity of THz radiation that is scattered



given an incident linear polarization angle. The intensity for the vertically and horizontally polarized components can be defined as

$$I_v = I_0 \frac{2\pi^4 a^4}{\lambda^3 r} (m^2 - 1)^2 \sin^2(\chi) \quad (42)$$

$$I_H = I_0 \frac{4\pi^4 a^4}{\lambda^3 r} \left( \frac{m^2 - 1}{m^2 + 1} \right)^2 \cos^2(\theta) \cos^2(\chi) \quad (43)$$

in which  $\chi$  is defined as the angle from the positive horizontal axis and  $r$  is the radial distance from the  $x$ -axis. A diagram of the configuration is shown in Figure 10 with the scattered radiation propagating as a cylindrical wave [42]. The glass weave strands could be oriented at any angle to the THz polarization direction, at normal incidence.

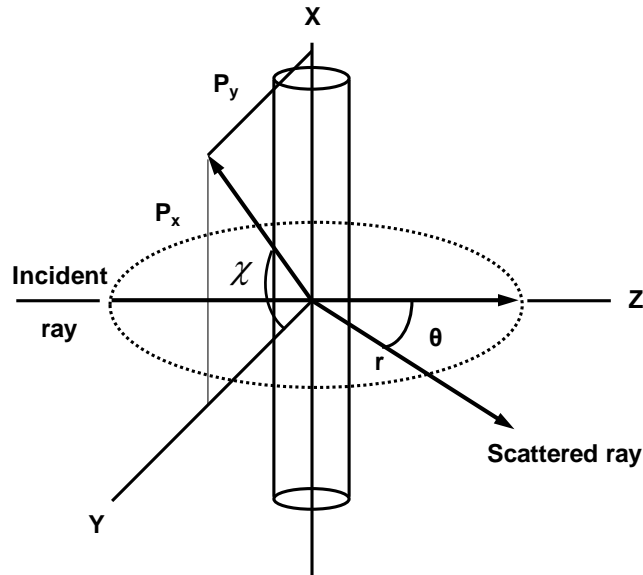


**Figure 10. Diagram showing incident and scattered ray upon an infinitely long cylinder.**

An alternate approach has been presented which models scattering effects within a densely distributed array of infinite cylinders. Its model utilizes an effective field and a quasi-crystalline approximation for the multiple scattering interactions within the dense medium [45].

## 2.4.4 Effective Medium Approximations

The propagation of electromagnetic waves in heterogeneous media can be analyzed using various effective medium approaches [1, 13, 27, 29, 49, 74]. Among these approaches, there are variations of three that have been used most frequently, including the Maxwell-Garnett theory, the Bruggeman effective medium model, and the simple effective medium approximation. All of these theories assume that spherical inclusions have been dispersed into a host matrix, the inclusions are much smaller than the wavelength in the host material ( $< 0.1\lambda - 0.2\lambda$ ), and that the material can therefore be treated like an effective medium as shown in Figure 11 [6]. The model can also be extended to cover cylindrical inclusions by using dielectric tensors.

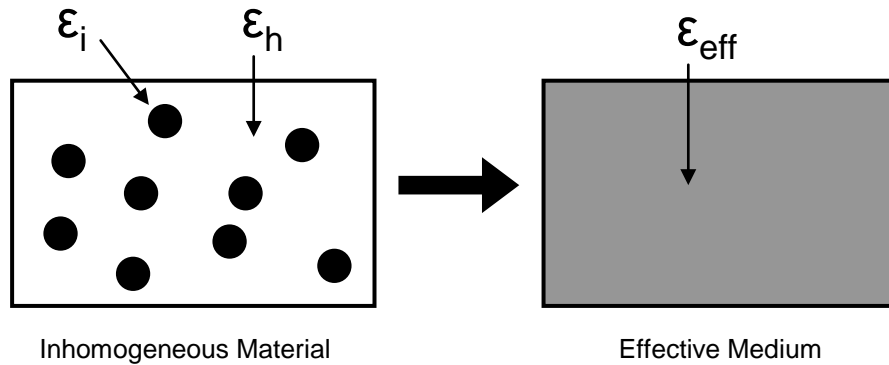


**Figure 11. An inhomogeneous system is replaced by a (virtual) effective medium.**

The simplest effective medium approach is with linear interpolation, using the filling factor  $f$ , which defines the volume fraction of the particles:

$$\epsilon_{eff}(\omega) = f\epsilon_i(\omega) + (1-f)\epsilon_h(\omega) \quad (44)$$

in which  $\epsilon_i$  is the dielectric constant of the inclusions and  $\epsilon_h$  is the dielectric constant of the host material. Another model that is used is called the Maxwell-Garnett effective

medium theory:

$$\varepsilon_{eff}(\omega) = \varepsilon_h(\omega) \left\{ \frac{1 + 2f \left[ \frac{(\varepsilon_i - \varepsilon_h)}{(\varepsilon_i + 2\varepsilon_h)} \right]}{1 - f \left[ \frac{(\varepsilon_i - \varepsilon_h)}{(\varepsilon_i + 2\varepsilon_h)} \right]} \right\}. \quad (45)$$

This theory assumes that the total polarization should be the same as the sum of polarization contributions from the embedded particles. The Maxwell-Garnett approximation holds up well at low filling factors  $f$  until the filling factor reaches a level of approximately 0.15. At this point, the theory developed by Bruggeman must be used to achieve an accurate determination of the effective dielectric constant. The formula is given by

$$f \left( \frac{\varepsilon_i - \varepsilon_{eff}}{\varepsilon_i + K\varepsilon_{eff}} \right) + (1-f) \left( \frac{\varepsilon_h - \varepsilon_{eff}}{\varepsilon_h + K\varepsilon_{eff}} \right) = 0 \quad (46)$$

where  $K$  is a geometric factor. The value for  $K$  is 1 if the inclusions are an array of cylinders with their axes collinear with the incident radiation and the value for  $K$  is 2 if they are spherical nanoparticles [8].

## 2.4.5 Imaging

The THz wave distribution function and the target's refractive index can be described by Maxwell's Equation:

$$\nabla^2 \bar{E}(\omega, r, t) + \frac{\tilde{n}(\omega, r)^2}{c^2} \frac{\partial^2}{\partial t^2} \bar{E}(\omega, r, t) = 0 \quad (47)$$

where  $r$  denotes a point in space,  $c$  is the speed of light, and  $\tilde{n}$  is the complex refractive index of the medium. In the case where the polarization effects of the wave can be neglected in the temporal frequency domain, this equation can be written as the scalar

Helmholtz equation

$$\nabla^2 \bar{E}(\omega, r) + k_0^2 \tilde{n}(\omega, r)^2 \bar{E}(\omega, r) = 0 \quad (48)$$

in which  $E(\omega, r)$  is the complex amplitude function of the electromagnetic field and  $k_0$  represents the wave number. This Helmholtz equation is valid in imaging and tomography applications. The purpose of THz imaging is to determine the refractive index function  $\tilde{n}(\omega, r)$  using the measured THz wave amplitude and phase distribution function  $E(\omega, r)$  [75].

THz imaging can be performed in either transmission or reflection mode. A THz TDS imaging system is constructed with a focus at the desired location of the object to be imaged. The waveform of the THz pulse that goes through the object at that focus can then be measured. By translating the object and measuring the transmitted waveform for each position of the object, an image can be built pixel by pixel. The two dimensional image that is formed may be represented by such aspects of the waveform as amplitude, phase, or a combination of the two. Phase, or time delay, imaging consists of the extraction of the arrival time of the waveform at each pixel. For amplitude imaging, one could use the peak-to-peak amplitude of the time-domain waveform for a measure of bandwidth-averaged transmission. Alternatively, one could perform an FFT of each pixel's waveform and then integrate over any desired frequency band to display some part of the spectral information [12, 48].

Three-dimensional, THz tomography refers to the cross-sectional imaging of an object by measuring either the transmitted or reflected illumination. One way of accomplishing this is to measure the time-domain THz pulse transmitted through or

reflected by the material. The resulting waveform will consist of a series of reflections from the sample of the various dielectric interfaces within that sample. The polarity and magnitude of each reflection are given by the reflection coefficient at each interface and are related to the size and sign of the corresponding index step [48]. This form of THz tomography is restricted, though, in its applicability. This type of tomography is based on three assumptions: (1) the samples have no dispersion, absorption, or diffraction affects, (2) the reflections are so weak that multi-reflections can be neglected, and (3) the refractive index is uniform throughout each layer [75]. Any one of the affects listed can significantly alter the shape of the reflected waveform. A numerical Fourier deconvolution in the time-domain could be applied to the waveform to more accurately measure the position of each of the reflections. Other methods of tomography are diffraction tomography, computed tomography, binary lens tomography, optical coherence tomography, and digital holography [75].

#### **2.4.6 Image Processing**

The image of a composite sample can be formed by arranging the pixels that were collected during the THz TDS scan. Since THz images are formed from a limited number of samples, their images appear “pixelated.” Interpolation techniques can be employed which enable one to remove the sharp edges of the pixels to make the image easier to view visually. Interpolation is the estimate of a signal at locations other than where it was sampled. If a two dimensional array’s pixels are expanded equivalently in both dimensions, the interpolation is called zoom or electronic zoom. Various

interpolation techniques in the time domain include the ideal sinc, zero order, triangular, or cubic spline interpolator [32].

A frequency domain interpolation technique was applied for the THz images in this research. The sampling rate was increased by zero-padding in the spatial frequency domain. First, the two-dimensional image can be transformed to the frequency domain with a discrete cosine transform (DCT). A DCT is similar to the discrete Fourier Transform (DFT) except that it uses only the real numbers, and is frequently used in data compression algorithms because it tends to concentrate information. Then the resulting matrix can be zero-padded in the spatial frequency domain which increases the sampling rate in the spatial domain. Finally, an inverse DCT can be performed on the data which results in the display of much smaller pixels and an apparent smoothing of the original pixel edges. By using the interpolation technique outlined above, zero-padding out to ten times the length and width in the frequency domain, the new image will appear to look the same as if the original image was shrunk ten times.

MATLAB also has a function called 'interp' which is designed to smooth boundaries between pixels. However, when this function is used on its own, it tends to create a blurry image if the pixels are too large. Occasionally, the DCT can leave a periodic pattern in the image from sharp boundaries which can be further smoothed out with a filter. A filter that has been used successfully for THz imaging by Zhang et al. is the Wiener filter [75].

## 2.5 THz TDS Literature Review

This section summarizes some of the recent work that has been published on the NDE of materials using THz TDS and on the progress in modeling the THz electrical and optical properties of those materials. This is followed by a summary of some of the work done on imaging and on characterizing the THz properties of composites, ceramics, and semiconductors, as well as paint and foam adhering to metallic surfaces.

### 2.5.1 Composites

A composite is defined in the American Heritage Dictionary as: “A complex material, such as wood or fiberglass, in which two or more distinct, complementary substances, especially metals, ceramics, glasses, and polymers, combine to produce structural or functional properties not present in any individual component” [3].

Composite designers can choose from a variety of fiber reinforcements and resins to develop the laminate structure. The reinforcement material provides mechanical properties such as stiffness, tension and impact strength, while the resin system (matrix) provides physical properties including resistance to fire, weather, ultraviolet light and corrosive chemicals. Three factors must be considered when choosing reinforcements. One must first choose the type of fiber: usually fiberglass, aramid (in Kevlar), or carbon fiber (also called graphite). Then one must choose the form: either roving strands, mat, or fabrics. Finally, an orientation of fiber direction is chosen, including parallel, circumferential, or helical along the length of the part, and/or with random continuous strands. The three types of resins that are available are polyester, vinyl ester, and epoxy.

A form, either wet lay-up or prepreg (a reinforcement saturated with resin), must be carefully chosen to ensure a successful design [78].

Several articles have been written describing the response of THz radiation when transmitted through various composites. One of the types of composites that has been studied involves polymers, which can be mixed with other additives or fillers to yield compounds with modified physical properties. In the manufacture of these composites, it can be difficult to verify the degree of homogeneity of the resulting compound, especially when using nanoscale fillers. One research group studied samples of low-density polyethylene (LDPE) containing titanium dioxide nanospheres (diameter  $\sim 270$  nm) coated with silver nanoparticles ( $\sim 20$  nm) as well as glass-fiber reinforced with epoxy [64, 66]. For the first case, they were able to see inhomogeneous areas in the LDPE polymer, but were not able to unambiguously determine whether the inhomogeneities were a result of the internal content or the surface reflections from the rough surface. In the case of the glass fiber matrix, THz TDS was able to locate materials and defects hidden inside the sample. A separate article characterizes the refractive index and absorption coefficient of polymers, including high-density polyethylene, Picarin, and cyclic olefin polymer [69]. All of these polymers can be used to fabricate THz communication systems. The authors showed that up to 90% of the incident THz radiation passes through 2 mm of each of the materials with very little attenuation, making them good candidates.

Another composite that has been studied is the polymer-graphite composite [70]. These types of composites are excellent absorbers of THz radiation with good shielding efficiency and small reflection. THz TDS was used to measure the complex refractive



index of this composite, showing that with a 35.7% graphite concentration, reflection was less than 10%, while the absorption was over 80%. Finally, a separate study has been conducted on aerospace carbon-fiber composites and space shuttle insulating tiles, exploring the effectiveness of using THz radiation for NDE of heat damage and voids [62]. The article was focused primarily on comparing continuous wave (CW) THz techniques to pulsed techniques, showing that CW THz systems have sufficient resolution to detect voids and heat damage.

### **2.5.2 Ceramics**

Although ceramics can be considered a subset of composites, a ceramic is more specifically defined in Wikipedia as “an inorganic non-metallic material whose formation is due to the act of heat” [78]. Ceramics are used in a wide range of applications including jet engines and mirrors. Silicon carbide (SiC) is a ceramic material which is strong and light-weight and is an excellent choice to be used for space-based mirrors. It is a difficult material to mount, and the unrelieved stress that results from mounting can cause failure during launch. The photoelastic effect, measured in the THz spectrum, can be used to measure the stress induced in the SiC. Recent literature has shown that the photoelastic effect has been used effectively to characterize defects in silicon carbide wafers in the optical regime [43, 46].

Studies have recently been conducted using THz TDS on aluminum oxide bearings and glass ceramics to measure their optical constants and to probe them for existing fractures [62, 63, 68]. Measurements have also been made on the dielectric constants and loss tangents of low-loss, high dielectric constant ceramics at THz

frequencies [11]. The materials tested included alumina, steatite, titania loaded polystyrene, and zirconium-tin-titanate. The real part of the dielectric constants of these materials were 6.5, 9.3, 16, and 37-93 respectively for each of them and could be used for cost effective photonic crystal components. Finally, material parameters were measured on various building materials, like plaster, glass, and wood [59].

### 2.5.3 Paint Thickness over Metallic Surfaces

The external coating of nearly all military aircraft is stripped down to bare metal during programmed depot maintenance cycles. This paint stripping process has become cost prohibitive in recent years and continues to be a major problem for the sustainment of aging aircraft fleets. One of the main contributing factors is the requirement to visually inspect aircraft for corrosion and fatigue damage. Several nondestructive techniques have been used to avoid visual inspection, including infrared, eddy current, ultrasonic, radiographic, and near-field microwave. THz offers the advantage of being non-contact, penetrating nonconductive materials, and reflecting from both metallic materials and from impedance discontinuities like voids and inclusions [16].

One paper presented an approach to use THz tomography to measure the thickness and degree of drying in the painting process. The thickness resolution  $d_{\min}$  is the limiting factor when using THz radiation and is given by

$$d_{\min} = (c\Delta T)/(2n_g) \quad (49)$$

where  $c$  is the speed of light in a vacuum,  $\Delta T$  is the temporal width of the THz pulse, and  $n_g$  is the group index of refraction for the medium [87]. This paper reported that the resolution was limited to  $\sim 10 \mu\text{m}$ . Another paper reported that surface roughness

differences below  $\sim 10 \mu\text{m}$  were indistinguishable from the metallic background when searching for corrosion under paint [5].

## 2.5.4 Semiconductors

THz TDS can also be used to measure the optical and electrical properties of a semiconductor by the technique outlined in section 2.4.1. Such techniques have been applied to various semiconductor materials and their nanostructures, including quantum dots [54], photonic crystals, and carbon nanotubes, which can have both metallic and semiconductor properties. Photonic crystals, made from semiconductor materials, have been studied recently using THz TDS to determine both defects and group velocity and group velocity dispersion characteristics [37, 38, 39, 53]. The dielectric constant of carbon nanotubes has been measured with a combination of the Drude and Lorentz harmonic oscillator models [41, 47]. In the dielectric function  $\varepsilon(\omega)$  shown in the following equation, the second term in the sum represents the Drude model and the third term represents the Lorentz model:

$$\varepsilon(\omega) = \varepsilon_{\infty} - \frac{\omega_p^2}{\omega^2 + i\Gamma\omega} + \frac{\omega_{p,L}^2}{(\omega_L^2 - \omega^2) - i\Gamma_L\omega}. \quad (50)$$

The term  $\varepsilon_{\infty}$  is the dielectric constant at infinity,  $\omega_p$  is the plasma frequency,  $\Gamma$  is the damping rate in the Drude model,  $\omega_L$  is the phonon frequency,  $\Gamma_L$  is the spectral width, and  $\omega_{p,L}$  is the strength of the Lorentz oscillator. Further characterization using the Drude model could also allow one to determine the number of photocarriers which have been generated.

Carrier dynamics can also be determined by using a technique called Optical-pump THz-probe spectroscopy to measure the conductivity of photocarriers as a function of time after photoexcitation [2, 10]. In this photoluminescence setup, an additional probe beam from the laser source is used to optically illuminate the sample and generate carriers so that it can then be probed with a THz beam. The optical-pump THz-probe technique has been used extensively to study semiconductor carrier dynamics. It has also been used to measure the optical and electronic characteristics of the material by using the free electron Drude model or the Lorenz model to estimate the dielectric constant.

### **2.5.5 Measuring Material Properties with THz Radiation**

Significant efforts have been expended on the development of THz imaging systems; however, somewhat less attention has been paid to the issue of the propagation through, or scattering from, realistic target materials which might be investigated with such systems. Understanding the interaction of THz radiation with a wide range of both homogeneous and inhomogeneous materials is an essential part of the design of systems for THz sensing and imaging. This section attempts to provide a summary of some of the recent work done on modeling the scattering of THz radiation and on the estimation of material parameters using THz TDS.

#### **2.5.5.1 Transmission Mode Measurement Technique**

One method of determining the material parameters of a homogeneous, planar material in using THz TDS in transmission mode is outlined by Dorney et al [23]. A schematic of the interaction of a THz pulse with a sample is shown in Figure 12. An

incident pulse contacts the sample where part of the wave is reflected and part is transmitted. As the THz wave propagates through the material it interacts with that material. Multiple reflections can also occur at the internal interfaces of the material, creating multiple output pulses.

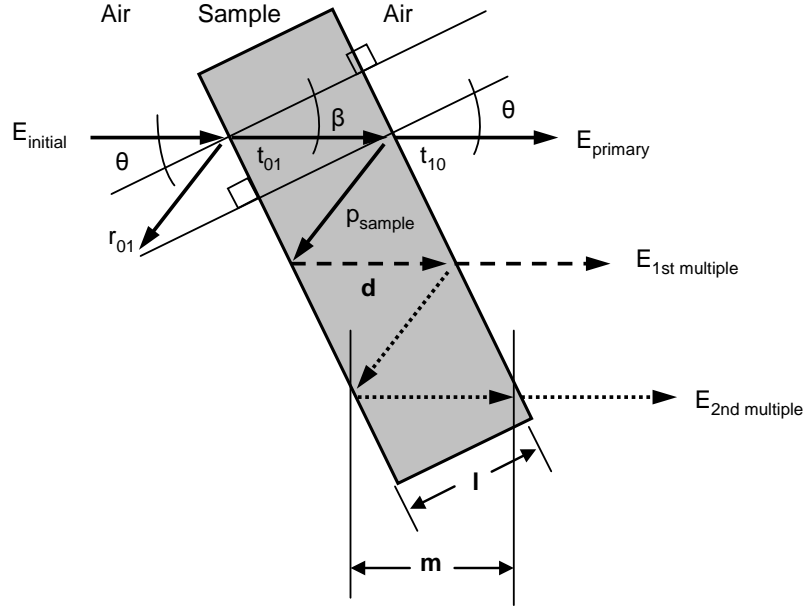


Figure 12. Transmission and reflection of a THz wave through a planar, homogeneous material.

The Fresnel equations describe the transmission and reflection of the THz wave at each interface

$$\tilde{t}_{ab}(\omega) = \frac{2\tilde{n}_a(\omega) \cos \theta}{\tilde{n}_a(\omega) \cos \beta + \tilde{n}_b(\omega) \cos \theta} \quad (51)$$

$$\tilde{r}_{ab}(\omega) = \frac{\tilde{n}_b(\omega) \cos \theta - \tilde{n}_a(\omega) \cos \beta}{\tilde{n}_a(\omega) \cos \beta + \tilde{n}_b(\omega) \cos \theta} \quad (52)$$

where  $\tilde{t}_{ab}(\omega)$  is the transmission coefficient of a wave at an incident angle  $\theta$  from region a to region b and  $\tilde{r}_{ab}(\omega)$  is the reflection in region a at the a-b interface. The angle  $\theta$  is estimated and the angle  $\beta$  is an approximation of Snell's law for nearly transparent materials:

$$\beta = \arcsin\left(\frac{n_a \sin \theta}{n_b}\right). \quad (53)$$

As the wave moves through the material along the path designated  $d$ , it accumulates a phase change through given by  $p_d(\omega, d)$  according to a transfer function or THz system response

$$p_d(\omega, d) = \exp\left(\frac{-i\tilde{n}_b(\omega)\omega d}{c}\right) \quad (54)$$

where  $c$  is the speed of light and the ray length  $d$  is determined by

$$d = \frac{l}{\cos \beta}. \quad (55)$$

Scattering is neglected in this model including such effects as the interface roughness [23].

The THz path both with and without the sample must be considered. For the free-air path, or reference path, we have

$$E_{ref}(\omega) = E_{initial}(\omega) p_{air}(\omega, x) \quad (56)$$

with the distance  $x$  being the distance between the transmitter and receiver and  $n_{air}$  being the index of refraction of air (1.00027). For the propagation through a sample, the distance  $m$  through the sample must be subtracted from the distance traveled through air. This distance varies with the angle of incidence and the material parameters. This distance  $m$  is defined as:

$$m = d \cos(\theta - \beta). \quad (57)$$

In Figure 12 there are only two additional paths shown representing the Fabry-Perot effect, but several additional paths could also be shown. The equation for the primary

received signal through the sample is given by

$$E_{primary}(\omega) = E_{initial}(\omega) P_{air}[\omega, (x-m)] \times t_{01} P_{sample}(\omega, d) t_{10}. \quad (58)$$

In this expression,  $t_{01}$  is the transmission coefficient at the air-sample interface and  $t_{10}$  is the transmission coefficient at the sample-air interface. Now that we have both the reference wave and the sample wave defined, we can define the ratio of the two

$$\frac{\tilde{E}_{primary}(\omega)}{\tilde{E}_{ref}(\omega)} = \frac{4\tilde{n}_{air}(\omega)\tilde{n}_{sample}(\omega)\cos\theta\cos\beta}{[\tilde{n}_{air}(\omega)\cos\beta + \tilde{n}_{sample}(\omega)\cos\theta]^2} \times \left( \exp\left\{ \frac{-i[d\tilde{n}_{sample}(\omega) - m\tilde{n}_{air}(\omega)]\omega}{c} \right\} \right). \quad (59)$$

This provides the transfer function for the model, where only the complex function for  $n_{sample}(\omega)$ ,  $l$ , and  $\theta$  are free variables [23].

This procedure, outlined by Dorney et al., involves a three step iterative process of determining the thickness and the complex index of refraction. The first step is to make an initial guess at the thickness of the sample. Second, the algorithm calculates the beginning functions for the complex index of refraction, assuming a non-dispersive medium. Finally, a gradient descent algorithm iterates the complex index of refraction in frequency until the total error no longer decreases monotonically. The complex index of refraction is then computed in this manner for a range of thicknesses. A metric called total variation is then used to select which pair of refractive index and thickness should be selected [23].

### 2.5.5.2 Literature Summary of THz Material Parameter Measurements

The technique for modeling the material parameters of a homogeneous, planar, optically thin, low-absorption material is shown in section 2.5.5.1. This technique was designed by Duvillaret et al. and refined by Dorney and Mittleman [22 - 25]. Although

Duvillaret et al. claim that an accurate initial guess at the sample thickness is very important to determine the material parameters, Dorney et al. claim that they are able to accurately determine sample thickness and refractive index by initially bounding the upper and lower limits of the thickness  $l$

$$l_{upper} = \frac{\Delta tc}{n_1 - n_{air}}, \quad l_{lower} = \frac{\Delta tc}{n_2 - n_{air}} \quad (60)$$

in which  $\Delta t$  is the time delay between the reference pulse and the first pulse from the sample. The parameters  $n_1$  and  $n_2$  are the limits of the range of refractive index, of which the range 1.2 – 8 covered most practical cases [23]. Withamayachumnankul et al. were able to use a fixed-point iterative method to determine the complex refractive index of the sample within a few iterations, given the sample thickness. Using the same measurement techniques as Dorney and Duvillaret, their iterative process gave the correct parameters for a silicon wafer sample when the material thickness exceeded 200  $\mu\text{m}$  [79, 80].

Xu et al. prepared a simulation with a Lorentz oscillator model to evaluate the accuracy of the extracted optical constants in THz TDS [85]. They analyzed the influence of the angle deflection, the delay-line timing error, and background and 1/f noise on the THz TDS measurement precision. They found that the deflection of the incident angle can influence both the real and imaginary parts of the index of refraction and the spectral features of the errors show a parabolic shape. They also found that the delay-line timing uncertainty introduced an exponential-dependent deviation curve of the imaginary part in the frequency domain and a dramatic feature in the resonant region for the real part.



A separate study reported on the propagation of a single-cycle THz pulse in a random media. Pearce et al. demonstrated a unique method for characterizing the diffusive radiation emerging from a random medium, involving the measurement of both its amplitude and phase [56]. They were able to compute a time-windowed temporal correlation between fields measured at different spatial locations which enabled them to identify individual scattering events for imaging applications. Pupeza et al. have developed a refined approach to measuring optical material parameters [61] while Kuzel et. al. has extracted both the complex refractive index and the wave impedance using THz TDS [44].

### **2.5.6 THz TDS for NDE**

This subsection outlines some of the recent literature reported specifically on the use of THz for NDE and quality control. In composite research, fiber glass samples from the automotive industry have been analyzed for their material property characteristics and have been imaged to show damage from stress [64, 66]. Some of the polymers that are typically used as the matrix material in composites have also been researched [76, 77]. The first article looks at the use of THz imaging to inspect plastic weld joints. They were able to use THz TDS to reveal contaminates like metal or sand within a weld joint of two polyethylene sheets and to identify small air gaps where the welding process had failed. In the second article, the authors were able to determine the additive content of polymers used in composites, including magnesium hydroxide in polyethylene, glass fibers in polyamide, and calcium carbonate, silicon or silicon dioxide in polypropylene.

THz NDE is also being proposed as a method of inspecting the adhesive bond-line of space shuttle tiles for defects [4, 84, 92]. Space shuttle tiles are manufactured from silica into a very porous material. These tiles are then bonded to the bottom of the space shuttle to provide insulation for re-entry. A triangular shaped defect was identified using data from a THz NDE scan and post-processing with a Hilbert-Huang Transform [4]. This process successfully highlighted the boundary between the triangular shaped defect and the background.

There are other articles which have been written to describe the use of THz TDS for NDE of materials other than composites. One of the authors presents work using THz TDS in reflection mode to inspect mural paintings for damage. They are able to image a sub-surface painting of a butterfly hidden beneath various colors of paint [34]. A separate application uses THz TDS to detect foreign bodies in chocolate bars, including metallic objects, stone, glass, and plastics. It can also distinguish these objects from nuts and other food products within the bars [40].

### **3. Material Parameter Estimation with Terahertz TDS**

In the nondestructive testing of aircraft composites, one is ultimately interested in identifying damage, including damage from heat and mechanical stress, and the detection of voids and delaminations. Measuring the material properties of a composite provided insight into the fundamental interaction of THz radiation with the material and could be tested as a technique to see if the material properties of a damaged composite were changed. A major focus of this chapter is to present the results obtained when THz TDS, in transmission and reflection configuration, was used to measure the index of refraction and absorption coefficient of various materials. In addition, scattering and effective medium theory were studied for their applicability to composites. Finally, this material parameter measurement technique was applied to composite samples with burn damage.

#### **3.1 THz TDS System Characterization**

There were several challenges associated with setting up a THz TDS system, including the accurate alignment and measurement of laser pump and probe beams, THz beam alignment, and the maximization of THz output signal quality. A diagram of our first setup for material parameter measurements is shown in Figure 13, using only two parabolic mirrors since the beam did not need to be focused onto the samples. To determine the point at which the TDS system measurements were of sufficient quality, we started with an initial set of criteria for comparison. The next sections will detail these criteria and the methodology for analyzing the THz output, including the measurement of water absorption spectra. This will be followed by a subsection on the

modeling of the THz pulse and associated spectrum. This will be followed by an explanation of some of the difficulties that we had initially with the PCA detector and of the techniques that we used to help align the THz TDS system more quickly.

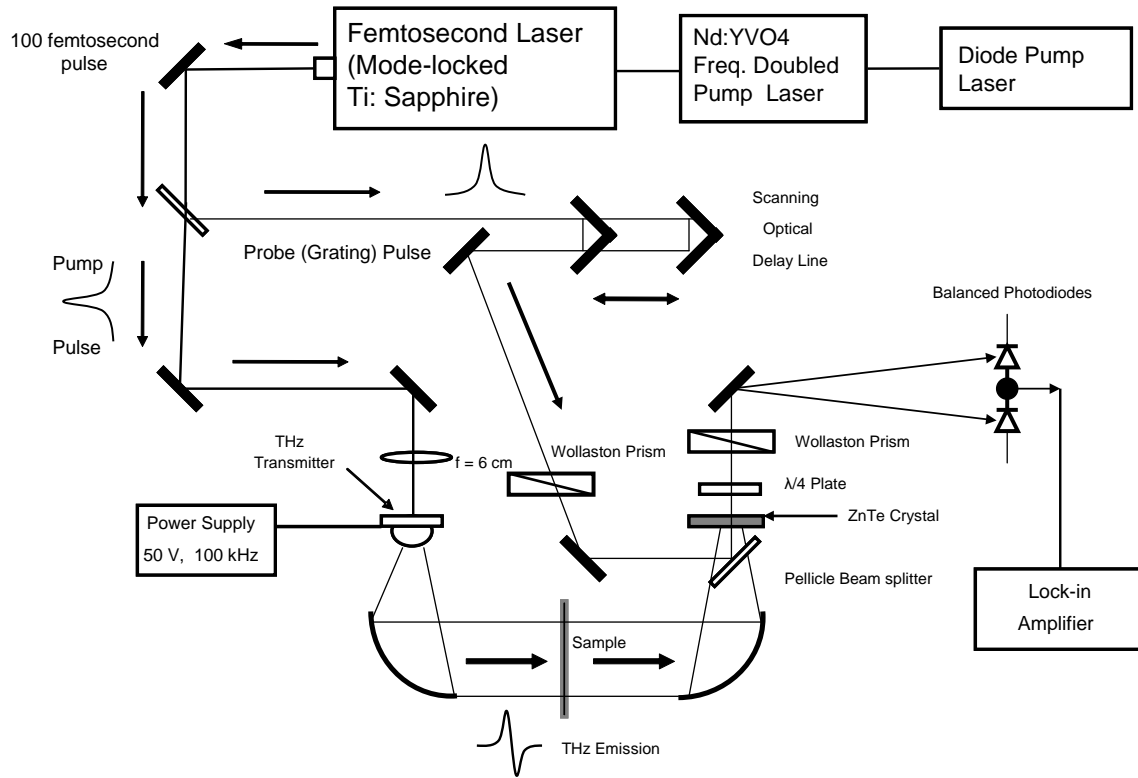


Figure 13. THz TDS setup for material parameter measurements.

### 3.1.1 THz TDS Output Specifications

The output specifications that we used to help evaluate our THz TDS system were detailed by Cheville et. al. in their THz tutorial [14]. These criteria are compared in Table 1 along with the measured results from our THz TDS setup. Although one could measure the signal-to-noise ratio from a logarithmic plot of the THz amplitude spectrum, Cheville et. al. recommend measuring the signal-to-noise ratio and the dynamic range in the time domain. The signal-to-noise level was measured by fixing the optical delay line

at the position of peak pulse amplitude and then collecting data for 30 minutes at that position. One could then measure the mean of the peak amplitude and observe how much the signal drifted. The signal-to-noise ratio is given by

$$\frac{\text{Signal}}{\text{Noise}} = \frac{V_{pk-mean}}{\left(\frac{\Delta V_{pk}}{2}\right)} \quad (61)$$

when the THz signal is measured in volts. The dynamic range is then measured by collecting a scan of the pulse, making sure to take sufficient time domain data in front of the pulse ( $t < 0$ ). The data is then scanned to find the smallest voltage step in this period prior to the pulse and is then compared to the peak of the pulse

$$\text{dynamic range} = \frac{V_{pk}}{\Delta V_{\min(t < 0)}} \quad (62)$$

The measurement accuracy specification was made by comparing 10 separate THz TDS scans and comparing the absolute variations in the amplitude spectra between them.

**Table 1. THz Time Domain Spectrometer specifications and measurements.**

Specification	Typical Value	Conditions	AFIT Typical Measured Value
Amplitude Dynamic Range	20,000:1	Measured in time domain	14,000:1
Power Dynamic Range	400,000,000:1	Amplitude value squared	196,000,000:1
Median Frequency	0.654 THz	Determined by spectral amplitude	0.704 THz
Bandwidth	0.06 to 2.51 THz 0.12 to 1.64 THz 0.26 to 0.92 THz	2% points of peak amplitude 10% points of peak amplitude 50% points of peak amplitude	0.01 to 2.5 THz 0.05 to 1.9 THz 0.15 to 1.35 THz
Signal-to-Noise (Signal Drift)	$\pm 0.5\%$ from mean	Measured sitting at peak of pulse over 30 minute period	$\pm 2.75\%$ from mean standard deviation = 0.9%
Measurement Accuracy	$\pm 0.5\%$ @ 0.2 THz $\pm 0.5\%$ @ 0.5 THz $\pm 0.25\%$ @ 1 THz $\pm 2\%$ @ 2 THz	No signal averaging, 10 minute scan length	$\pm 3.23\%$ @ 0.2 THz $\pm 0.22\%$ @ 0.5 THz $\pm 5.14\%$ @ 1 THz $\pm 20\%$ @ 2 THz

### 3.1.2 Water Vapor Absorption Spectra

Another method that was used to determine if our THz TDS setup was producing accurate results was to look at water vapor absorption spectra. The water vapor in the atmosphere leaves fluctuations after the main pulse in the time domain and it leaves characteristic notches in the frequency spectrum. A full scan of the THz pulse through air was taken by moving the optical delay line at a slow rate. The results of the scan are shown in Figure 14. It should be noted that the smaller pulse in 14a is a result of reflections in the ZnTe crystal which cause the Fabry-Perot etalon effect in 14c. The phase plot in 14b shows how the phase unwraps linearly with frequency.

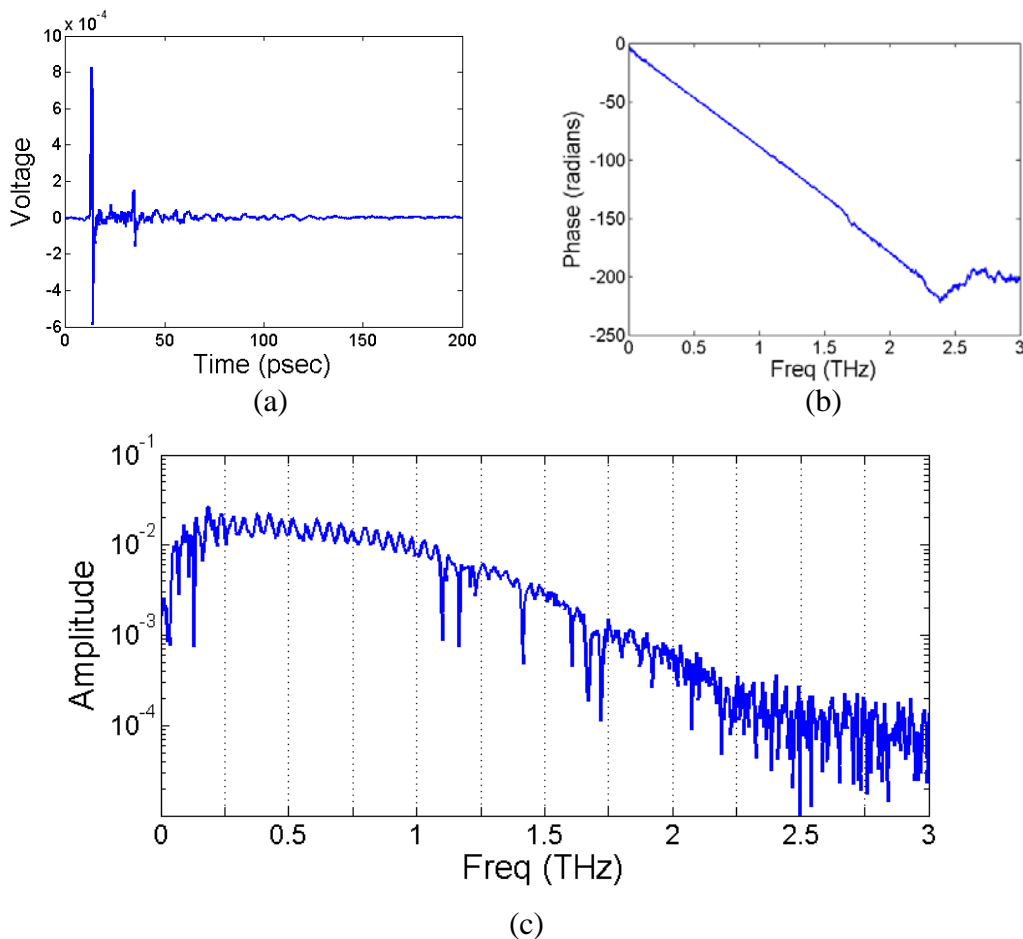


**Figure 14. THz TDS scan of ambient air: (a) THz time domain pulse, (b) THz phase spectrum, and (c) THz amplitude spectrum.**

The absorption lines in 14b can now be identified in the THz frequency spectrum and can be compared with those measured and calculated in the literature. As shown in Table 2, our absorption lines line up fairly closely with published values between 1.0 – 2.4 THz. Several articles have been written measuring the absorption spectrum of water at various relative humidity readings and studying the various molecular transitions and phenomena associated with absorption [83, 90].

**Table 2. Absorption spectrum rotational transitions for water vapor between 0.2 – 2.4 THz [82].**

<b>Transition Number</b>	<b>Published Frequency (THz)</b>	<b>Measured Frequency (THz)</b>	<b><math>\Delta\nu</math> (THz) Published - Measured</b>
1	0.557	0.56	-0.003
2	0.753	0.75	0.003
3	0.989	0.99	-0.001
4	1.098	1.10	-0.002
5	1.164	1.16	0.004
6	1.2264	1.23	-0.0036
7	1.4116	1.41	0.0016
8	1.603	1.60	0.003
9	1.671	1.67	0.001
10	1.718	1.71	0.008
11	1.798	1.80	-0.002
12	1.869	1.87	-0.001
13	1.921	1.92	0.001
14	2.076	2.07	0.006
15	2.264	2.27	-0.006
16	2.346	2.35	-0.004
17	2.393	2.40	-0.007

### 3.1.3 THz Pulse and Spectrum Modeling

The shape of the THz pulse was very sensitive to the position and alignment of the laser pump and probe beams as well as the THz optics. One could attempt to predict the shape of the THz beam in both space and time by approximating it as a Gaussian

pulse. In one article, the authors have already attempted to model the effects of EO sampling on a Gaussian pulse emitted from a GaAs crystal and detected by a ZnTe crystal [9]. Beside the effect of the THz emitter and detector, both the alignment of the lenses and mirrors as well as the sample have an effect on the eventual shape of the pulse. In this exercise, the emphasis was on modeling the effects of a glass fiber composite sample on the THz pulse and comparing modeled data to measured data.

When pulses reach the single cycle regime, like they do with THz TDS, one must use the following equation to model the electric field  $E(r,t)$  of the pulse:

$$E(r,t) = \exp\left(\frac{-\eta(t)^2}{2}\right) \exp\left(\frac{-w_0\omega_1\tau_{G0}r}{2Lv\tau_G}\right) \exp\left(\frac{i\omega_1\tau_{G0}^2\eta(t)}{\tau_G^2}\right) \quad (63)$$

where  $w_0$  is the spot size of the THz beam,  $\omega_1$  is the central frequency of the THz spectrum,  $\tau_{G0}$  is the pulse duration,  $r$  is the distance from the center of the beam,  $L$  is the distance the pulse has traveled, and  $v$  is the speed of the pulse through the medium modified by the complex index of refraction [19]. The terms  $\eta(t)$  and  $\tau_G$  are defined as:

$$\eta(t) = t - \frac{L}{v} - \frac{r^2}{2Lv} \quad \text{and} \quad (64)$$

$$\tau_G = \sqrt{\tau_{G0}^2 + \left(\frac{w_0r}{Lc}\right)^2}. \quad (65)$$

In modeling the THz pulse shape in the time domain, the spot size was assumed to have a width  $w_0$  of 0.6 mm which became mostly irrelevant when considering the center of the THz spot at  $r = 0$ . Both the THz pulsewidth and frequency center of mass had to be measured from actual data. Data was chosen carefully so that the majority of the pulse



had a positive polarity like a Gaussian. The full width at half maximum (FWHM) value of  $\tau_{G0}$  was measured to be 0.62 psec and the THz central frequency was 0.55 THz.

After choosing the THz signal characteristics, the Gaussian pulse through the air reference was modeled in the time domain and frequency domain. The glass fiber complex index of refraction was applied to the frequency domain data using  $2.05 - iK(\omega)$  where  $K(\omega)$  is the imaginary part of the index of refraction. Then an inverse Fourier transform was applied to return the pulse to the time domain. The comparisons of the modeled and measured pulses and frequency spectra can be seen in Figure 15. Although a Gaussian distribution for the pulse was assumed, the FWHM value  $\tau_G = \tau_p / 1.177$  for a Gaussian was not small enough to match the measured frequency response. A factor of  $\tau_G = \tau_p / 1.763$ , similar to a sech distribution, was more accurate in modeling the THz pulse and spectrum characteristics. The magnitude of the modeled air reference pulse was chosen to match the peak-to-peak amplitude of the measured THz pulse. It is apparent that factors other than the sample have an effect on the THz signal, such as the THz emitter, detector, optics, and water vapor absorption.

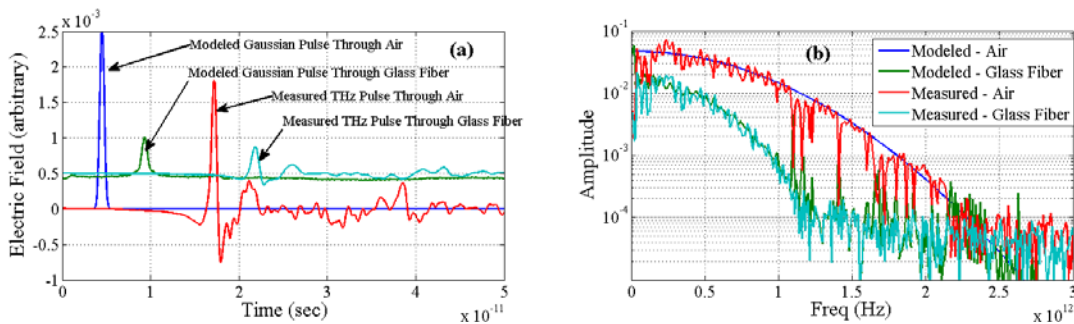


**Figure 15. Comparison of a Gaussian modeled THz pulse through air and glass fiber compared to THz TDS measurements for air and glass fiber in the (a) time domain and (b) frequency domain.**

### 3.1.4 System Setup Challenges

The most challenging part of collecting data from a THz TDS system is the alignment of the optical components with the near-infrared laser and the terahertz beam. The laser has to be aligned with the photoconductive switch antenna and with the detector (either a photoconductive switch or an electro-optic crystal). Then the THz beam had to be aligned through the optical system of parabolic mirrors to maximize the THz pulse received at the detector. One piece of equipment that was essential to the THz beam alignment was a pyroelectric detector. This pyroelectric detector could be used to maximize the beam intensity at each of the optical components before locking them into place and helped to manage the many degrees of freedom that existed in the alignment problem. A HeNe laser could be used to initially help align the near-infrared Ti:Sapphire laser with the emitter and detector. Then fine-tuning of the position of the laser spot could be steered by measuring the resistance of the emitter and detector. The laser power sent to the pump and probe beams also had to be closely monitored so that the maximum specifications were not exceeded. A list of the specifications that were measured are listed in Table 3.

**Table 3. List of Specifications for Ekspla photoconductive switch components.**

Measurement	Measured Value	Maximum Limit/ Expected Value
Emitter Dark Resistance	Infinite	Infinite
Emitter Illuminated Resistance	3.1 M $\Omega$	8 M $\Omega$
Detector Dark Resistance	68 M $\Omega$	67 M $\Omega$
Detector Illuminated Resistance	1.3 M $\Omega$	0.8 M $\Omega$
Pump Laser Power	125 mW	125 mW
Probe Laser Power	50 mW	50 mW
Power Supply Voltage	50 Volts	50 Volts
Power Supply Modulation	120 kHz	50 kHz

Significant effort was expended to align the Ekspla photoconductive detector, before it was considered damaged or unusable. The pulse widths that were measured were much wider in the time domain and much lower in amplitude than the advertised values in the Ekspla manual. Figure 16 shows the (a) THz pulse and its (b) amplitude spectrum measured at the photoconductive switch receiver. In the time domain, the main pulse was spread out over 6 psec and several oscillations proceeded for a long duration after the main pulse.

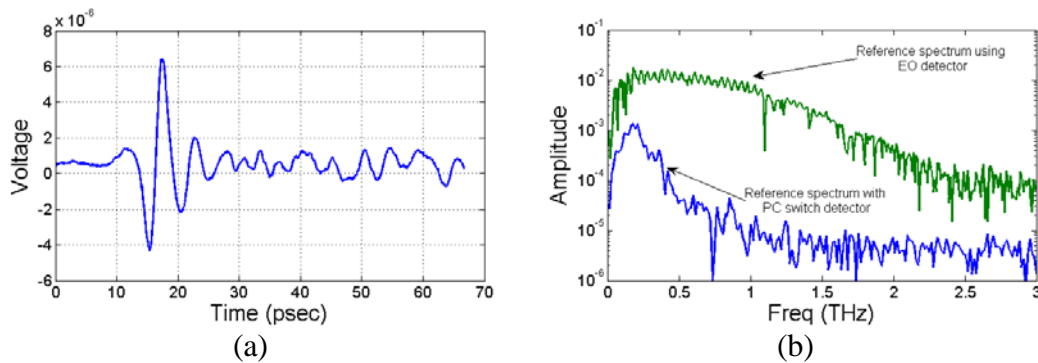


**Figure 16. THz pulse measured with photoconductive (PC) switch detector: (a) time domain pulse and (b) frequency domain spectrum compared to electro-optic detector.**

It was also two orders of magnitude lower in amplitude than the pulse measured with the ZnTe crystal. This translated to a narrower bandwidth ( $\sim 0.7$  THz) and a reduced amplitude in the frequency domain. The energy in the pulse was determined by estimating the noise floor for each spectrum and then calculating the area under the curve above the noise floor for each spectrum separately. The total energy under the PC switch spectrum was only 2% of that under the EO detector spectrum.

### 3.2 Transmission Mode Measurements

This section outlines the results of our transmission mode measurements of optical parameters using THz TDS. The first two subsections show the calculation

techniques used to determine the material parameters and the results of those calculations. The last subsection shows how to use the Drude model to calibrate the material parameter measurements from the THz TDS system using a semiconductor.

### 3.2.1 Calculation Technique

Although the theory for calculating materials parameters was discussed in section 2.4.1, the practical technique used in this research for determining indices of refraction and absorption coefficients is outlined in this section. The index of refraction  $n(\omega)$  was calculated using the following equation

$$n(\omega) = 1 + \frac{c[\phi_{sam}(\omega) - \phi_{ref}(\omega)]}{\omega d_{sam}} \quad (66)$$

where  $\phi$  is the phase of the sample (*sam*) or the reference (*ref*),  $c$  is the speed of light, and  $d_{sam}$  is the sample thickness. One of the challenges of using this formula was to accurately unwrap the phase data linearly between the sample and reference since software routines alternate between  $-\pi$  and  $+\pi$ . The absorption coefficient  $\alpha(\omega)$  could be calculated using the following formula

$$\alpha(\omega) = -\frac{2}{d_{sam}} \ln \left[ \frac{|E_{sam}(\omega)|}{T(\omega)|E_{ref}(\omega)|} \right] \quad (67)$$

in which  $|E_{sam}(\omega)|$  is the magnitude of the THz field collected through the sample, and  $|E_{ref}(\omega)|$  is the magnitude of the THz field collected through air.  $T(\omega)$  is the fraction of the power transmitted through the air-sample interface given by

$$T(\omega) = \frac{4n(\omega)}{(n(\omega)+1)^2}. \quad (68)$$

The index of refraction and the absorption coefficient could be determined with an iterative process, solving both of them simultaneously at each frequency component. Since the absorption coefficient calculations were somewhat noisy, a windowing filter could be applied which averaged the ten nearest data points at each frequency.

When making material parameter measurements, one must also pay attention to the dynamic range DR of the THz TDS setup. The largest absorption coefficient that can be measured reliably with a given DR corresponds to the situation in which the sample signal is attenuated to a level equal to the noise floor:

$$\alpha_{\max} d = 2 \ln \left[ DR \frac{4n}{(n+1)^2} \right]. \quad (69)$$

If the absorption coefficient exceeds  $\alpha_{\max}$  then the analysis will show an apparent absorption coefficient equal to  $\alpha_{\max}$ . The index of refraction is not subjected to the same limitations [35].

Experimental uncertainty or error is another consideration in making calculations with measured data. One must first estimate the measurement error for all of the potential sources, given as  $\delta x$ ,  $\delta y$ , etc. If the source of uncertainty is from a standard deviation, it can be adjusted by the factor  $1/\sqrt{n}$  if  $n$  is the total number of runs. Once this is accomplished then the total error  $\delta f$  of a function  $f$  can be expressed by

$$\delta f = \sqrt{\left(\frac{\partial f}{\partial x}\right)^2 \delta x^2 + \left(\frac{\partial f}{\partial y}\right)^2 \delta y^2 + \dots}. \quad (70)$$

There are several potential sources of error with a summary of a few of them listed in Table 4.

**Table 4. Sources of error for THz material parameter measurements.**

Source of Measurement Error	Error Type	Error	Material Parameter Measurement Error
Amplitude Accuracy of Frequency Spectrum	Amplitude (std dev – 10 measurements)	$\pm 3.29\%$ @ 0.2 THz $\pm 5.7\%$ @ 0.5 THz $\pm 4.46\%$ @ 1 THz $\pm 40.7\%$ @ 2 THz	Absorption coefficient
Phase Accuracy of Frequency Spectrum	Phase (std dev – 10 measurements)	$\pm 1.01\%$ @ 0.2 THz $\pm 2.5\%$ @ 0.5 THz $\pm 0.15\%$ @ 1 THz $\pm 14.2\%$ @ 2 THz	Index of refraction
Sample thickness	Length	$\pm 0.01$ mm (w/calipers), $\pm 1$ mm (w/ruler)	Index of refraction and Absorption coefficient
Sample angle	Angle from normal	$\pm 5$ degrees	Absorption coefficient $\pm 0.4\%$ amplitude
Optical delay line timing	Length repeatability	$\pm 5$ $\mu$ m	Index of refraction, Absorption coefficient $\pm 16.66$ femtoseconds

### 3.2.2 Measurement Results on Various Materials

Using the THz TDS setup in Figure 13, data was collected from numerous samples, including space shuttle tile, silicon wafers, aircraft glass fiber composite strips, an aircraft panel made with composites, plexiglass, and paper. The measurement technique from the previous section was then applied and the results are summarized in the following paragraphs. The first material that was measured was space shuttle tile, a sample that was borrowed from AFRL/RXLP. The sample was 5 cm in thickness and was composed of a mixture of 70-80% air and the remainder of silica. The sample was

scanned and the resulting pulses and amplitude spectra are shown in Figure 17. One can observe that the amplitude of the pulse is reduced and the pulse broadens after traveling

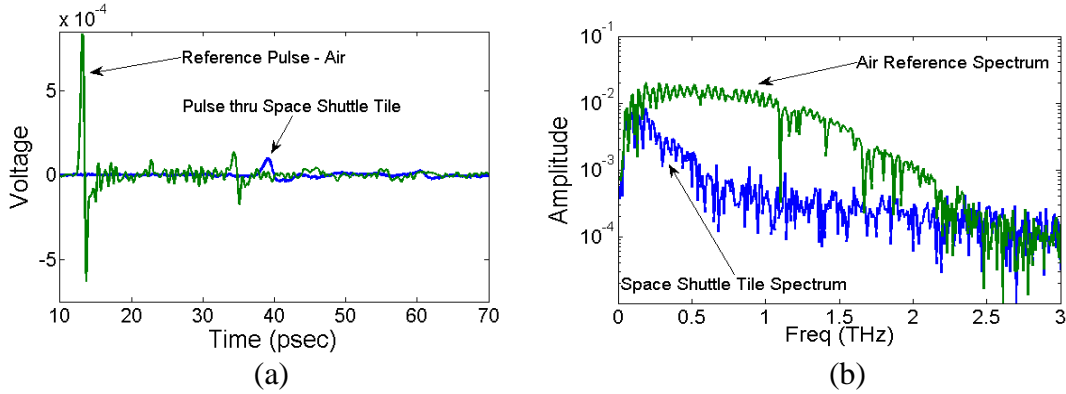


**Figure 17. THz TDS results through air & space shuttle tile: (a) THz pulse and (b) amplitude spectra.**

through the space shuttle tile. The bandwidth of the pulse is reduced from 2.5 THz down to 0.7 THz. The next step was to calculate the index of refraction and the absorption coefficient. The results are shown in Figure 18. The index of refraction remained constant at 1.16 over the range of 0.1 – 0.7 THz, while the absorption coefficient rose to  $0.9 \text{ cm}^{-1}$  at 0.5 THz and peaked at about  $1.4 \text{ cm}^{-1}$  at 0.7 THz. However, a calculation of  $\alpha_{\text{max}}$  in Figure 18b shows that the absorption measurements are only accurate until 0.72 THz. At this frequency, the dynamic range of the sample spectrum is insufficient to

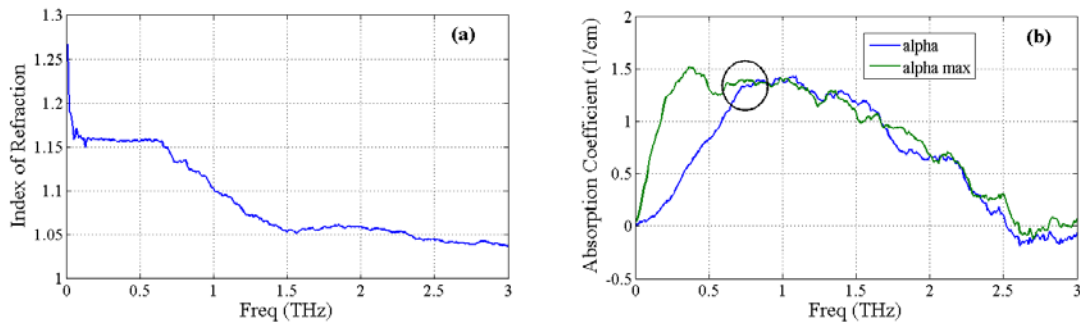


**Figure 18. Space shuttle tile calculations for (a) index of refraction and (b) absorption coefficient with a calculation for  $\alpha_{\text{max}}$ .**

measure the absorption coefficient and in the rest of the graph noise dominates the sample spectrum. Measurements in the THz frequency range on silica have been reported in the literature, ranging between 1.93 - 1.975 for refractive index and between 0.15 – 0.62 cm<sup>-1</sup> for absorption coefficient at 0.5 THz [51].

Since space shuttle tile is a mixture of silica and air, one would have to use an effective medium approximation to estimate the index of refraction for the space shuttle tile. Assuming that the true index of refraction for air is 1 and silica is 1.96, an estimate was made for the filling factor  $f$  for silica given our calculated index of 1.16. The results are summarized in Table 5. Since the Maxwell-Garnett Model is generally considered valid when  $f < 0.15$ , the Bruggeman Model appears to be the most accurate choice since it yields a filling factor estimate within the bounds of 70 – 80% air composition. Silica aerogel, a similar thermal insulating material consisting of silica and air, was measured with an index of refraction of ~1.03 and an absorption that ranged from 0.5 cm<sup>-1</sup> at 0.5 THz to 1.3 cm<sup>-1</sup> at 1.0 THz [91].

**Table 5. Summary of results for effective medium approximations on space shuttle tile at 0.5 THz.**

Effective Medium Model	Mathematical Formula	Silica Filling Factor ( $f$ ) Estimate
Linear Model	$\epsilon_{eff}(\omega) = f\epsilon_i(\omega) + (1-f)\epsilon_h(\omega)$	12.5%
Maxwell-Garnett Model (Valid: $f < 0.15$ )	$\epsilon_{eff}(\omega) = \epsilon_h(\omega) \left\{ \frac{1 + 2f \left[ (\epsilon_i - \epsilon_h) / (\epsilon_i + 2\epsilon_h) \right]}{1 - f \left[ (\epsilon_i - \epsilon_h) / (\epsilon_i + 2\epsilon_h) \right]} \right\}$	21.5%
Bruggeman Model	$f \left( \frac{\epsilon_i - \epsilon_{eff}}{\epsilon_i + K\epsilon_{eff}} \right) + (1-f) \left( \frac{\epsilon_h - \epsilon_{eff}}{\epsilon_h + K\epsilon_{eff}} \right) = 0$	24%

In the earlier calculation of the absorption coefficient we assumed that all reduction in amplitude of the signal was due to absorption. It is also realistic to assess



that scattering plays an important role in a sample with a mixture of two substances with different dielectric constants. Using an average value of  $0.36 \text{ cm}^{-1}$  from the reported values for the absorption coefficient of silica and the equation in section 2.4.3, one could estimate the scattering mean free path to be approximately 1.2 cm at 1 THz.

A slice of a glass fiber composite from was also scanned with our THz TDS system so that material parameters could be estimated. The THz pulse was measured on the glass fiber sample (1.2 mm thickness) and then an FFT was performed to convert it into the frequency domain as illustrated in Figure 19a and b. The graphs showing the calculated index of refraction and absorption coefficient are shown in Figure 19c and d. The measured value of refractive index is constant across the frequency spectrum at 2.05, while the absorption coefficient increases to  $7 \text{ cm}^{-1}$  at 0.5 THz and  $25 \text{ cm}^{-1}$  at 1.0 THz. A plot is also shown in 19d which shows  $\alpha_{\text{max}}$  for the glass fiber. The highest frequency at which there is sufficient dynamic range in the sample spectrum is at about 1.25 THz. This calculation neglects any affects of scattering. Other attempts to measure fiber glass have yielded a refractive index of 2.05 – 2.1 and an absorption coefficient of  $7 \text{ cm}^{-1}$  at 0.5 THz and  $25 \text{ cm}^{-1}$  at 0.8 THz [66].

Another material that was measured was an entire aircraft panel. The panel was approximately 2.8 cm in thickness and two thin layers of glass fiber surrounding a thicker layer of honeycomb material in the middle. Only a very limited amount of THz energy at the lower end of the THz spectrum penetrated the material and no further analysis was attempted. Plexiglass was also scanned, and the resulting index of refraction was calculated as 1.55, compared with a published optical value of 1.48. A paper notebook was also measured, resulting in an index of 1.45 compared with wood, which was been

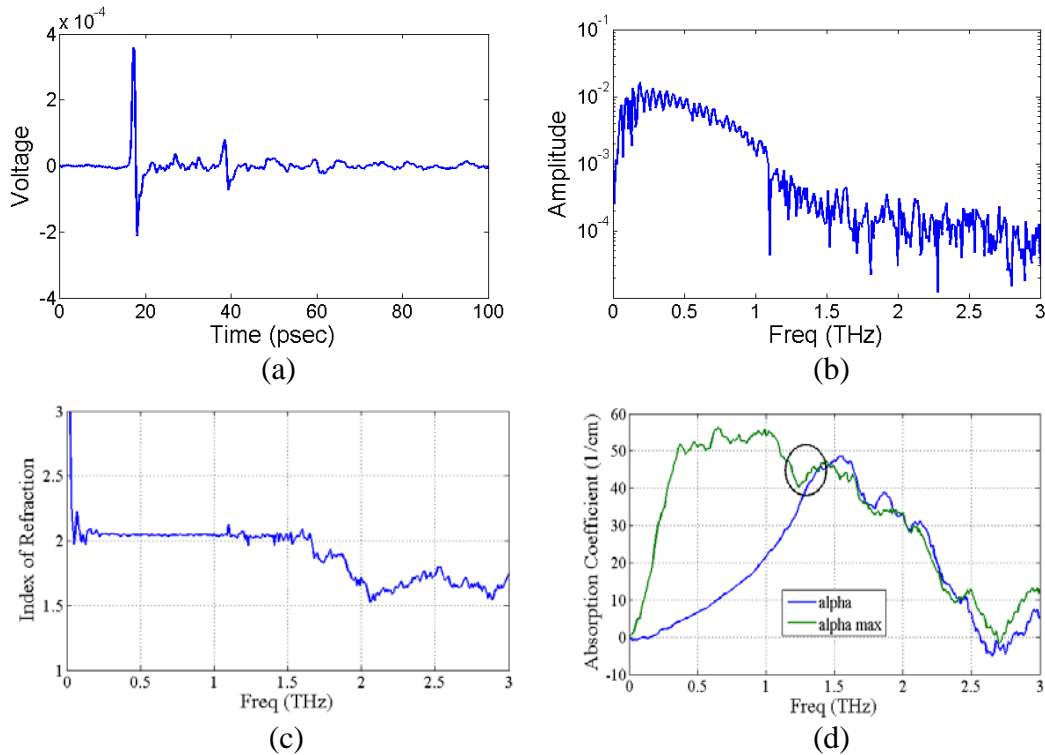


**Figure 19. THz pulse measured through glass fiber: (a) time domain, (b) frequency domain, (c) index of refraction, and (d) absorption coefficient with  $\alpha_{\max}$  included.**

measured in the lower end of the THz region as 1.35. When sheets were removed from the notebook, the spectral energy under the curve changed in proportion to the number of sheets that were removed.

### 3.2.3 Effective Medium Approximation and Scattering Analysis

Using a combination of effective medium theory and scattering theory in conjunction with THz TDS measurements, the propagation of THz through a glass fiber composite can be explained. First, the material properties of weaved glass fiber, polyimide resin, and the glass fiber composite were measured separately using THz TDS. Next, effective medium approximations for the composite were used to show the correlation between the composite and its components. Finally, scattering theory

calculations were made to show the minimal contribution of scattering to the extinction coefficient.

In our system, the glass fiber weave was considered as the inclusion and the polyimide was the host material. The glass fiber weave is made up of individual cylinders of glass that are approximately 10  $\mu\text{m}$  in diameter and much smaller than the THz wavelength. These cylinders are then bundled together into groups that were about 520  $\mu\text{m}$  in width which are then used to weave the overlapping pattern used in the composite. The polyimide resin is added and permeates throughout the individual glass fiber strands. The glass fiber volume concentration is typically between 40 – 60% depending on the type of technique used for combining the two components.

In an effort to determine the scattering effects of THz radiation in a glass fiber composite, samples of polyimide and glass fiber weave were prepared. The material parameters were determined first using THz TDS and thickness measurements. The results for polyimide (0.85 mm thick) in Figure 20 show a refractive index that remained fairly constant around  $1.81 \pm 0.03$  and absorption coefficients of  $3 \pm 2 \text{ cm}^{-1}$  (0.5 THz),  $8 \pm 2 \text{ cm}^{-1}$  (0.8 THz), and  $11 \pm 2 \text{ cm}^{-1}$  (1.0 THz).

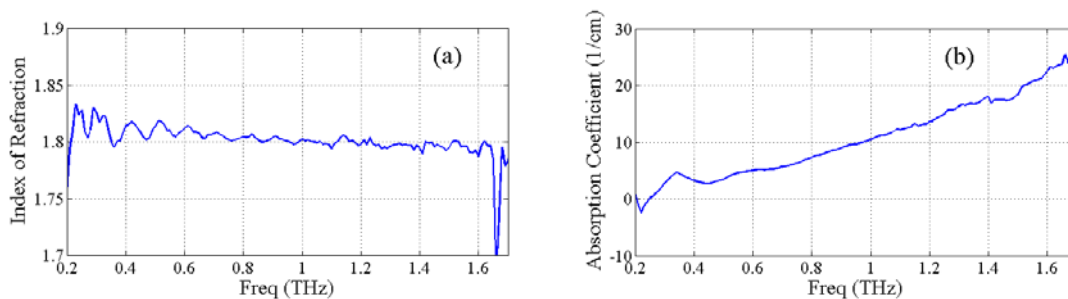


**Figure 20. THz TDS material parameter measurements using actual thickness measurements from polyimide showing (a) index of refraction and (b) absorption coefficient.**

It was difficult to obtain a thickness measurement on the weaved glass and therefore the refractive index and absorption coefficient in the THz region could not be accurately measured. Other measurements have been made on a variety of glasses in the THz frequency range [51], but no information is yet available on the glass used in this research. One of the most common types of glass used in aerospace glass fiber components is S-2 glass. A literature source reported an index of refraction of 2.21-2.30 at 1 MHz [18]. However, since the glass fiber composite could be measured, effective medium theory was used to estimate the approximate dielectric properties of the glass. Then the glass and polyimide measurements were used to estimate the effects of scattering in the glass fiber composite. Using the Bruggeman model with a glass fiber refractive index of 2.03, a polyimide index of 1.80, and assuming the composite is made up of 60% glass by volume (common for high performance composites), the refractive index for the glass was estimated to be 2.22. Another paper extracted the index of refraction for glass in a glass fiber composite in the THz frequency range to be 2.17 [65].

It would also be useful to determine the amount that scattering contributes to the extinction coefficient versus absorption. Since the diameters of the individual strands of glass (10  $\mu\text{m}$ ) are much smaller than the THz wavelengths used in this laboratory setup, the scattering analysis of infinitely long circular cylinders from section 2.4.3 is comparable to Rayleigh scattering for small spheres. Using the values of the refractive index, the value of  $m$ , which appears in section 2.4.3, was calculated to be 1.23. An estimate of the scattering coefficient for the glass fiber composite was then determined, assuming that the two perpendicular components of the scattering coefficient contributed equally,  $\bar{\sigma} = (\sigma_{TM} + \sigma_{TE})/2$ . This assumption was made based on the overlapping weave

pattern of the glass. The results of the scattering approximation are shown in Figure 21. Since the estimate was low in comparison to the extinction coefficient presented in Figure 19, scattering was considered to be insignificant in the glass fiber.

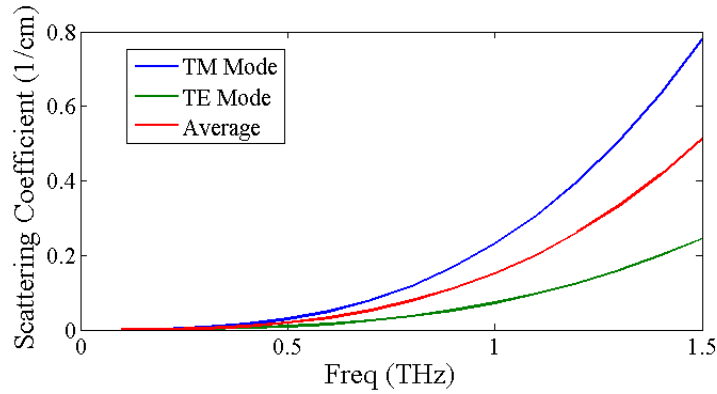


**Figure 21. Scattering coefficient calculation for glass fiber in the THz frequency range.**

A further attempt was made to use the Bruggeman effective medium approximation to show the relationship between the absorption properties of the polyimide and the glass weave within the composite and to explain the scattering properties of the glass weave within the composite. Although the glass weave (in air) thickness could not be measured, two assumptions were made about its composition. The first was that the glass had an index of refraction of 2.22 and the second was that the weave was 60% glass and 40% air. By inserting these assumptions into the Bruggeman model, the glass and air mixture was calculated to have a refractive index of 1.73. One could then analyze the data and modify the thickness until this index was obtained. The extinction coefficient could then be determined at this thickness with the results shown in Figure 22a. One can see that there are two valleys located at about 0.45 THz and 0.9 THz. This corresponds to THz wavelengths of approximately 330  $\mu\text{m}$  and 660  $\mu\text{m}$  in air,

which is the same order of magnitude of the width of fiber bundles. This could indicate that Mie scattering from the fiber bundles is present in the glass weave and air mixture.

Using the absorption coefficient data collected for polyimide, one could then use the Bruggeman model to estimate the absorption/extinction coefficient of the composite. A comparison of the data from the Bruggeman approximation and the actual glass fiber composite data (without coating) is displayed in Figure 22b. The two are a close match and Bruggeman approximation shows the valleys from the glass weave/air mixture data. Then a calculation of the scattering coefficient was made for the glass weave and air mixture in Figure 22c, assuming the glass fiber is much smaller than  $\lambda$  and ignoring

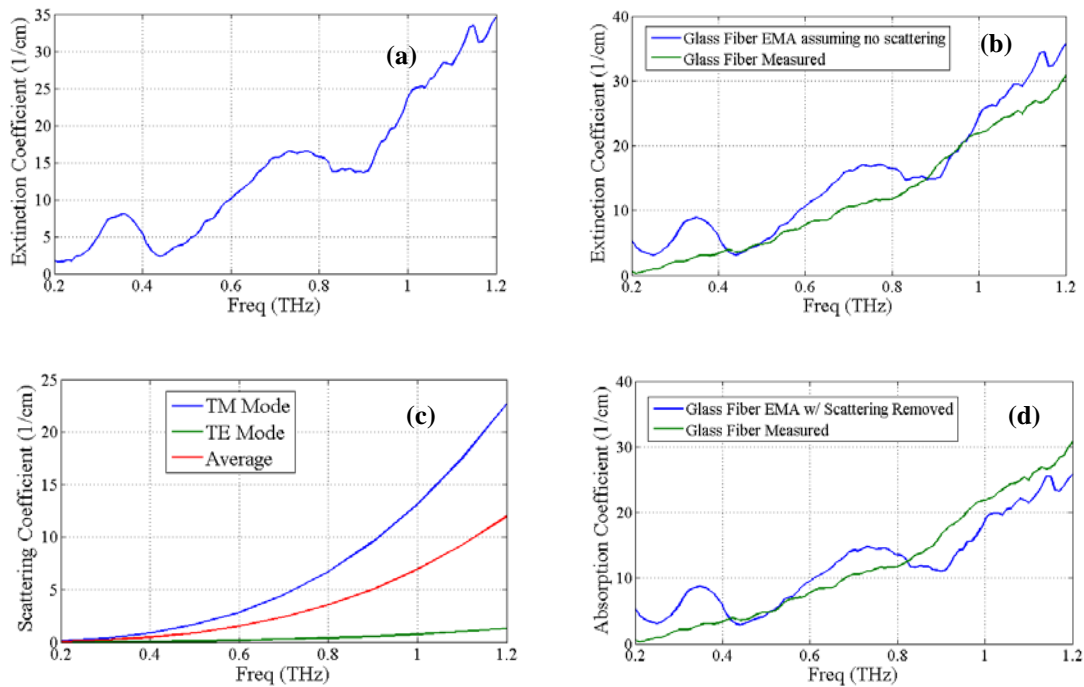


**Figure 22. (a) Extinction coefficient estimation on glass weave assuming an air-glass index mixture. (b) Comparison of the Bruggeman EMA for glass fiber extinction using polyimide and glass weave data vs. actual glass fiber extinction data. (c) Scattering coefficient calculations for the air and glass weave mixture. (d) Comparison of EMA for glass fiber using polyimide and glass weave (scattering removed) vs. glass fiber extinction coefficient.**

possible Mie scattering from the fiber bundles. Finally, the scattering from the glass-air mixture was removed in Figure 22d and the Bruggeman approximation is again compared to the actual composite data. The contribution of scattering to the extinction coefficient would be more significant for the glass weave/ air mixture than the composite due to the larger index gradient between glass and air. However, since the Bruggeman approximation for the extinction coefficient in 22b and 22d produced such close results with the actual glass fiber extinction data, it could not be determined whether the scattering from the individual cylinders of glass fiber contributes to the overall extinction coefficient.

### **3.2.4 Material Parameter Calibration**

For calibration of a material parameter measurement technique, one can use a material with absorption coefficient and refractive index properties that are well known. A material with a low absorption coefficient like teflon could be used to make measurements on the refractive index only. However, a semiconductor material like silicon could be used to calibrate both refractive index and absorption coefficient through the use of the Drude Model. One can use silicon in its high-resistivity form to calibrate the index of refraction and then use a more highly doped silicon sample to calibrate the absorption coefficient.

#### **3.2.4.1 Drude Model Predictions**

Silicon wafers have several specifications that are measured prior to sale, including thickness, resistivity, dopant, orientation, and whether it was polished. We

were looking for tight tolerances on resistivity and thickness so that we could model the optical parameters accurately. The first step was to use the Drude Model, explained in section 2.4.2, to predict the index of refraction and absorption coefficient for silicon. A series of samples with a wide range of resistivities were modeled and the results are shown in Table 6. The value used for  $\epsilon_{\infty}$ , the relative dielectric constant of undoped silicon, was chosen to be 11.68, even though published values ranged from 11.6 – 11.9. The carrier density of the dopant could be estimated from graphs in the Sze text *Semiconductor Devices: Physics and Technology* or from the website for Solecon Laboratories, while values for mobility of carriers could be estimated from graphs in the Sze text [73]. The fraction of THz that would be transmitted is given by

$$Fraction = \exp\left(\frac{-\alpha L}{2}\right) \left(\frac{4n_{Si}}{(n_{Si} + 1)^2}\right) \quad (71)$$

which is important when choosing a wafer, since a thicker wafer with higher absorption rates will result in no THz radiation being detected. The thickness of high-resistivity

**Table 6. Drude Model parameters and predictions for Silicon at 1 THz.**

Sample/ Resistivity $\rho$ ( $\Omega$ -cm)	Thick- ness (mm)	Carriers, type/no. ( $\text{cm}^{-3}$ )	Carrier Mobility ( $\text{cm}^2/\text{V-s}$ )	Momentum Relax. Time $\tau$ , (ps)	Index of Refraction (n)	Absorption coefficient, $\alpha$ ( $\text{cm}^{-1}$ )	Fraction THz Trans.
7	0.250	p/ $1.9 \cdot 10^{15}$	430	0.06365	3.403	11.068	0.612
10	0.380	p/ $1.32 \cdot 10^{15}$	430	0.06365	3.408	7.679	0.607
19	1	p/ $6.9 \cdot 10^{14}$	430	0.06365	3.412	4.008	0.575
23	1	p/ $5.69 \cdot 10^{15}$	430	0.06365	3.413	3.305	0.595
40	6	n/ $1.09 \cdot 10^{14}$	1350	0.2	3.415	1.008	0.519
50	6	n/ $6.18 \cdot 10^{13}$	1350	0.2	3.415	0.801	0.552
100	6	n/ $4.32 \cdot 10^{13}$	1350	0.2	3.416	0.399	0.623
800	3	n/ $5.38 \cdot 10^{12}$	1350	0.2	3.4175	0.05	0.691
1100	3	n/ $3.91 \cdot 10^{12}$	1350	0.2	3.4175	0.036	0.694
4200	6	p/ $3.09 \cdot 10^{12}$	430	0.6365	3.4176	0.0179	0.698
10000	6	n/ $4.3 \cdot 10^{11}$	1350	0.2	3.4176	0.004	0.702
30000	1	p/ $4.32 \cdot 10^{11}$	430	0.6365	3.4176	0.0025	0.702
100000	1	p/ $1.3 \cdot 10^{11}$	430	0.6365	3.4176	$7.5 \cdot 10^{-4}$	0.702



silicon required to remove the Fabry-Perot oscillations is determined by the optical path length through silicon. A thickness of at least 6 mm is required to remove the oscillations from a 133 psec scan, assuming  $n_{Si} = 3.4176$ .

### 3.2.4.2 Silicon Measurements

The first silicon that we measured was a silicon wafer with an unknown resistivity and a measured thickness of approximately  $0.37 \mu\text{m}$ . The pulse was measured first and is shown in Figure 23a. One can see the first and second Fabry-Perot reflections from the sample. The Fourier transform of the pulse is shown in 23b. The Fabry-Perot reflections in 23a led to the oscillations in the refractive index and absorption coefficient spectra.

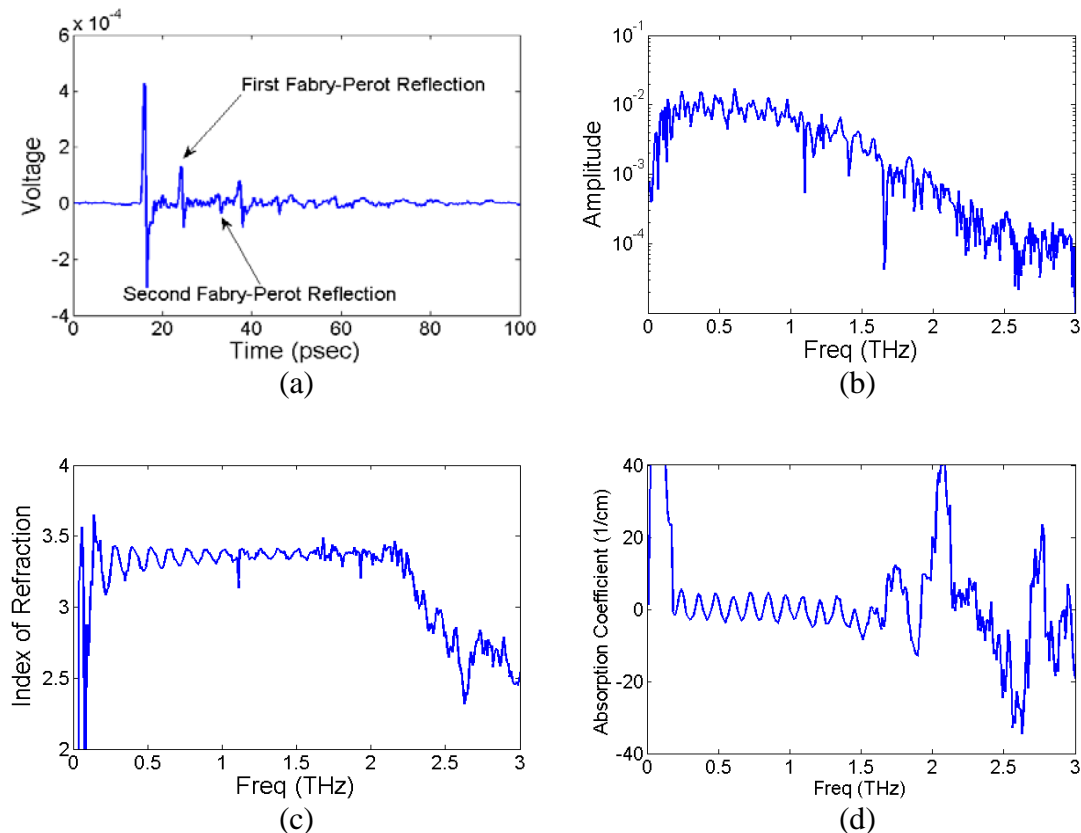


**Figure 23. Material parameter measurements on a silicon wafer: (a) THz pulse showing FP reflections, (b) THz spectrum, (c) index of refraction, and (d) absorption coefficient.**

The second piece of silicon that was tested was a piece of polished high resistivity silicon with a thickness of  $1.016 \pm 0.02$  mm and a resistivity of 30-100  $\Omega$ -cm. From this resistivity, the Drude Model prediction would be 3.4176 for the refractive index and  $0.0008 - 0.0025$   $\text{cm}^{-1}$  for the absorption coefficient. The pulse and spectrum data are shown in Figure 24a and 24b with the strong Fabry-Perot etalon effect in the frequency domain being a result of the reflections visible in the time domain. The index of refraction in 24c oscillates between 3.375 and 3.475 with an average of 3.425. The absorption coefficient 24d oscillates around 0  $\text{cm}^{-1}$ .

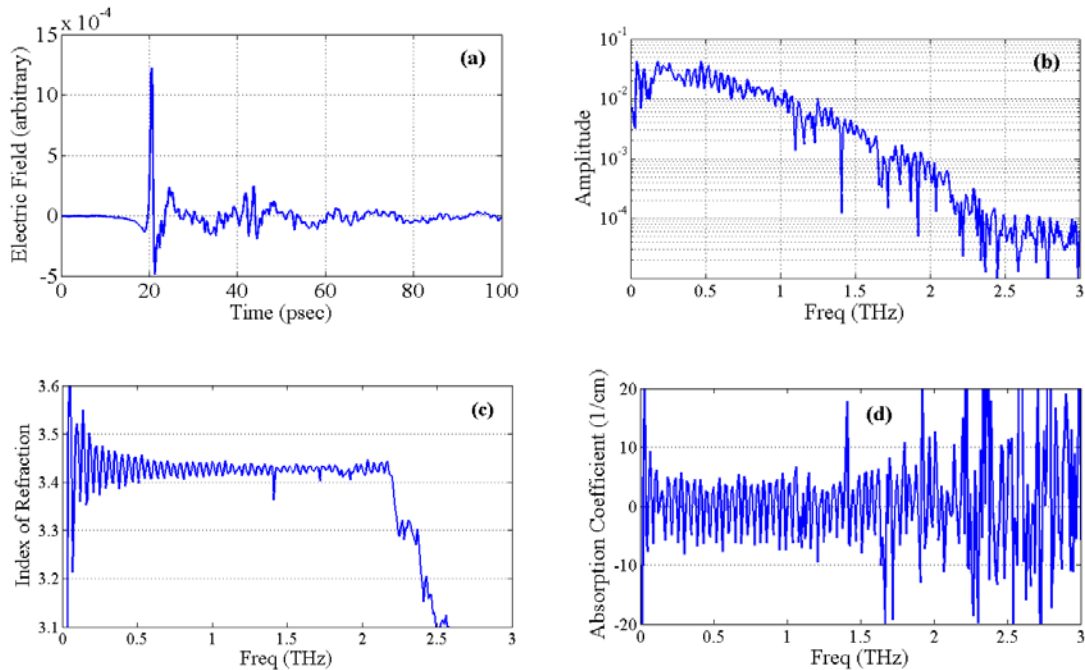


**Figure 24. Material parameter measurements on high resistivity silicon: (a) THz pulse, (b) THz spectrum, (c) index of refraction, and (d) absorption coefficient.**

The third piece of silicon was a thick piece of unpolished float zone (FZ) silicon with a thickness of  $6.0 \pm 0.1$  mm and an average measured resistivity of 4200  $\Omega$ -cm. Using the Drude model, the predicted index of refraction would be 3.4176 and the absorption coefficient would be  $0.02$   $\text{cm}^{-1}$ . Figure 25a and 25b shows the pulse and

spectrum data for the FZ silicon collected with the THz TDS setup with the first Fabry-Perot reflection shown at the far right of the time domain plot. The index of refraction in 25c was measured to be 3.416 and the absorption coefficient in 25d was approximately  $0 \text{ cm}^{-1}$ . These calculations and measurements can be compared to those made by Dai et. al. where their results were 3.4175 for the index of refraction and  $0.01 - 0.23 \text{ cm}^{-1}$  (0.5 – 4.5 THz) for the absorption coefficient for FZ silicon (39 mm thickness) from the same manufacturer [17].

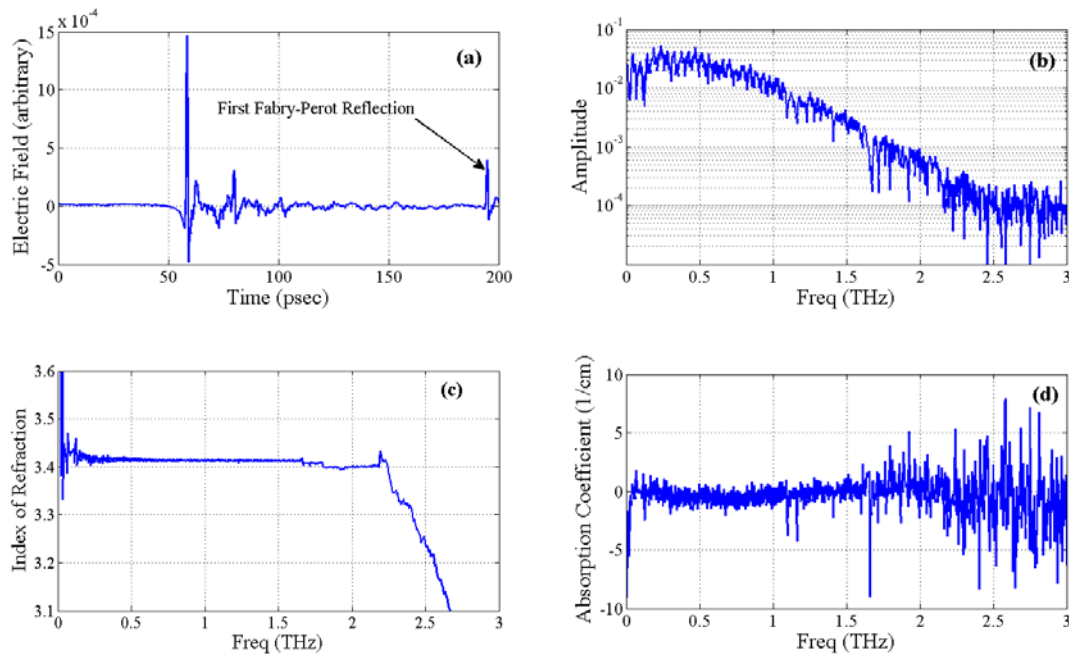


**Figure 25. Material parameter measurements on 6 mm thick float zone (FZ) silicon: (a) THz pulse, (b) THz spectrum, (c) index of refraction, and (d) absorption coefficient.**

### 3.2.5 Fabry-Perot Resonance Removal Techniques

One can attempt to remove the Fabry-Perot etalon effect illustrated in the previous section with one of three different techniques. One such technique is to window the pulse in the time domain, removing all of the etalon reflections that occur after the pulse. The problem with this technique is that the reduction in the total collection time of the pulse

causes the resolution of the THz spectrum in the frequency domain to be significantly reduced. This caused an inaccuracy in the unwrapping of the phase change required to calculate the index of refraction.

A second method of removing the Fabry-Perot etalon effect is to subtract out the reflections from the time domain pulse. One can obtain a THz field in the time domain that has removed the first two reflections, assuming that there is little or no absorption. In the following equation the measured THz field  $E_m(t)$  is multiplied by the reflected field at the air-silicon interfaces for the first two reflections to obtain the resultant field  $E_f(t)$ :

$$E_f(t) = E_m(t) - RE_m(t+d) + R^2E_m(t+2d). \quad (72)$$

In this equation,  $R$  is the reflectance and  $dt$  is the time between reflections, given by

$$R = \left( \frac{n-1}{n+1} \right)^2, \quad dt = \frac{2nd}{c} \quad (73)$$

where  $d$  is the thickness of the material. One can also observe the data and measure the time difference between the main pulse and the reflected pulses. An example of this FP etalon removal technique is demonstrated in Figure 26. A similar technique was used by Naftaly et. al. [52].

Another technique, introduced by Duvillaret et. al., uses an iterative process to remove the Fabry-Perot reflections in the frequency domain [79]. A block diagram describing the technique is in Figure 27. The first iteration starts with the basic equations to determine the index of refraction and absorption coefficient from section 3.2.1. The Fabry-Perot  $FP$  term represents the accumulation of all the etalon reflections through the

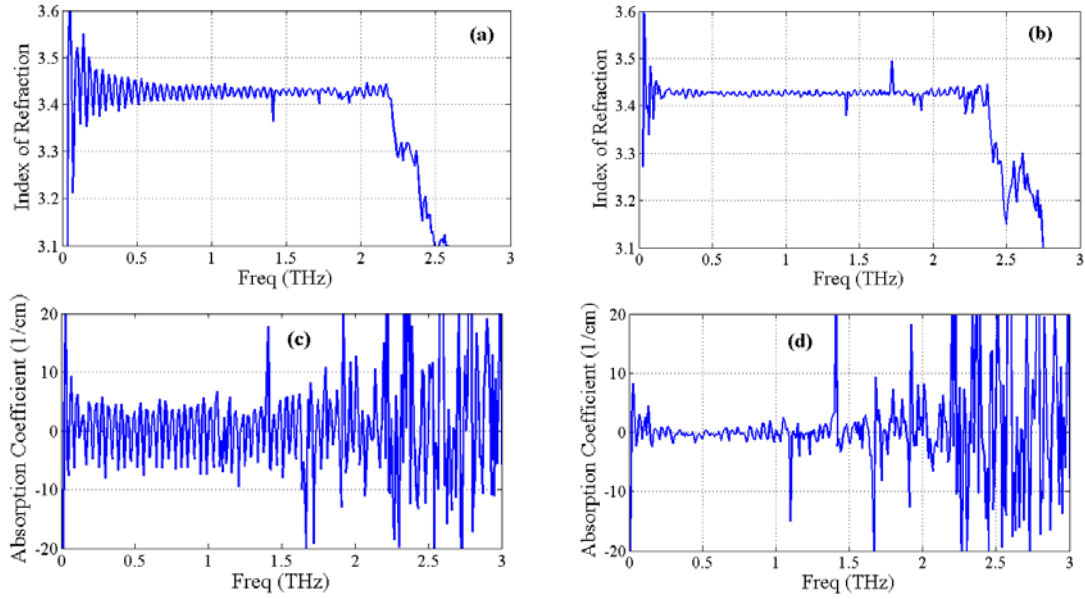


**Figure 26. Diagrams showing the removal of FP oscillations in the time domain: (a) index of refraction with FP oscillations, (b) index of refraction without first 2 FP oscillations, (c) absorption coefficient with FP oscillations, (d) absorption without first 2 FP oscillations.**

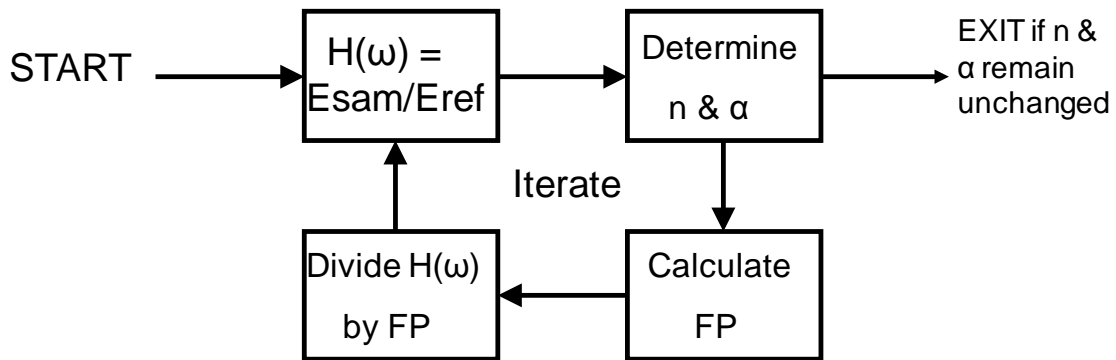


**Figure 27. Iterative process for removal Fabry-Perot etalon effect in frequency domain described by Duvillaret et. al.**

sample and is an expansion of the transmission equation from section 2.5.5.1

$$\frac{\tilde{E}_{sam}(\omega)}{\tilde{E}_{ref}(\omega)} = \frac{4\tilde{n}(\omega)}{[\tilde{n}(\omega)+1]^2} \exp\left\{-i\left[\tilde{n}(\omega)-1\right]\frac{\omega}{c}d\right\} \cdot FP. \quad (74)$$

This Fabry-Perot term is defined as:

$$FP = \frac{1}{1 - \frac{[\tilde{n}(\omega) - 1]^2}{[\tilde{n}(\omega) + 1]^2} \times \exp\left[-i2\tilde{n}(\omega)\frac{\omega}{c}d\right]} \quad (75)$$

where the index of refraction is a complex number, including the absorption coefficient.

On the next iteration, one divides  $E_{\text{sam}}/E_{\text{ref}}$  by FP and then re-calculates the optical parameters. The FP term is then readjusted and the process continues until the optical parameters stop changing. Results are shown in Figure 28 for the refractive index (a) and (b) and the absorption coefficient (c) and (d) after 5 iterations of the routine described above. In addition to Fabry-Perot removal techniques, efforts have been made to remove noise peaks caused by water vapor absorption lines and to remove spurious effects caused by the early truncation of a THz signal [28].

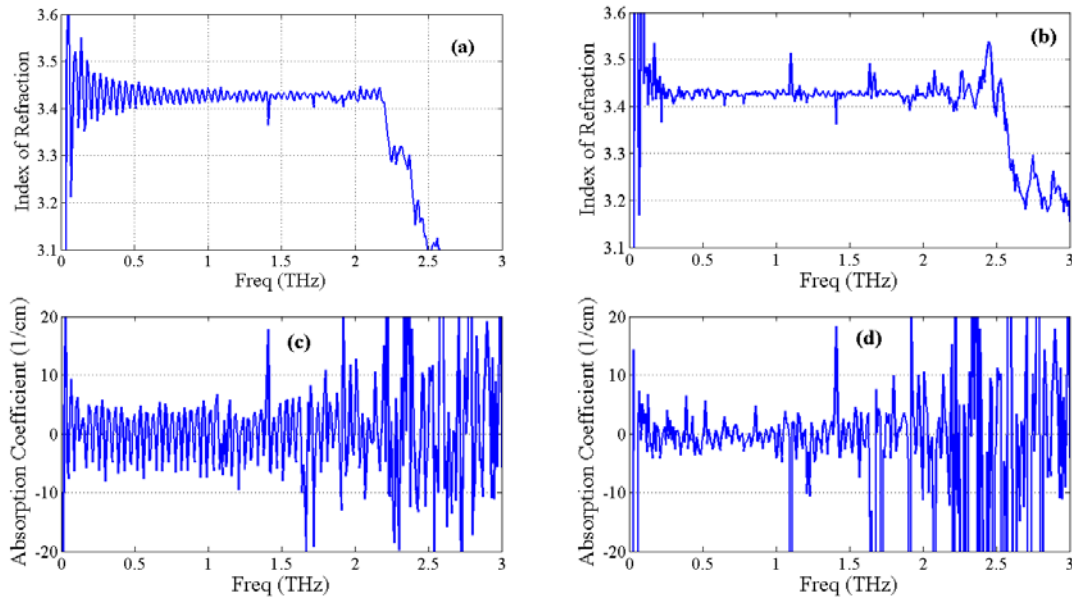


**Figure 28. Fabry-Perot oscillation removal technique showing the real part of the index of refraction (a) before & (b) removal, followed by the imaginary part of the index of refraction (c) before & (d) after the Fabry-Perot removal technique was applied.**

### 3.3 Reflection Mode Material Parameter Measurements

Most maintenance techniques limit the inspection of materials from only one side. Additionally, some materials are optically thick and therefore do not transmit radiation in the THz region. A different setup is needed to characterize these types of materials. The reflection mode THz TDS system used in this research is shown in Figure 29. For THz optics, it uses a 25 mm diameter ( $f = 25$  mm) parabolic mirror first, followed by four 50 mm diameter ( $f = 100$  mm) parabolic mirrors. The equation used to model reflection spectroscopy at normal incidence is given by

$$\frac{\tilde{E}_{sample}(\omega)}{\tilde{E}_{ref}(\omega)} = \frac{|\sqrt{R(\omega)}| \exp[-i\Delta\phi(\omega)]}{|\sqrt{R_{ref}(\omega)}| \exp[-i\Delta\phi_{ref}(\omega)]} = \frac{[1 - \tilde{n}(\omega)][1 + \tilde{n}_{ref}(\omega)]}{[1 + \tilde{n}(\omega)][1 - \tilde{n}_{ref}(\omega)]} \quad (76)$$

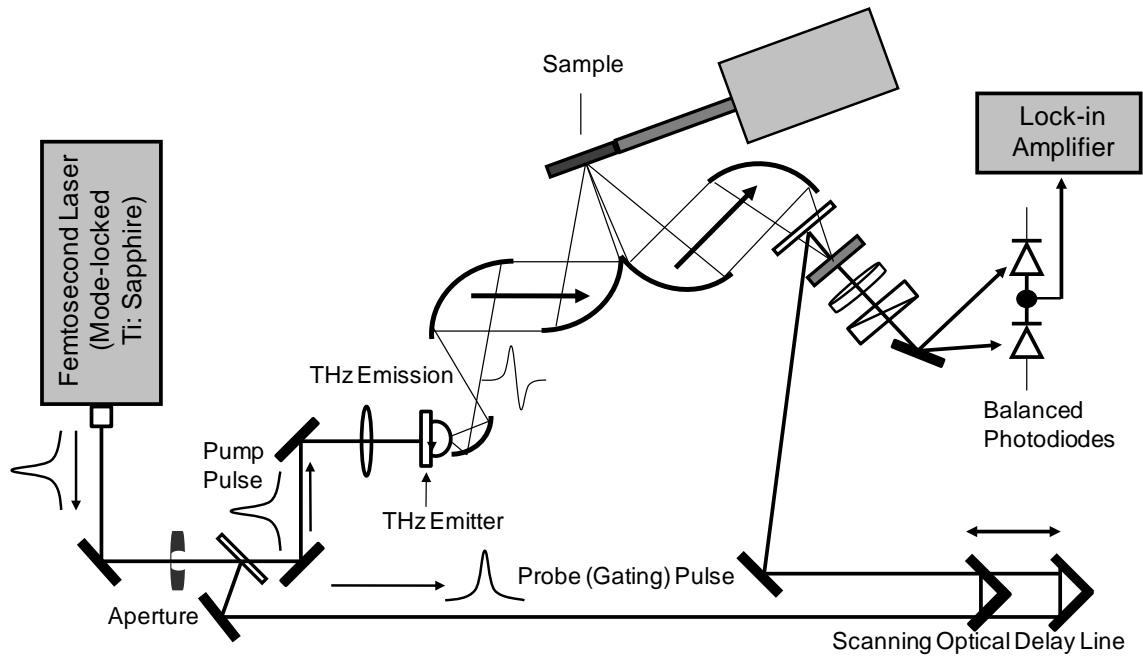


Figure 29. THz TDS reflection mode schematic.

where  $\tilde{n}_{ref}(\omega)$  is the refractive index of the reference mirror [67]. The surface of the reference mirror must be positioned at precisely the same location as that of the sample.

Any misalignment in the reference mirror will cause a severe error in phase and should be suppressed to less than 1  $\mu\text{m}$ . The misalignment problem in reflection measurements can be resolved by aligning the THz TDS system with attenuated-total-reflection and ellipsometry methods. One author provides dispersion relations in the analysis of experimental data from reflection spectroscopy to help remove the sample misplacement error [30]. A second paper presents the effects of surface roughness on the reflection spectra obtained from THz TDS [20]. A final paper shows a technique for measuring the alcohol content of an aqueous solution in a closed bottle using a reflection geometry [36].

### 3.3.1 Calculation Technique

If one uses a metallic mirror for the reference scan then the reflection coefficient is close to unity. In this case, the equation in the previous section reduces to

$$|r|\exp(i\phi) = \frac{\tilde{n}-1}{\tilde{n}+1} \quad (77)$$

in which  $r$  is the amplitude of ratio of the sample spectrum to the reference spectrum and the relative phase is  $\phi$  [35]. This equation can then be inverted and simple equations can be obtained for the index of refraction  $n$  and the absorption coefficient  $\alpha$ :

$$n(\omega) = \frac{1 - |r(\omega)|^2}{1 + |r(\omega)|^2 - 2|r(\omega)|\cos\phi(\omega)}, \quad (78)$$

$$\alpha(\omega) = \frac{4\pi\omega}{c} \frac{2|r(\omega)|\sin\phi(\omega)}{1 + |r(\omega)|^2 - 2|r(\omega)|\cos\phi(\omega)}. \quad (79)$$



A correction term is also needed to account for the angle of reflection for the THz TDS apparatus. The following term should be multiplied by both Equation 70 and 71 to account for the incident angle,  $\theta$ :

$$\angle Factor = \cos \left\{ \sin^{-1} \left[ \frac{\sin(\theta) / n}{\cos(\theta)} \right] \right\}. \quad (80)$$

Both the index of refraction and the absorption coefficient have terms with a phase dependence. In addition, the relative phase would have to unwrap in a manner in which the phase would stay relatively close to zero so that  $\cos(\phi) \approx 1$  and  $\sin(\phi) \approx \phi$ . Unfortunately, in practice the relative phase unwrapped in a way that quickly became greater than zero. It became apparent after several attempts that it would be impossible, with the current lab equipment, to maintain a consistent position of the sample and reference and therefore the required phase accuracy could not be obtained.

An alternate approach was attempted where the relative phase was assumed to change at a much slower rate by dividing the relative phase by  $10^5$  so it remained close to zero, but would still unwrap linearly. Since the relative amplitude  $|r(\omega)|$  was more consistent across the THz frequency spectrum, the index of refraction could be approximated using equation 78. The index of refraction for FZ silicon, determined using reflection mode, is shown in Figure 30a where the mean value is  $3.40 \pm 0.04$ , assuming an angle of  $20 \pm 2^\circ$ . Although the mean value is similar to the transmission measurement, the figure clearly shows a greater deviation about this mean. The absorption coefficient calculated using the small relative phase (unknown accuracy) is shown in 30b.

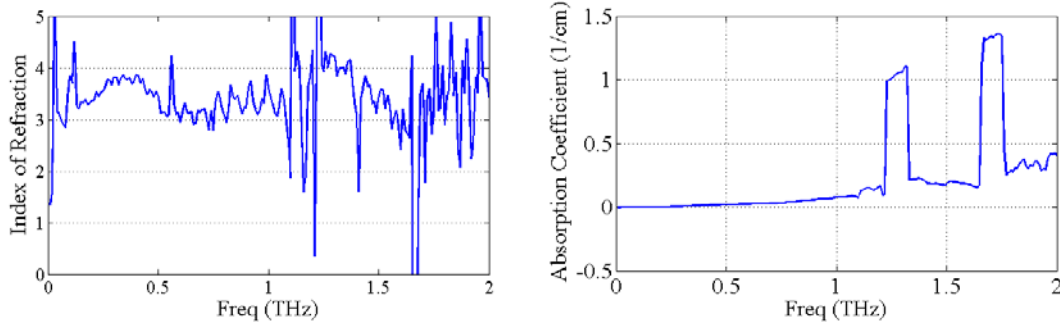


**Figure 30. Material parameter measurements using reflection configuration on 6 mm thick float zone (FZ) silicon: (a) index of refraction and (b) absorption coefficient.**

### 3.3.2 Practical Approximation of Material Parameters

Since the phase accuracy requirement was so difficult to meet when comparing a sample to a reference piece of aluminum, an alternate approach was attempted. Instead, the reflection off the back surface of the sample was compared with the reflection off the front side of the sample. An assumption was made that the index of refraction spectrum had a flat response and could be determined via a time of flight measurement. Then the absorption coefficient could be determined using this index of refraction measurement. The easiest way to test this method was by using the thickest piece of FZ silicon so that the effects of the ZnTe Fabry-Perot reflections would not interfere with the back reflection. The results of the pulse are shown in Figure 31a. The index of refraction  $n$  was calculated using the following formula:  $n = (T_b - T_f)c/2d$  where  $T_b$  is the time of arrival of the back pulse and  $T_f$  is the time of arrival of the front pulse. One can notice that the polarity of the back reflection is the opposite of the front reflection due to the  $\pi$  phase shift encountered when reflection from the first air-to-glass fiber interface. Using the measured thickness  $d$  of 6.0 mm, the calculated value of  $n$  was 3.418 which was very close to the values reported for transmission configuration and for the Drude model.

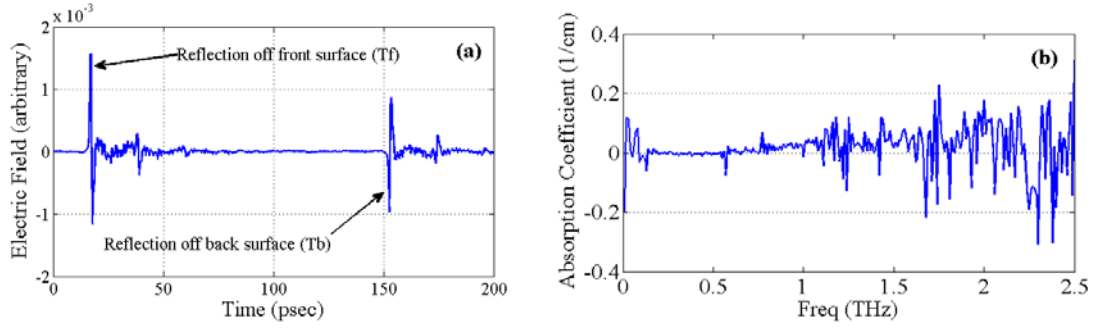


**Figure 31. THz TDS reflection setup for thick FZ silicon: (a) pulses off front and back surface and (b) absorption coefficient using Fourier transform from each pulse.**

Since the pulses were sufficiently separated in time, one could split the 200 psec time period in half, and take the Fourier transform of each half. The absorption coefficient is then calculated like in transmission setup, except that the Fresnel reflections are different. A diagram showing the geometry of the Fresnel reflections in reflection setup is shown in Figure 32. The following equation shows how to determine the absorption coefficient  $\alpha$  from the two reflected pulses:

$$\alpha(\omega) = -\frac{2}{d_{sam}} \ln \left( \frac{|E_{sam}(\omega)|}{R(\omega)|E_{ref}(\omega)|} \right). \quad (81)$$

The term  $R(\omega)$  is defined based on the geometry in Figure 32 as

$$R(\omega) = \frac{t_{12}(\theta_1)t_{21}(\theta_1)r_{23}(\theta_1)}{r_{12}(\theta_1)} \quad (82)$$

where the coefficients are defined according to

$$r_{12} = \frac{n_1 \cos(\theta_1) - n_2 \cos(\theta_2)}{n_1 \cos(\theta_1) + n_2 \cos(\theta_2)}, \quad t_{12} = 1 + r_{12} \text{ and} \quad (83)$$

$$r_{23} = \frac{n_2 \cos(\theta_2) - n_3 \cos(\theta_3)}{n_2 \cos(\theta_2) + n_3 \cos(\theta_3)}, \quad t_{21} = 1 + r_{21}. \quad (84)$$

The absorption coefficient could then be calculated as shown in Figure 32b. It remained close to  $0 \text{ cm}^{-1}$  and shows some similarities to the transmission configuration graph.

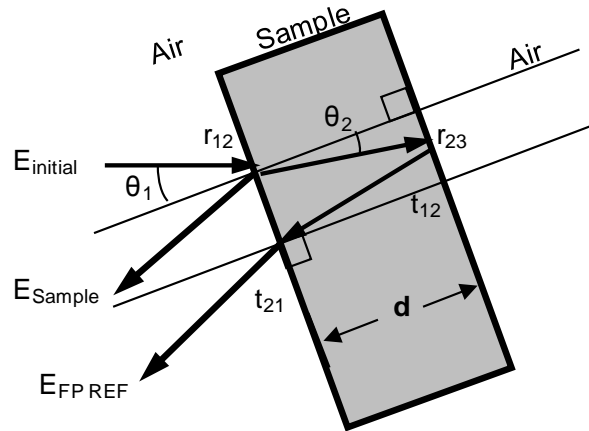
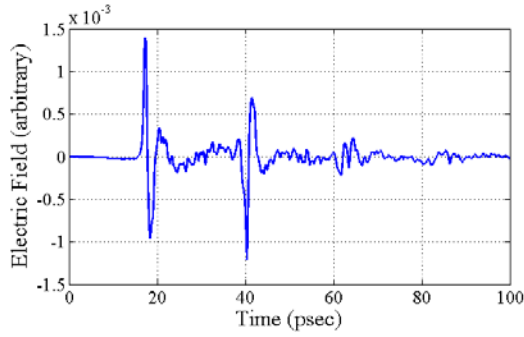


Figure 32. Diagram showing the geometry of the first Fabry-Perot reflection from the sample in reflection configuration.

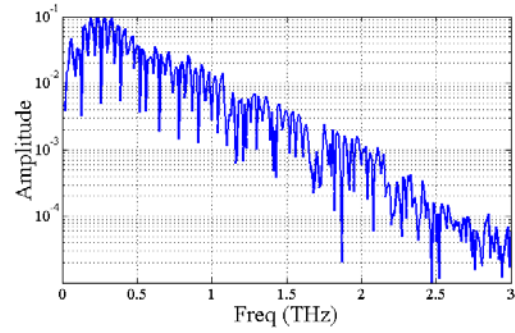
### 3.3.3 Other Material Parameter Measurements

In the previous two sections, the thick piece of FZ silicon, with a significant time separation before the first FP reflection, was used to test two methods of extracting material measurements using a THz TDS reflection configuration. In this section, material parameter measurements were attempted on the high resistivity silicon and finally on the glass fiber in an effort to find a useable reflection technique.

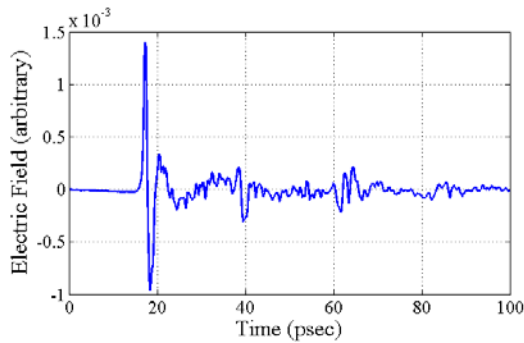
The first material analysis was performed on the high resistivity silicon. Figure 33 shows the THz (a) pulse return and the (b) spectrum with the effects of the Fabry-Perot reflections from both the sample and the ZnTe. This made it difficult to determine the index of refraction from Equation 78. To determine the material parameters, the first



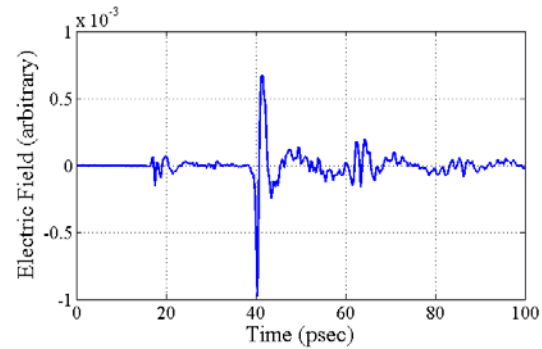
(a)



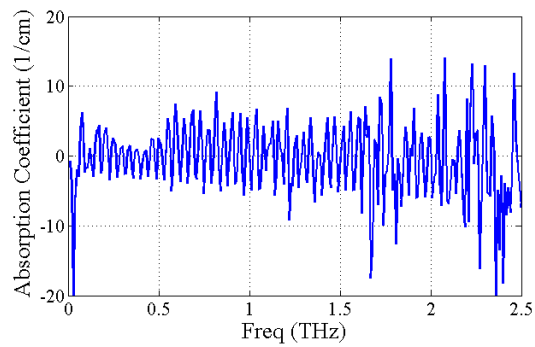
(b)



(c)



(d)



(e)

**Figure 33. THz TDS reflection (a) pulse and (b) spectrum for 1.016 mm high resistivity silicon. Isolation of the (c) front reflected pulse and the (d) back side reflected pulse in the time domain. The (e) absorption coefficient for high resistivity silicon measured using the spectrum of the front and back pulse.**

technique that was attempted was to measure the index of refraction with the time delay of the THz pulse between the front and back reflections. The index was measured to be

3.405 from either the peak of the pulse or the zero crossing. In order to measure the absorption coefficient, a separate Fourier transform would have to be taken for both the front and the back reflection. First, the front pulse was multiplied by the factor from Equation 82 (-0.686) and then subtracted from the back reflection shown in 33c. Then the reference pulse was multiplied by the Fresnel reflection coefficient (0.546) and subtracted from the front reflected pulse for 33d. The Fourier transform of each was taken and the result is shown in 33e. The result oscillates about zero from 0.1 - 1.2 THz.

The material measured next was the glass fiber composite without an exterior coating. The glass fiber was unique from the silicon samples in that it had a considerably higher absorption. The THz pulse in Figure 34a data was taken with the TDS reflection setup. A first attempt was made to measure the index of refraction using the timing between the front and back reflections, however, the index measurements were lower than in transmission configuration. An alternate method was tried using the relative amplitude of the pulses measured peak-to-peak. The amplitude of the first glass fiber pulse (1.5133) to the aluminum reference pulse (4.2124) was measured to be 0.3592. Using the equation for the Fresnel reflection coefficient from the front surface, the index of refraction was calculated to be  $2.03 \pm 0.02$ . With this index of refraction, the absorption coefficient was calculated using the method outlined in section 3.3.2. The graph in 34b shows the Fabry-Perot etalon effect in the glass fiber, while the graph in 34c is filtered using a windowing technique. The coefficient was measured to be  $7 \pm 2 \text{ cm}^{-1}$  at 0.5 THz and  $18 \pm 2 \text{ cm}^{-1}$  at 1.0 THz which were close to the results for transmission. The measurement appears to run out of dynamic range at approximately 1.0 THz, which makes it slightly worse than transmission which was at about 1.25 THz.

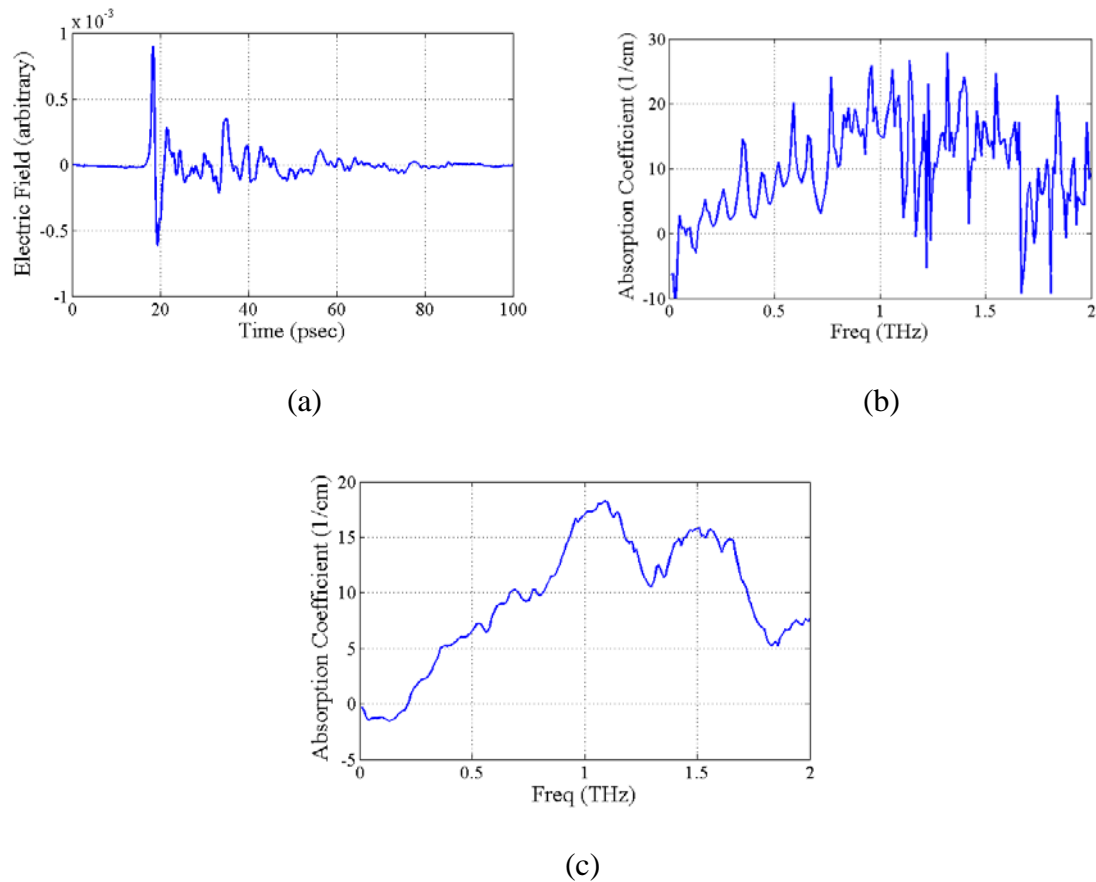


**Figure 34.** Plot of the (a) THz pulses reflected from the front and back of a glass fiber coupon. Absorption coefficient for the glass fiber (b) without filtering and (c) with filtering.

### 3.4 Burn Diagnostics Using THz TDS

One of the problems with designing aircraft is that the heat from jet engines can cause damage to the external structure of the aircraft. THz TDS could be used to measure the material properties of the aircraft glass fiber composites to determine if the composition of the material has fundamentally changed. Polyimide is a resin which has the characteristic of being very resilient to thermal loads, maintaining its properties for long periods of continuous use at 230°C, and for short excursions as high as 480°C.

Composite samples were prepared that were heated with various temperatures close to the maximum for polyimide for short durations.

### 3.4.1 Transmission Mode

One of the first steps that was taken in the nondestructive evaluation of damaged samples was to consider whether the material properties were altered in any way by the damage. Since the samples with heat damage on them were different than the previously measured glass fiber samples in Figure 19, we measured the THz pulse and amplitude spectrum for the sample and reference shown in Figure 35a and 35b. These damage samples had a coating applied to the exterior of the glass fiber which changed the properties slightly. The index of refraction for the unaltered composite remained

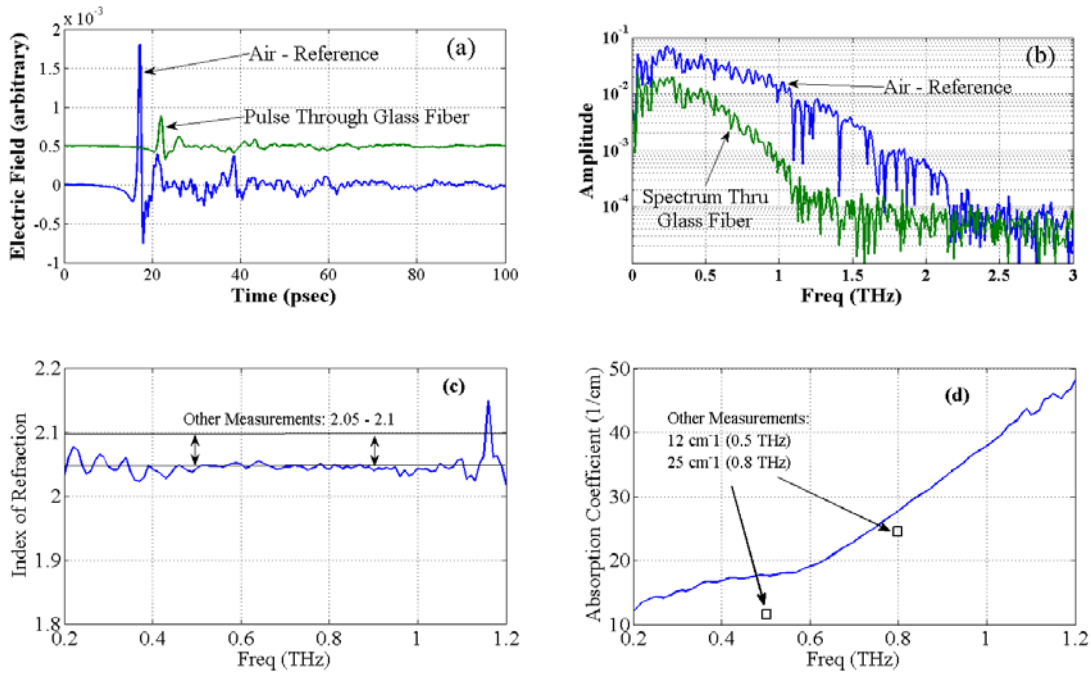


**Figure 35. THz TDS (a) pulse and (b) amplitude spectra for air reference and coated glass fiber. (c) Index of refraction and (d) absorption coefficient measurements for coated glass fiber in the THz frequency range.**



relatively constant in the THz frequency range at  $2.05 \pm 0.01$  in 35c while the absorption coefficient was measured as  $17.5 \pm 0.8 \text{ cm}^{-1}$  (0.5 THz),  $27.5 \pm 0.8 \text{ cm}^{-1}$  (0.8 THz) and  $38 \pm 0.8 \text{ cm}^{-1}$  (1 THz) shown in 35d. This is comparable to another measurement made on glass fiber samples, where the index of refraction was 2.05-2.1 and the absorption coefficient was  $12 \text{ cm}^{-1}$  (0.5 THz) and 26- 32  $\text{cm}^{-1}$  (0.8 THz) [4].

Using the setup shown in Figure 40, we measured an undamaged glass fiber sample followed by a series of damaged samples with heat damage. Thickness measurements were made on each of the samples and their burn areas, where the most visually noticeable difference was in the largest burn area ( $440^\circ\text{C}$  for 4 minutes). Using the measured thickness of each blistered area, we obtained the results in Figure 36 for the (a) index of refraction and (b) absorption coefficient. Figure 36 shows that there is a variation based on the thickness of the sample blister.

For comparison, the burned material parameter measurements were calculated with the undamaged sample thickness, such that the optical path length through each damage spot was constant. As is shown in Figure 37, two of the burn areas have

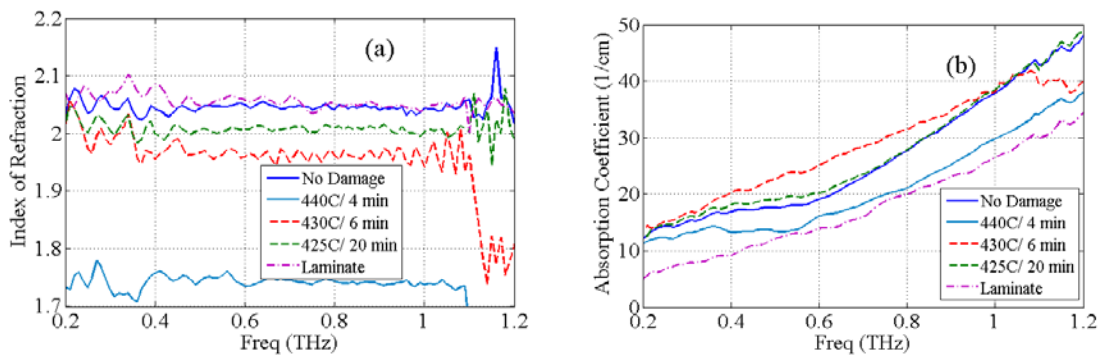


**Figure 36. THz TDS material parameter measurements using actual thickness measurements for burn damage areas showing (a) indices of refraction and (b) absorption coefficients.**

relatively the same optical path length as the undamaged area. The third damage area, burned at 430°C for 6 minutes, may have been different due to a small difference within the burn spot. There is an area in the center of the burn spot where there appears to be either a removal of the outer coating or a residue created during the burning process. Since it is in the center of the small burn spot it was not possible to ensure a THz TDS measurement could be made outside of the difference area. These measurements suggest that burning the samples at these high temperatures does not alter the material parameters, but merely introduces a blistering of the glass fiber and/or coating.

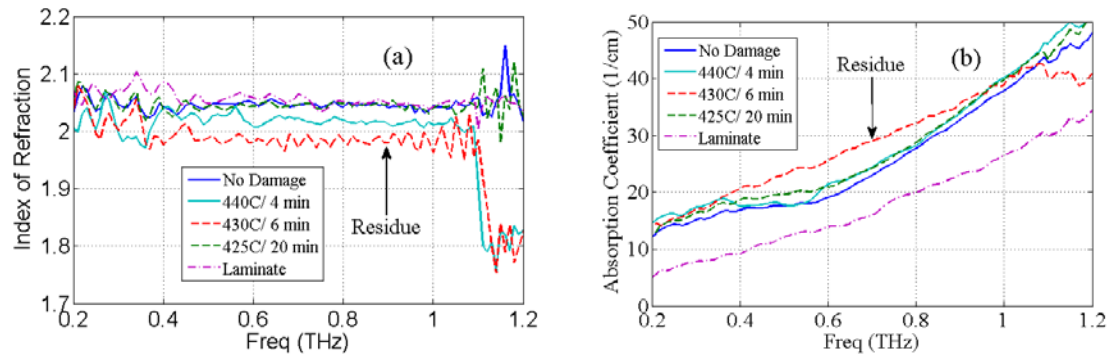


**Figure 37. THz TDS material parameter measurements, assuming the same thickness, for burn damage areas showing (a) indices of refraction and (b) absorption coefficients.**

### 3.4.2 Reflection Mode

Reflection configuration could also potentially be used for material parameter burn diagnostics on composites. A reflection technique would assume that the back side reflection of the THz would be large enough to use the technique described in section 3.3.3. However, an exterior coating was present on all three of burn spots available for this research, and this prevented most of the back reflection from being detected. A comparison of a reflected pulse from glass fiber both with and without the coating is

shown in Figure 38. Nearly double the amplitude is reflected from the coated sample due to the two reflections at the coating and composite surfaces. A very small back side reflection is evident in 38a for the coated sample. A burned area of the glass fiber without a coating would be required to test this technique.

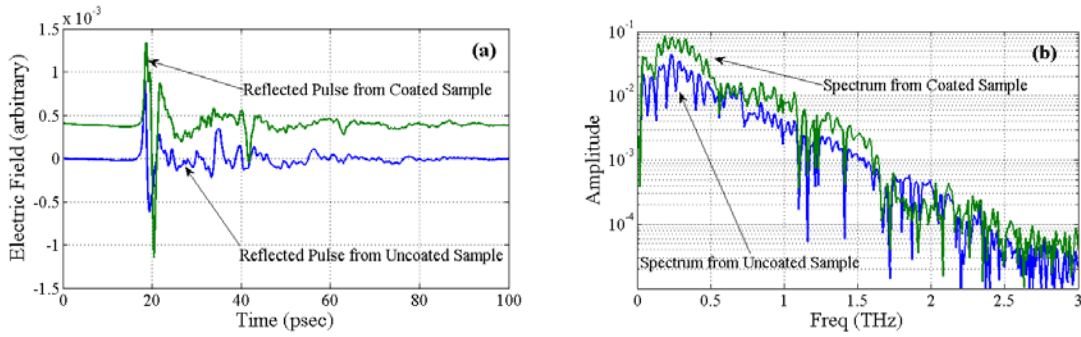


**Figure 38.** Comparison of the reflected signal from a coated and uncoated sample, showing the (a) time domain and (b) frequency spectrum returns.

## 4. THz Imaging for Nondestructive Evaluation

This chapter explains the results and analysis of imaging using THz TDS for the nondestructive evaluation of composites. It is divided primarily into a section on transmissive imaging and another section on reflection imaging. However, prior to analyzing the imaging results, there is an explanation of the samples and the setup, including sections on the numerical modeling and measurements of the THz beam at the sample position. Using each of the two imaging techniques, two-dimensional imaging was performed on the test samples. Finally, the last portion of each technique described the analysis of the depth of delaminations using THz TDS.

### 4.1 Sample Preparation

The composite samples that were provided by AFRL/RXLP to test representative forms of exterior aircraft damage are shown in Figure 39. The samples that were heated with various temperatures for short durations are labeled 2 and 3 in Figure 39. The first sample was burned at 440°C for 4 minutes, creating a blister on the sample about 2 cm X 1.5 cm. The second sample was burned in two places: 430°C for 6 minutes and 425°C for 20 minutes.

Another goal was to determine if various forms of damage could be imaged with a THz TDS system in either transmission or reflection setup. Three additional samples were prepared to test the ability of a THz TDS system to detect the damage. The first composite specimen, labeled 1 in Figure 39, was used as a thickness standard coupon to test the response of THz TDS imaging techniques to various sample thicknesses.

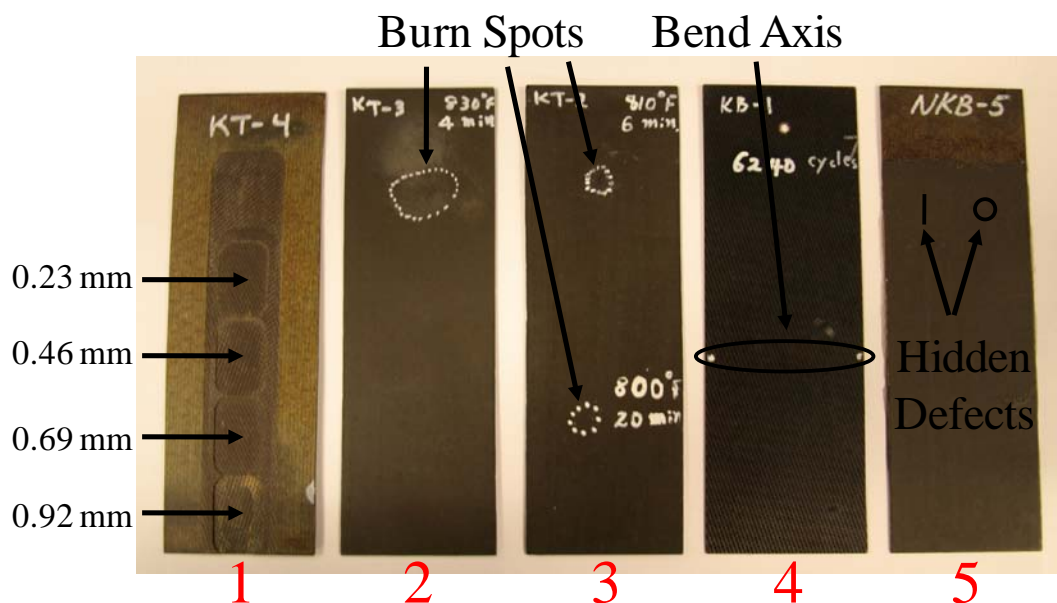


**Figure 39. Photograph showing the 5 glass fiber samples: (1) thickness calibration sample, (2) & (3) burn samples, (4) mechanical stress sample, and (5) hidden defect sample showing the hidden location of two of the eight defects.**

Another coupon, labeled 5, was prepared to search for flaws. This coupon consisted of two laminated pieces and is described in another reference [50]. The bottom piece was prepared by etching four layers and then creating a 6 mm slit and a 3 mm flat bottom hole (~70  $\mu\text{m}$  depth) in each of the four layers. A top layer was created by etching 4 layers with the same thicknesses and then attaching to the bottom layer in the opposite direction with epoxy, being careful not to allow any epoxy into the flaws. Finally, a third sample, labeled 4 in Figure 39, was prepared by bending a piece of glass fiber about a fixed axis a total of 6240 cycles to investigate mechanical damage with THz TDS imaging.

## 4.2 Transmission Mode Setup

The setup that was used for the THz TDS nondestructive evaluation and imaging is illustrated in Figure 40. A photoconductive switch was used for the THz emitter and

an electro-optic crystal (ZnTe) was used for the detector. This setup differed from the one used for material parameter measurement in that it used four off-axis parabolic mirrors to steer the THz beam, focusing it tightly at the sample. The first and last parabolic mirror had a diameter and focal length of 25 mm while the center two parabolic mirrors had a focal length and diameter of 50 mm.

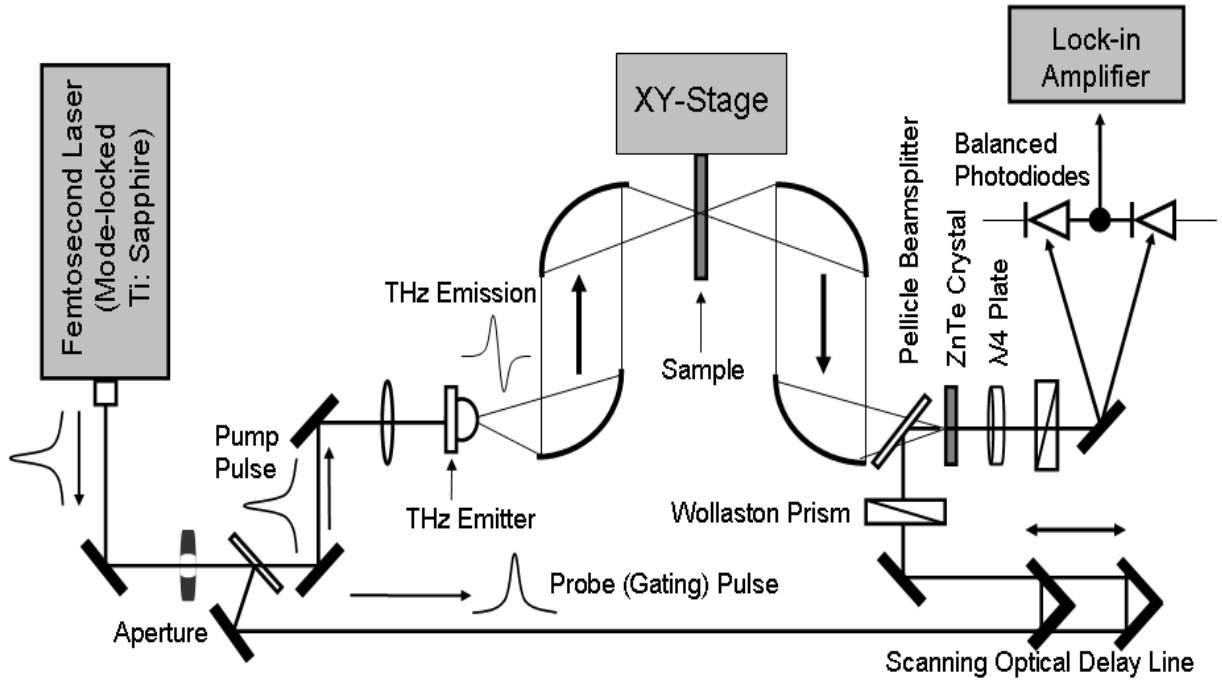


Figure 40. THz TDS Setup for Imaging Composites in Transmission Mode.

### 4.3 THz Beam Propagation and Modeling

This section shows the results of modeling a THz beam spatially as a Gaussian through our THz TDS system and the minimization of the spot size at the sample. The numerical results are presented for both the transmission and reflection configurations. Finally, actual THz spot size measurements are compared to the modeling predictions.

### 4.3.1 Spot Size Minimization

The first step in calculating the propagation of a THz beam through an optical system was to obtain the measured radius of curvature and spot size measurements at the output of the hemispherical lens from Ekspla, the THz emitter and detector manufacturer. These parameters are listed in Table 7 below. The Ekspla hemispherical lens is considered a collimating lens and the beam actually narrows initially as it propagates out of the lens before it spreads. Many of the hemispherical designs result in the spreading of the THz beam at a given angle, which can then be collimated by a parabolic mirror and then focused by a second parabolic mirror.

**Table 7. Ekspla measurements at the exit of the silicon hemispherical lens.**

Frequency (THz)	Radius of curvature (mm)	Spot size (mm)
1.0	-0.224	4.1641
2.0	-0.225	4.16395
3.0	-0.2256	4.1639

The transmission mode setup for this experiment requires a unique mirror focusing arrangement to achieve the diffraction-limited spot size at the sample. One has to ensure that the THz beam fills the entire second mirror, is minimized at the sample, does not expand beyond the diameter of any of the mirrors, and then is focused at the detector. A diagram showing the propagation of the THz beam through the optical system is shown in Figure 41. The final design is able to achieve the diffraction-limited spot size within a limited path length and with available equipment. A summary of the diffraction-limits and the calculated values for the optical design is in Table 8. The beam diameter at the focus (\*) at 0.5 THz was estimated by extrapolating the radius of curvature and spot size from the Ekspla data.

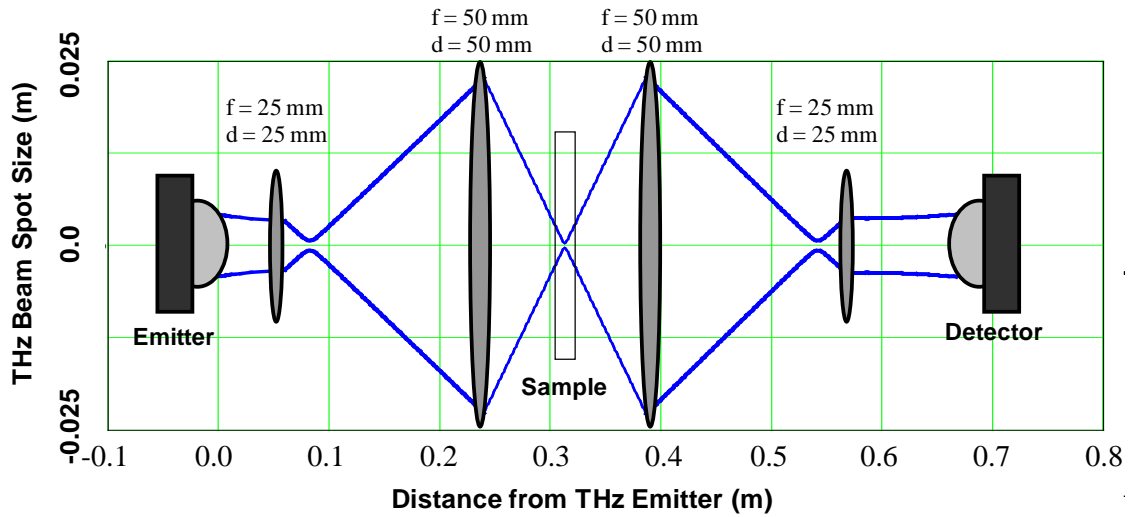


Figure 41. Diagram showing the transmission optical system with THz beam focusing on sample at 1 THz.

Table 8. Comparison of diffraction-limited spot sizes with THz beam optical design focus spot sizes for the transmission configuration.

Frequency (THz)	Diffraction-Limited Beam Diameter ( $\mu\text{m}$ )	THz Beam Diameter at Focus for Design ( $\mu\text{m}$ )
0.5	1200	1181*
1.0	600	617
2.0	300	312
3.0	200	209

A similar analysis can be performed to design the optical system for a THz TDS reflective configuration. The goal of that design is to minimize the spot size at the sample with available equipment within the shortest path length. Using the Ekspla data from Table 7, one can design an optical system in which five parabolic mirrors are used to steer the THz beam as shown in Figure 42. The maximum diameter of the THz beam at the third parabolic mirror is 31 mm, limiting the focusing ability of the system. The diffraction-limited spot size and the calculated Gaussian beam size at the sample are shown in Table 9.



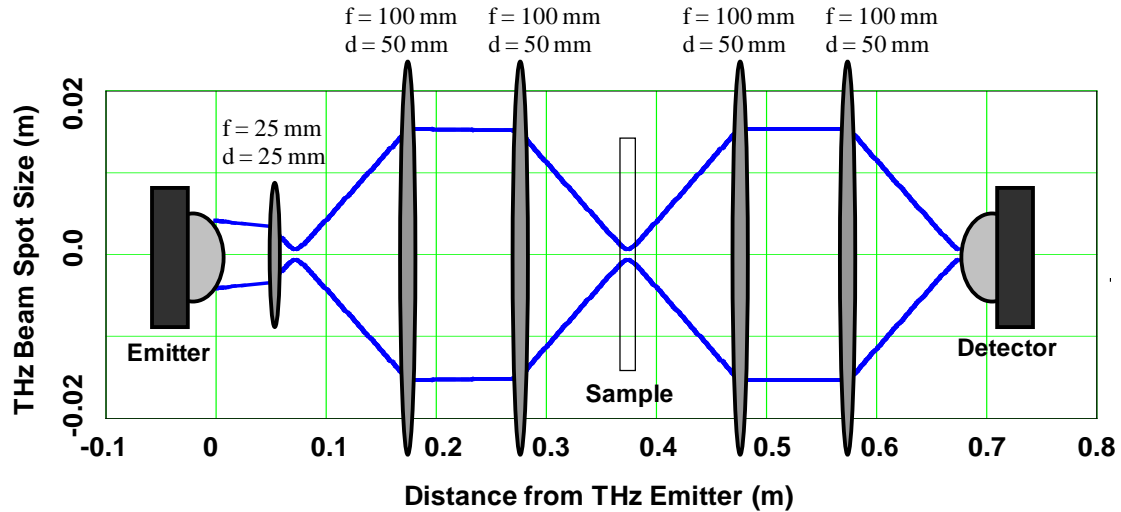


Figure 42. Diagram showing the reflection optical system with THz beam focusing on sample at 1 THz.

Table 9. Comparison of diffraction-limited spot sizes with THz beam optical design focus spot sizes for the reflection configuration.

Frequency (THz)	Diffraction-Limited Beam Diameter (mm)	THz Beam Diameter at Focus for Design (mm)
0.5	2.42	2.48*
1.0	1.21	1.27
2.0	0.60	0.69
3.0	0.40	0.52

### 4.3.2 THz Beam Measurements

The next task was to build and align the THz TDS setup similar to the numerical calculations, tweaking the parabolic mirrors and hemispherical mirrors to minimize the spot size. Although the final setup did not follow the model exactly, it provided a good starting point. The first setup that was measured for spot size at the sample was the transmission configuration. The first technique that was used was the knife edge method, scanning a knife blade through the THz beam horizontally and vertically. The knife was

scanned through the beam from 0% blockage to 100% blockage and beamwidth was measured between 88% of peak voltage and 12 % of peak voltage of an unobstructed beam with the electro optic detector [21]. The smallest beam measurements were 1.65 mm in the horizontal direction and 2.38 mm in the vertical direction, making it elliptical in nature. A circular hole of roughly 1.5 mm in diameter was then moved into the position of the minimum beam size. The result was that approximately 90% of the peak pulse voltage was transmitted through the hole.

Before imaging the composites in reflection configuration, the spot size was measured again. The same knife edge technique was attempted in reflection configuration, except that the knife was used to reflect the THz and not block it. In the horizontal direction, a spot width of 3.0 mm was obtained, while a spot width of 2.75 mm was obtained for the vertical direction. The positioning of the knife was more difficult in reflection setup so another method was attempted. This second method included the use of the circular hole with a piece of aluminum behind the hole. The geometry of this setup is shown in Figure 43 where  $\theta$  is the angle of incidence, X is the diameter of the incident THz beam, and Y is the spot size of the THz beam on the aluminum reflector. The method of calculating the spot size on the sample (Y) was to close the pupil and the measure the diameter at which 92% of the pulse peak was detected. The following equation was used to determine the spot size (Y):

$$Y = D - 2d \sin(\theta) \quad (85)$$

where  $d = 5$  mm. Given an incident angle of  $20^\circ$  and a measured pupil diameter of 7.2 mm, the spot size was calculated to be 3.78 mm. Since it was at an angle, the actual THz beam width would be around 3.55 mm.

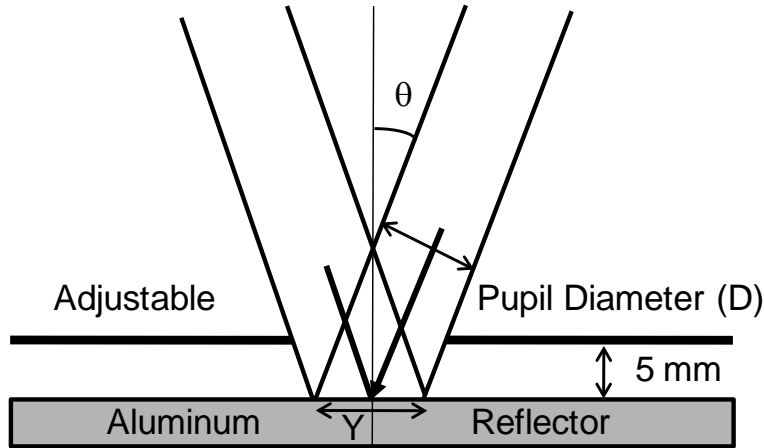


Figure 43. Diagram showing the geometry of the incident and reflected beam off the apparatus for measuring the THz spot size in TDS reflection configuration.

#### 4.4 Imaging of Composites with Transmission Setup

This section shows and explains the results for the first method of THz imaging using the TDS transmission setup shown in Figure 40 to obtain the images. Although this setup is not likely for maintenance operations, it provides insight into the capabilities and limitations of THz TDS imaging in general. In the first part of this section, there is a description of some of the results using thickness measurements and a comparison of some image processing techniques. The next portion of the section shows the results of THz TDS scans on various types of damage, including heat damage, bending damage, and hidden defects. Finally, the last section shows a measurement analysis of the depth of delaminations.

##### 4.4.1 THz TDS Thickness Measurements

One area of interest for imaging is whether the characteristics of the pulse change with different thicknesses and heat damaged areas of glass fiber material. Figure 44 shows how the THz pulse is not only reduced in amplitude through thicker samples, but

is also spread out in time as higher frequency components are attenuated more rapidly than lower ones. The arrival time of the pulse is also longer due to a longer optical path length through thicker materials. This illustrates how the THz TDS system could be used to measure sample thickness and hence a simple phase technique could be used to image composites for nondestructive evaluation.

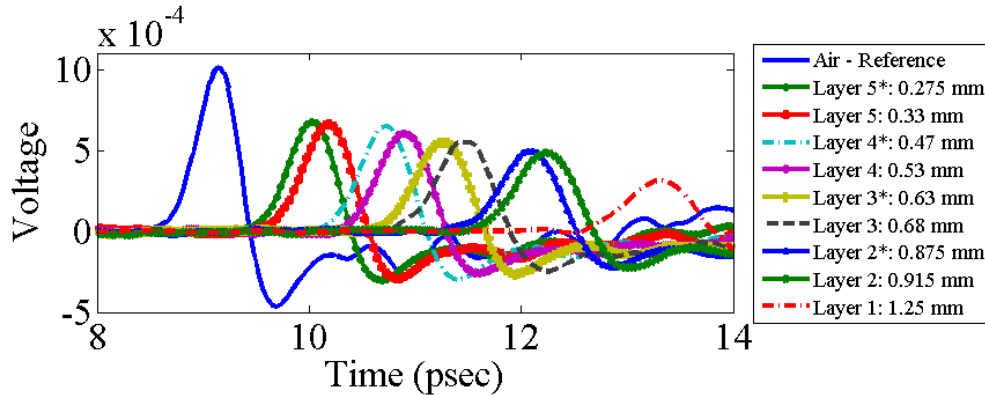


**Figure 44. Relative delay of THz pulses for various thicknesses of glass fiber sample, including those that were etched (\*).**

#### 4.4.2 Image Processing Comparison

The image processing technique that was described in section 2.4.6 was tested on a piece of glass fiber with a circle etched in it. The circle was 12.5 mm in diameter and approximately 70  $\mu\text{m}$  in depth. A series of images are shown in Figure 45, showing the progression of techniques from the original 1 X 1 mm pixel image in a. Figure 45c shows the image after zero-padding in the spatial frequency domain and Figure 45d shows the additional of the MATLAB ‘interp’ function to further smooth out the image in Figure 45c. Figure 45b was added to show the effect of the MATLAB ‘interp’ function without the frequency domain interpolation. The image in Figure 45e is the equivalent of viewing the original pixel image in (a) at 1/10 the original size.

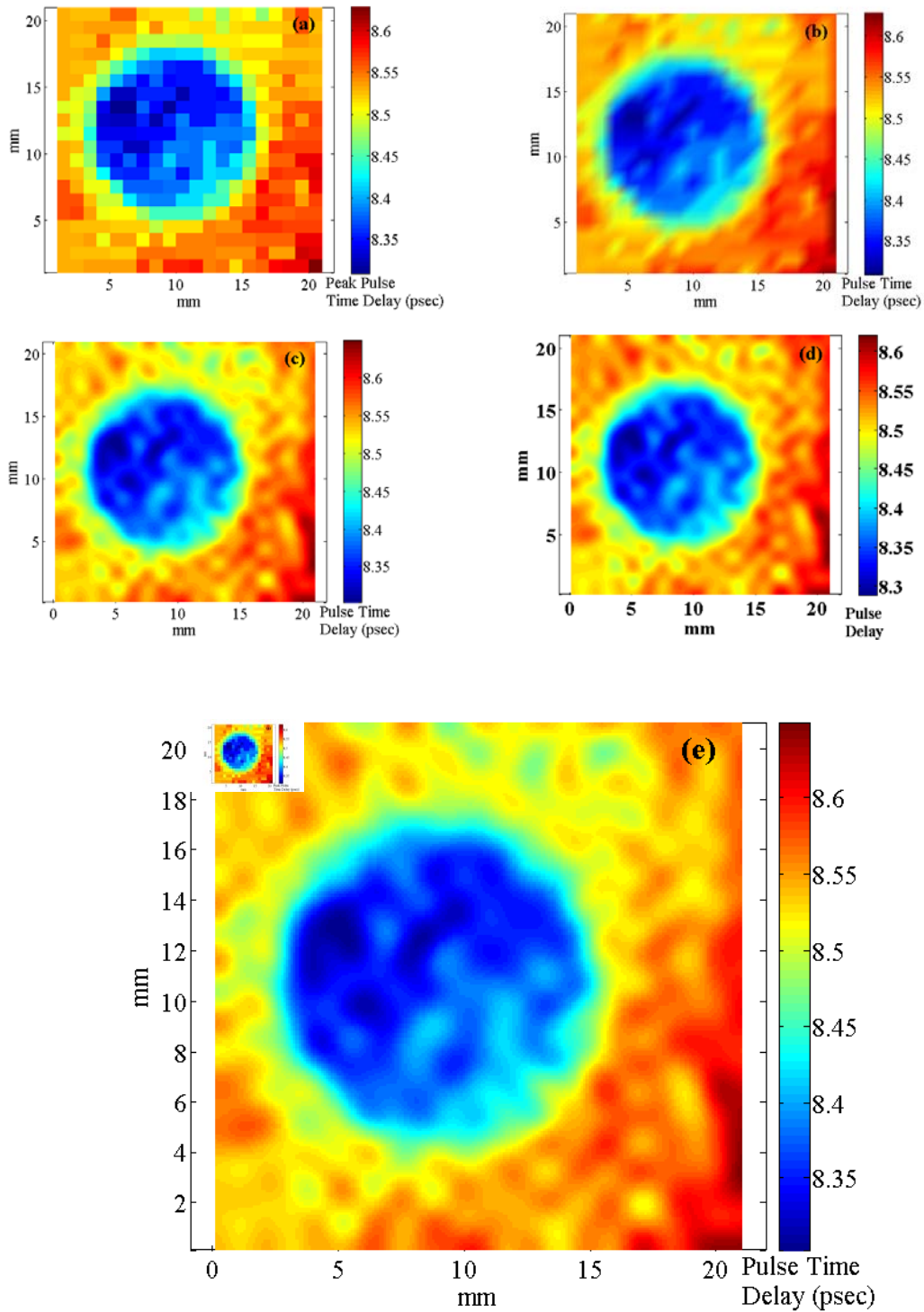
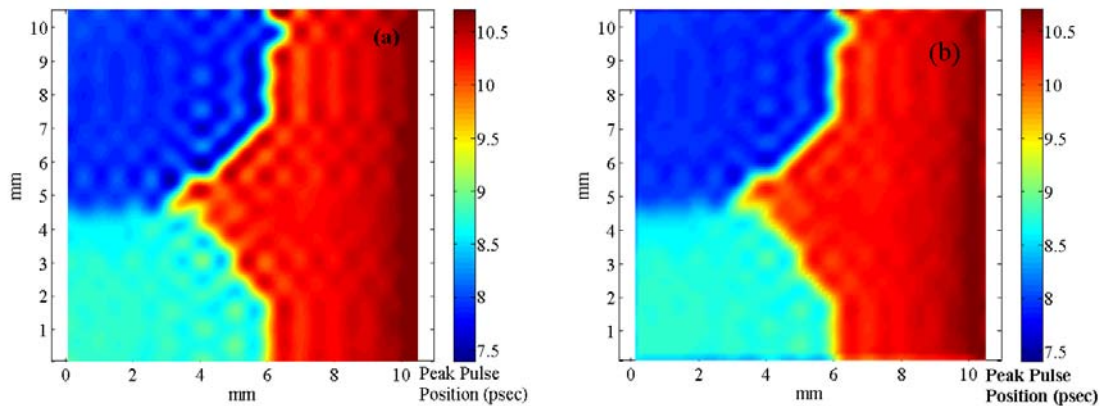


Figure 45. THz image of a 12.5 mm diameter circle etched in glass fiber showing (a) the original 1X1 mm pixel image, (b) image after MATLAB 'interp' function, (c) image after zero-padding 10 times in the spatial frequency domain, and (d) final image after applying MATLAB 'interp' function to part (c). (e) Comparison of (c) with 1/10<sup>th</sup> scale pixel image.

One of the consequences of using the zero-padding approach was that certain features, like sharp edges, caused a periodic modulation in the image. An example of this effect can be seen in Figure 46a. The “checker board” pattern could be reduced by zero-padding with fewer zeros and then using a Wiener filter on the image to reduce the modulation as is shown in Figure 46b.



**Figure 46. Image comparison showing the (a) the zero-padding technique (10 times) and the (b) zero-padding technique (4 times) with the addition of a Wiener filter.**

### 4.4.3 2-D Imaging Results

The first sample was prepared to calibrate the system based on material thickness. A THz image was taken of a 1 X 1 cm section of overlapping milled out areas with different thicknesses. The image is shown in Figure 47 where (a) represents the peak pulse amplitude and (b) shows the pulse position at each pixel of the sample shown in (c) [48]. The decrease in amplitude of the pulse at the edges is a result of THz scattering [48]. The periodic modulation in Figure 47b is a result of the interpolation technique to smooth out the pixels and does not match the pattern of the glass weave within the composite.

Similar images can be shown using the area under the curve from the amplitude spectrum in the frequency domain. The image in Figure 48 shows pixels that represent the sum of the amplitudes over the entire frequency spectrum that could penetrate the glass fiber composite. It closely resembles the peak pulse amplitude image shown in Figure 47a. The differing heights of the edges of the milled out areas causes a frequency

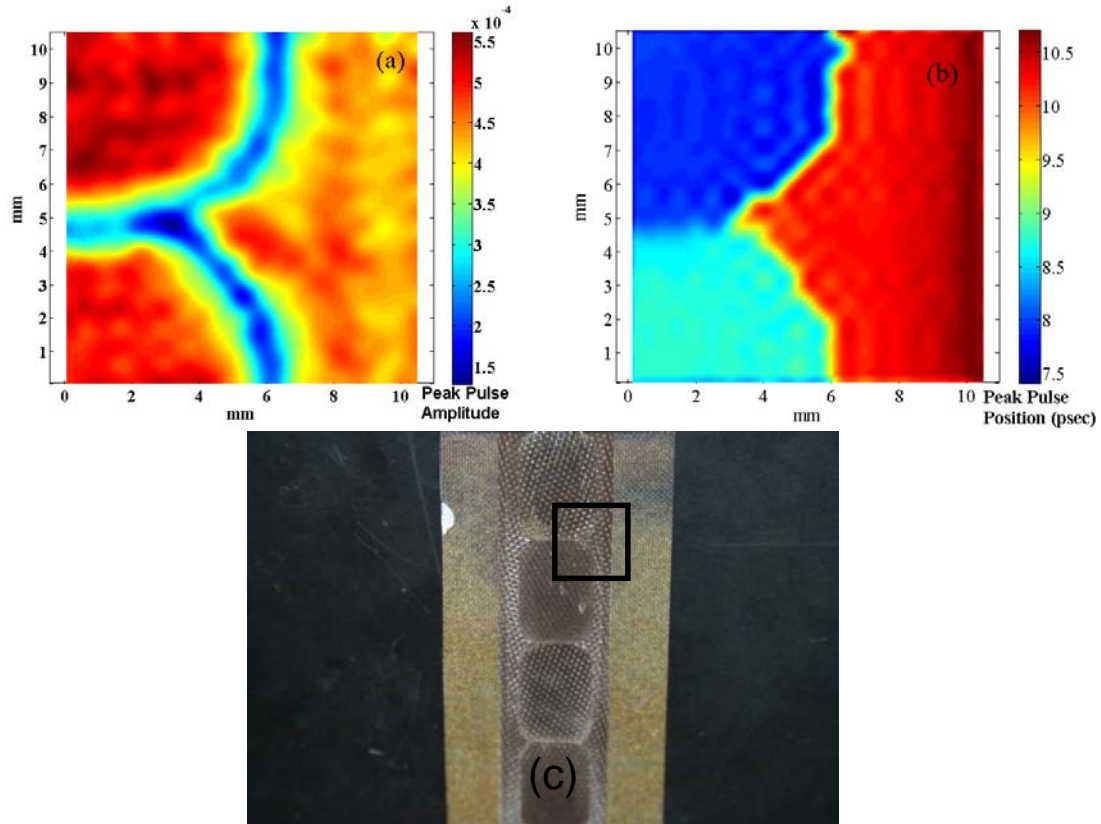


**Figure 47. THz TDS transmission images showing a section of the glass fiber that had been milled to two different thicknesses using peak pulse amplitude (a) and peak pulse position (b) techniques. A picture of the scan area on the calibration sample (c).**

dependence in the amplitude intensity. This can be seen in Figure 48 (b) and (c). The upper left quadrant is about 0.92 mm lower than the right half while the lower left quadrant is about 0.69 mm lower than the right half. The ridge between the two left quadrants has a height difference of 0.23 mm. The THz spot size is wavelength

dependent and was spread across the milled ridges differently depending on the position of the pixel during this raster scan. The lower amplitude areas represent the positioning of the THz spot so that a majority of the radiation at that frequency was scattered.

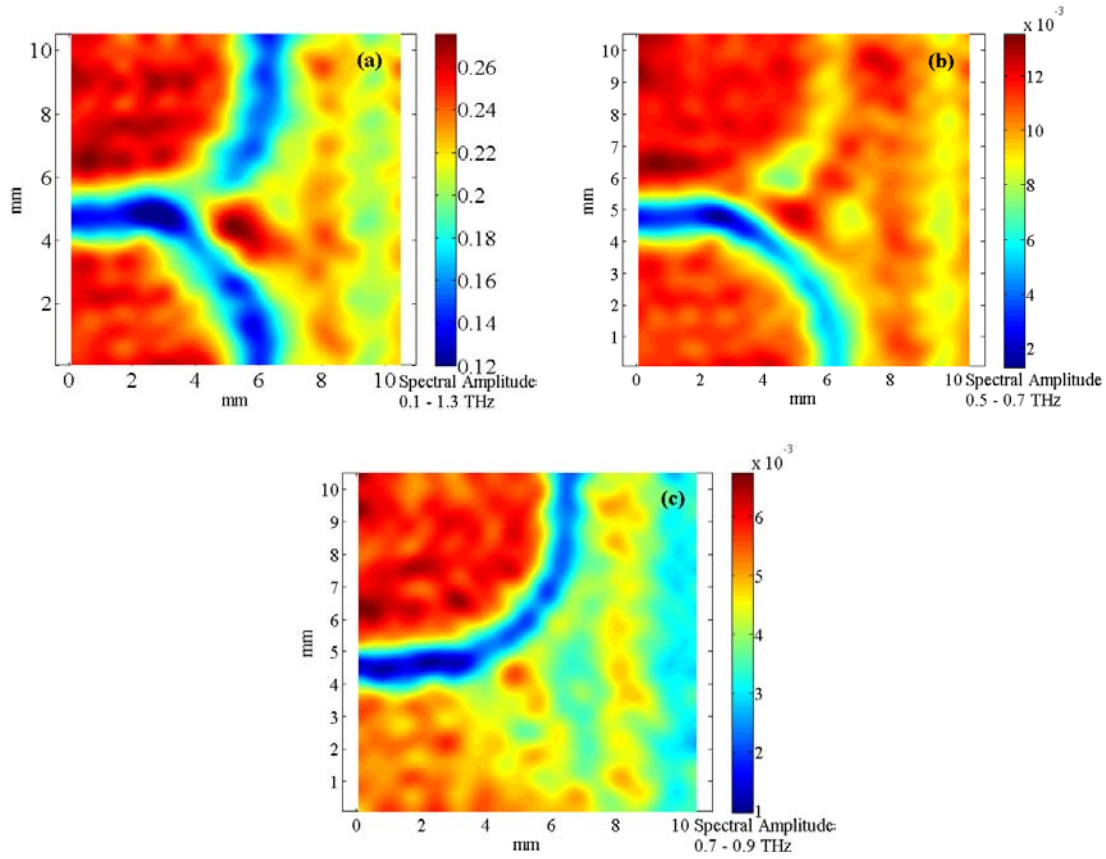


**Figure 48. THz images formed by summing the area under the curve of the amplitude spectrum within a given frequency range for each pixel: (a) 0.1 – 1.3 THz, (b) 0.5 – 0.7 THz, (c) 0.7 – 0.9 THz.**

#### 4.4.3.1 Imaging of Burn Damage

The next task was to image the burn samples. The results of the burn dot images formed by the peak amplitude of the THz pulses are shown in Figure 49 with the visibly burned areas within the circles. Figure 49a shows the sample that was burned at 440°C for 4 minutes over  $\sim 2 \times 1.5$  cm area. It has a visibly noticeable bubble or blister on its exterior which roughly corresponds with the blue area within the black oval.



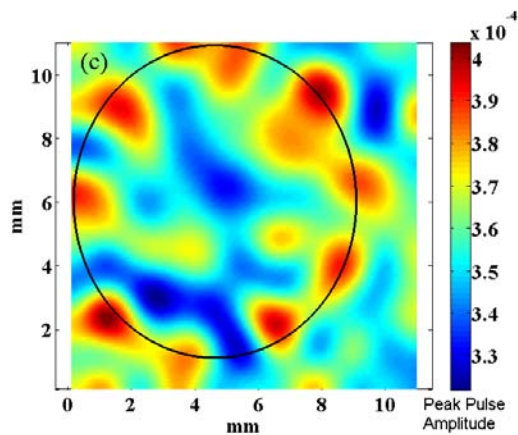
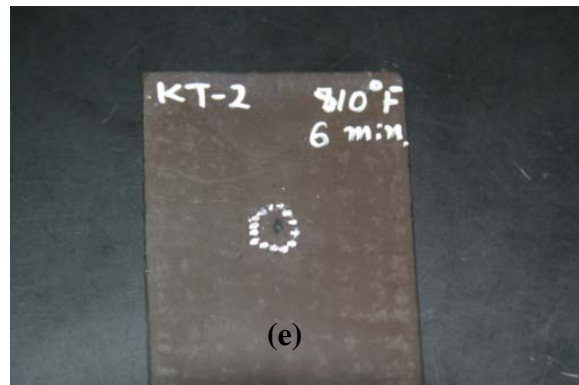
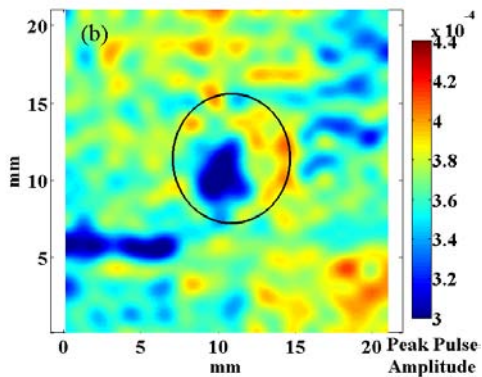
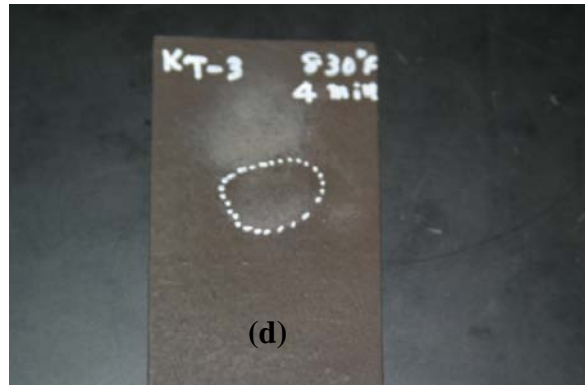
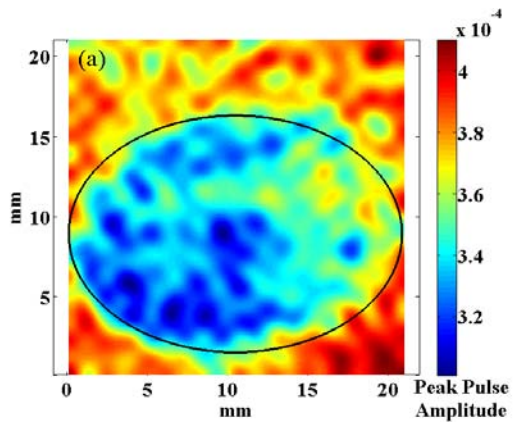


**Figure 49. THz TDS images and photos for three burn areas on glass fiber samples: (a), (d) 440°C for 4 minutes; (b), (e) 430°C for 6 minutes; and (c), (f) 425°C for 20 minutes.**

Comparisons of the THz time domain signal of pixels from the burn area were made with those from outside the burn area. A comparison is shown in Figure 50 contrasting a THz signal from an undamaged portion of the sample to one from the center of the large burn area (440°C for 4 minutes). There appeared to be time domain reflections in several of the pixels within the burn area, showing evidence of air gaps, but without a consistent pattern between pixels. These reflections caused a reduction in the peak pulse amplitude based on the Fabry-Perot etalon effect from the air – composite interfaces, which reduces the initial peak pulse, and because of scattering from the small air gaps and discontinuities. In the frequency domain, there were no consistent spectral changes to the THz signals through the burn areas.

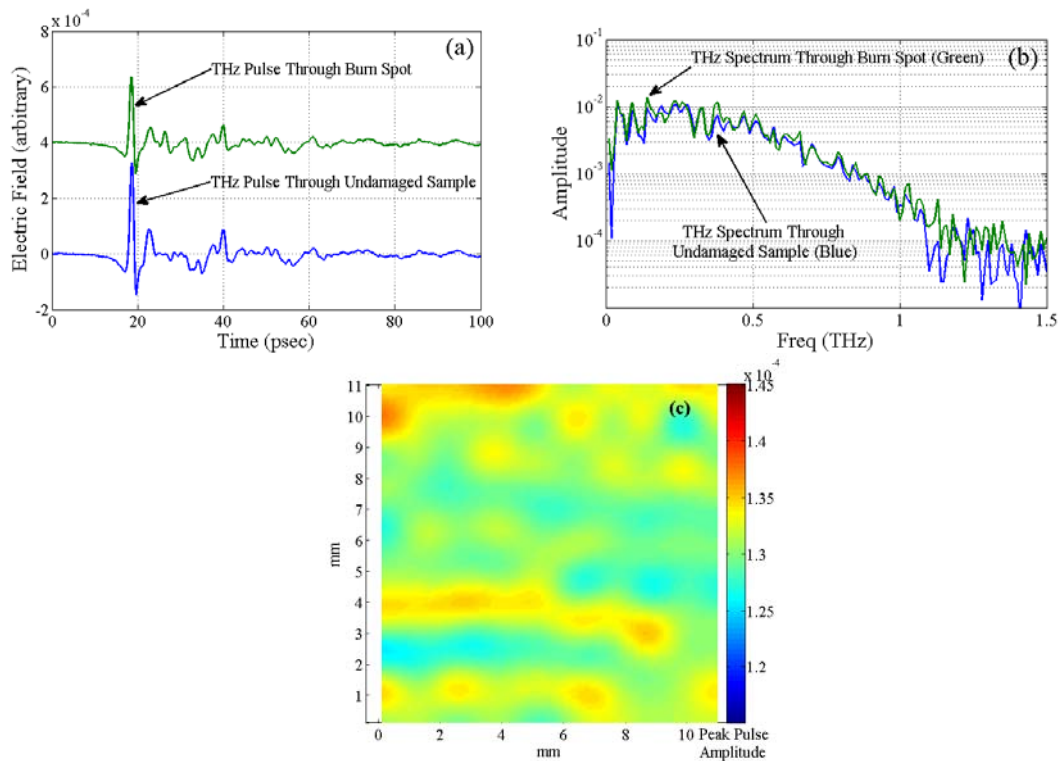


**Figure 50. THz TDS (a) pulse image and (b) amplitude spectra for undamaged glass fiber sample and for an area with burn damage (440°C for 4 minutes). (c) THz TDS amplitude image of high resistivity silicon.**

The other two burn areas are shown in Figure 49b and 49c, neither of which showed much visual evidence of blistering. The dark blue area within the circle in Figure 49b is roughly equivalent to the position of the residue or coating loss. Since the absorption spectrum remained higher than the unburned sample, even when adjusted to the same optical path length, it is more likely that the dark blue area is a form of residue. The red circular dots in Figure 49c and less noticeable orange dots in Figure 49b correspond to the white marker dots made on the samples to show the extent of the burn area. The THz image of the damage area in Figure 49c was inconclusive in showing evidence of burning.

During many of the transmission scans, the laser output power varied, and this variation was not stabilized until after the laser optics were cleaned. To demonstrate this variation, a scan was made of the thin wafer of high resistivity silicon. This scan can be seen in Figure 50c showing the approximate color variation for the pulse amplitudes that were demonstrated in 49c. The mean amplitude was measured at 1.306 mV while the standard deviation was 0.017 mV (1.33%) and the maximum variation was  $\pm 4\%$  from the mean. Over the same scan period, the laser power varied by 3%, roughly matching the pulse amplitude pattern shown in the image. If one considers that in Figure 49c that the amplitude varied by more than  $\pm 7\%$  across the image (not including the marker dots) then one could say that the signal-to-noise of the transmission setup contributed to the image variations, but was not the most significant factor.

#### 4.4.3.2 Imaging of Bending Damage

An attempt was made to show damage caused by mechanical fatigue as a result of 6240 bending cycles. Visually, one could observe a thin area of discoloration on one side of the glass fiber strip and one could see a small amount of cracking and buckling on the back side. In Figure 51, the image of the sample shows an area of lesser amplitude corresponding roughly to where the axis of bending occurred. Electrical tape, in the shape of an 'X', was attached at the top of the image area for reference as shown in the first photo in 51b. The second photo in 51c shows the location of cracking on buckling on the back side of the sample that corresponds to the pattern in the THz image. The

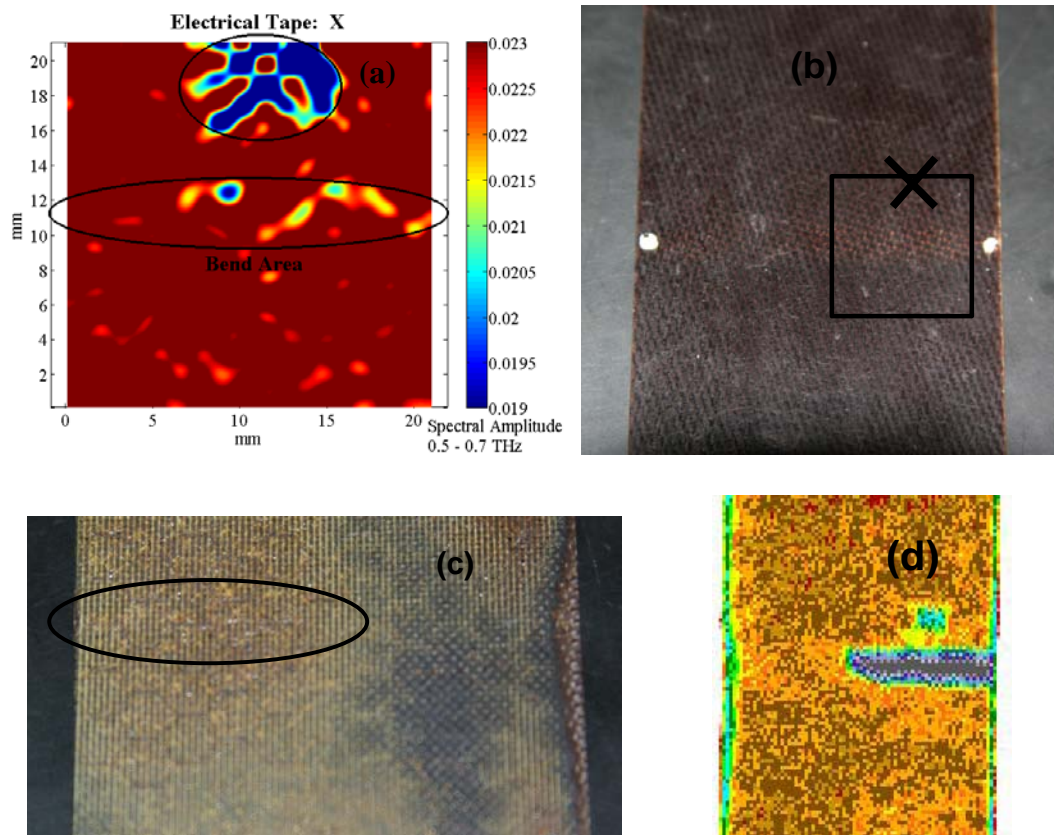


**Figure 51. THz TDS image showing bend damage across the central bend axis (a). Photographs of the (b) front side of the composite strip showing the scan area with the location of the taped 'X' and the (c) back side showing the location of the cracking and buckling and the hexagonal structure. (d) Ultrasound image of the bend damage.**

cracking and buckling follows the hexagonal pattern faintly visible in the picture.

Finally, the image in 51d shows an ultrasound image of the same damage, showing the same damage area and the electrical tape.

#### 4.4.3.3 Imaging of Hidden Defects

Voids were also investigated, which simulated either manufacturing defects or damage caused by stress over time. THz images are shown in Figure 52a and 52b for a circular void (3 X 3 mm) and a crack or slit void (6 mm length) in 52c. For the circular

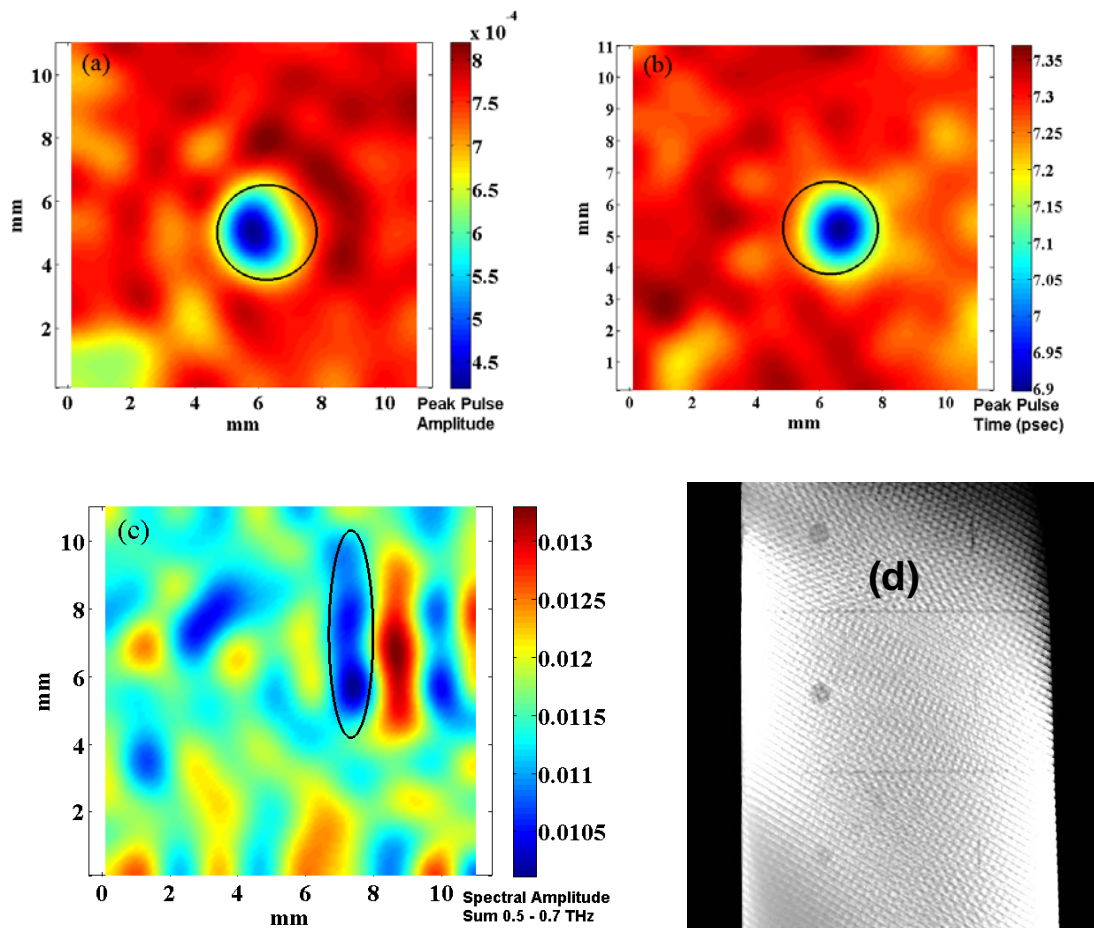


**Figure 52. THz TDS images showing 3 mm diameter milled area hidden between two glass fiber strips using (a) peak pulse amplitude and (b) peak pulse position. Linear slit void (6 mm length) (c) also hidden between two strips of glass fiber. The final picture is an x-ray computed tomography scan of the laminated sample showing the hidden circular and slit voids in the sample.**

void, a simple time domain amplitude or phase technique was sufficient to detect the void. For the slit void, a specific frequency range was required to isolate the approximate position, and was more difficult to isolate on multiple attempts [48]. The voids show an area of reduced amplitude, most likely due to the multiple reflections from the air/composite interface. A larger number of samples per area could be useful in isolating this slit void in space by providing more complete coverage at the higher frequency components. Another candidate would be to use a rotate the sample at  $45^\circ$  to the THz polarization and then collect pulses with the detector at horizontal polarization and then vertical polarization.

#### 4.4.4 Depth of Delamination Analysis

The previous experiments demonstrated the imaging of voids in a two-dimensional plane. An attempt was made to use THz TDS to isolate a void in the third dimension of depth using the time domain. The goal was to use THz TDS to find Fabry-Perot reflections in a delaminated area of the laminated sample (#5 in Figure 39) where the epoxy had not adhered the two glass fiber strips. The THz scans are shown in Figure 53a, showing the THz pulse after it had transmitted through the adhered area and the delaminated area. The autocorrelation was taken for each of the two pulses independently of each other in the attempt to show the Fabry-Perot reflections in Figure 53b. Then the sample was flipped over and the process was repeated in the opposite direction Figure 53c and 53d. The timing of the Fabry-Perot reflections was calculated with  $T_{FP-ref} = 2n_{gf}l/c$  where  $n_{gf}$  is the index of the glass fiber and  $l$  is the thickness of a delaminated piece. Given that the index of refraction is 2.05 and that the thickness of the

two layers is approximately 0.23 mm and 0.92 mm, the predicted times would be 3.12 psec and 12.5 psec. The first Fabry-Perot reflection occurred at approximately 3.3 psec after the main pulse in the autocorrelations. The approximate location of the second Fabry-Perot reflection is shown; however, the autocorrelation is difficult to identify on the graph. The Fabry-Perot reflections show up similarly in both directions, indicating the ambiguity in determination of depth using a transmissive setup.

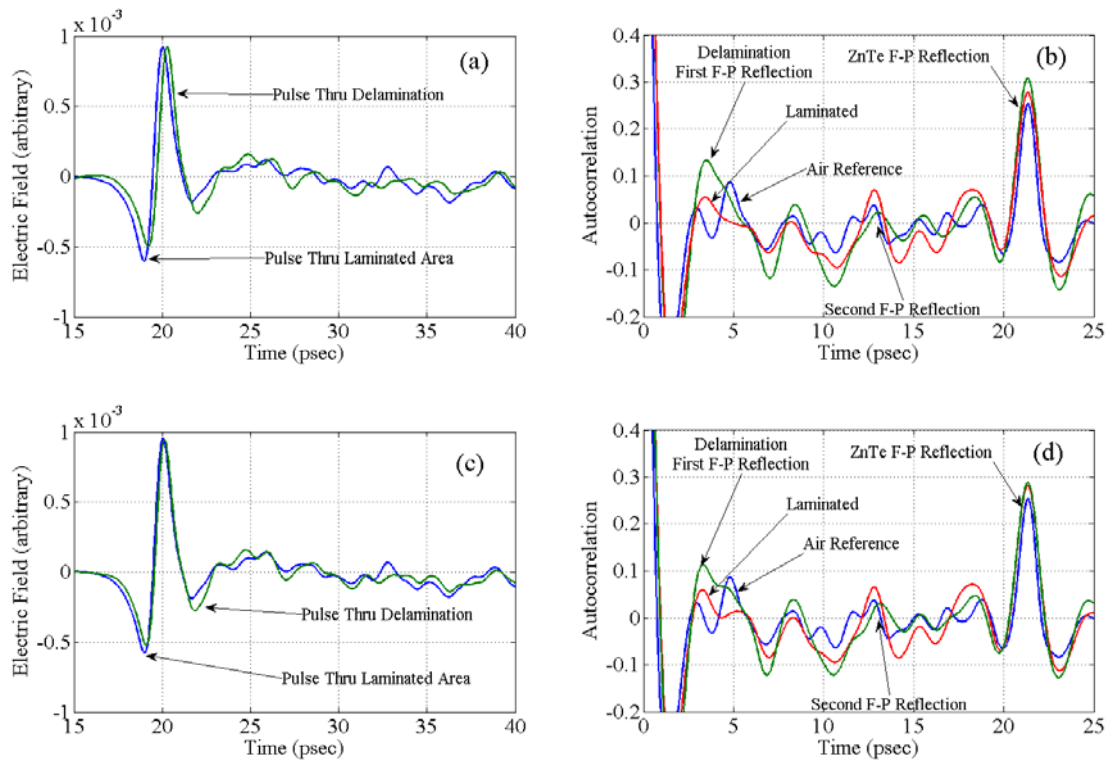


**Figure 53. THz pulses after propagating through (a) laminated and delaminated portions of a glass fiber strip. (b) Autocorrelation of each of the two pulses showing the approximate location of Fabry-Perot reflections. Thz pulse propagation in the opposite direction showing pulses and their autocorrelations (c), (d).**

The attenuation of the THz signal can be estimated based on the measured absorption coefficient of the glass fiber,  $T_{FP}(\omega) = R(\omega)\exp(-\alpha(\omega)l)$ , where  $R(\omega)$  is the reflection of the signal off of the two air-sample interfaces. The amount of terahertz

radiation, relative to the initial pulse, that is transmitted through the glass fiber composite after undergoing a single Fabry-Perot reflection is shown in Figure 54, with a diagram of the two pulses in 54a, calculations for  $T_{FP}(\omega)$  in 54b, and a picture of the 0.23 mm delamination in 54c. One can observe in the figure that unless a delamination is very thin ( $\sim 0.23$  mm) the reflection is unlikely to be recognizable above the system response.

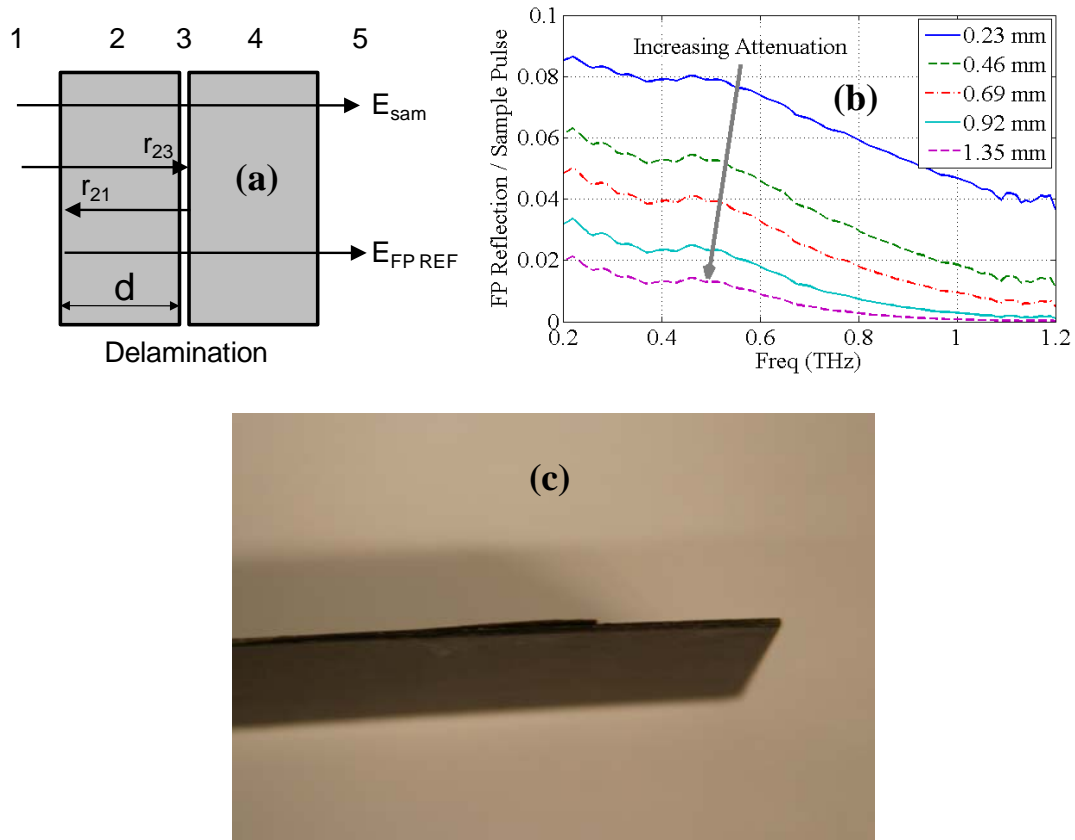


**Figure 54. (a) Diagram showing the main pulse and the first Fabry-Perot reflection in transmission configuration. (b) A chart showing the relative amplitude of the first Fabry-Perot reflection to the main pulse after traveling through various thicknesses of composite. (c) A photograph showing the delamination.**



## 4.5 Reflection Mode Imaging of Composites

This section shows the THz imaging results collected using the reflection setup shown in Figure 29. The reflection configuration is a more likely technique for maintenance than transmission. The samples were the same as those used for the transmission setup, providing a direct comparison of the two techniques. This section also looks at the same types of damage in two-dimensional imaging as well as a depth of delamination analysis. Finally, results are shown for reflection scans on entire exterior panels. All of the reflection mode images are taken with 1 X 1 mm step size in the raster scan.

### 4.5.1 Thickness Calibration

A comparison of the thickness calibration sample imaged with a reflection setup was compared to the transmission setup. The results of the peak pulse amplitude and peak pulse position images are shown in Figure 55a and 55b. The resolution of the images is not as good as the transmission images, but they still clearly show the three distinct areas. The scattering of the THz signal is also shown in dark blue in Figure 55a along the sharp edge between the different milled areas. The difference in amplitude in each area is based on the geometry of the THz optical system and not based on any characteristic of the glass fiber. The phase image in Figure 55b shows the opposite pattern of the pulse arrival from the images for transmission configuration. Thicker sections have a shorter arrival time in reflection, but a longer arrival time in transmission. An additional scan was made by lengthening the pixel scan time from 25 psec to 40 psec to ensure that the pulse reflected off the back side of the glass fiber was always collected.

From this data, a thickness image Figure 55c could be assembled using the optical path length of the THz in glass fiber.

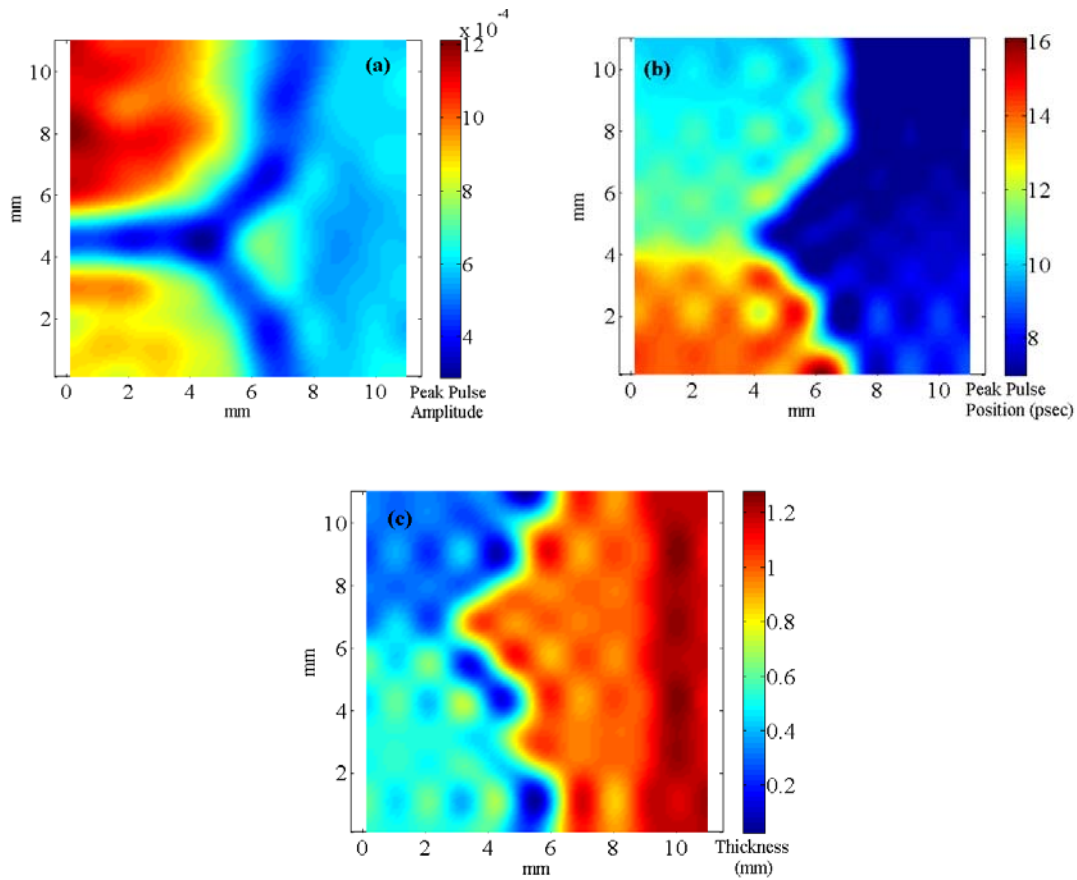


**Figure 55. THz TDS reflection images showing a section of the glass fiber that had been milled to two different thicknesses using peak pulse amplitude (a) and peak pulse position (b) techniques. The final image (c) shows a thickness estimation for a separate scan.**

#### 4.5.2 2-D Imaging Results

The following section shows the image results for the various types of damage. One of the issues that makes reflection mode imaging different from transmission setup is that the tip and tilt of the sample can vary as the sample is moved through the THz beam. This is caused by a slight angle misalignment ( $\pm 2^\circ$ ) of the sample to the raster scanning mechanism and/or a warping or curvature of the sample. This can create an artificial

delay of the pulse from top-to-bottom or from left-to-right. It can have the same effect on the amplitude due to a changing of the geometric alignment of the reflected beam through the collection optics. Linear correction techniques were implemented in post processing to attempt to correct these deficiencies. The bandwidth of the signal reflected from the surface was much greater than the bandwidth of any signal that penetrated the glass fiber at any depth.

#### **4.5.2.1 Imaging of Burn Damage**

The burn damage was imaged using the reflection configuration on the three areas analyzed earlier. The first burn area (440°C for 4 minutes), which had the most noticeable blister, was imaged first and the amplitude and phase images are shown in Figure 56. The rough area of the blister is encompassed by the oval. The amplitude image shows the sensitivity of the geometry of the sample within the TDS setup. One part of the bubble actually reflected more THz than the undamaged portion due to the initial alignment with the upper right corner of the image. The angular dependence of the reflection to the sample geometry causes a variation in the reflected amplitude due to a changing alignment of the THz beam within the THz optics. The phase plot shows a more accurate representation of the bubble where the true shape of the bubble is more apparent.

One can also observe the pulse shape characteristics in each of the pixels. For example, a pixel was chosen on the right side of the bubble and is shown in Figure 56c. One can see the double reflection off the bubble surface and off a hidden delamination below. The time of flight difference of 6.6 psec can be used to calculate the distance

between the pulses. Assuming an index of refraction of 2.05, the distance between the reflections was 483  $\mu\text{m}$ . The index is a rough estimate, because the bubble could contain some combination of air, coating, and glass fiber. However, if this estimate is close, then it would make sense that the delamination is close to where the original surface was located. An x-ray image of the sample, showing the bubble from the side profile, can be seen in Figure 56d.

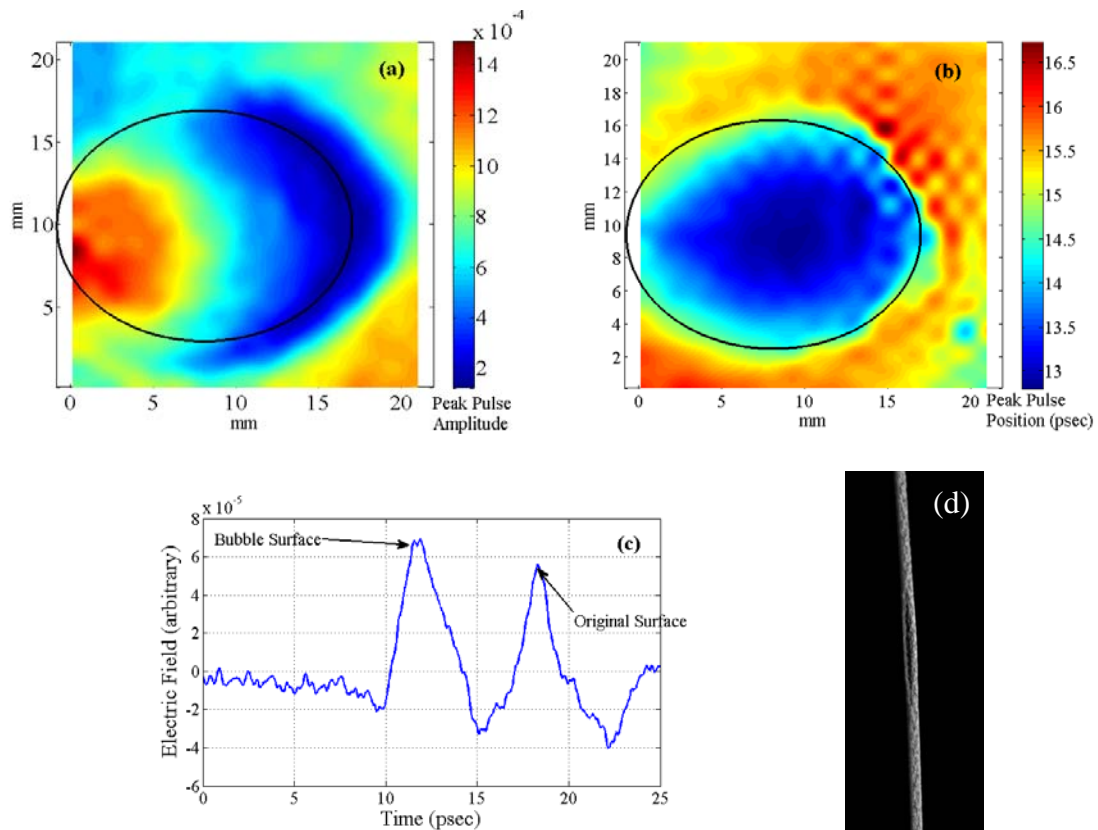


**Figure 56. THz TDS reflection images for burn damage from heating at 440°C for 4 minutes for (a) peak pulse amplitude and (b) peak pulse position. Pulse return from the right side of the bubble showing the double pulse return (c). X-ray computed tomography image showing a side profile of the large burn blister (d).**

Additionally, one can determine the approximate height of the bubble by measuring the difference in the pulse phase between the center of the burn area and the unburned area. From the diagram, one could choose a pulse position of 13 psec at the

center of the bubble and another of approximately 16 psec from outside the bubble for a difference of 3 psec. This equates to a height difference of 450  $\mu\text{m}$  which is the approximate thickness difference between the bubble (1.80 mm) and the undamaged glass fiber (1.35 mm).

The sample with the other two burn spots was imaged next. First, the area that had been heated at 430°C for 6 minutes was imaged and is shown in Figure 57a. Instead of using the peak pulse amplitude, the minimum pulse amplitude was used since it showed the residue coating better. This might have been due to the THz pulse reflecting off both the exterior paint and the surface of the glass fiber, which could have flipped the polarity of the pulse. The dot in the center of the circled burn spot corresponds with the residue. Next, the area that was heated at 425°C for 20 minutes was imaged with the reflection setup and is shown in Figure 57b. Like transmission mode, there was no hint of damage to the glass fiber, however, the white marker dots showed up again quite well. After adjusting the contrast, the apparent resolution of the dots is almost as precise as the transmission setup images.

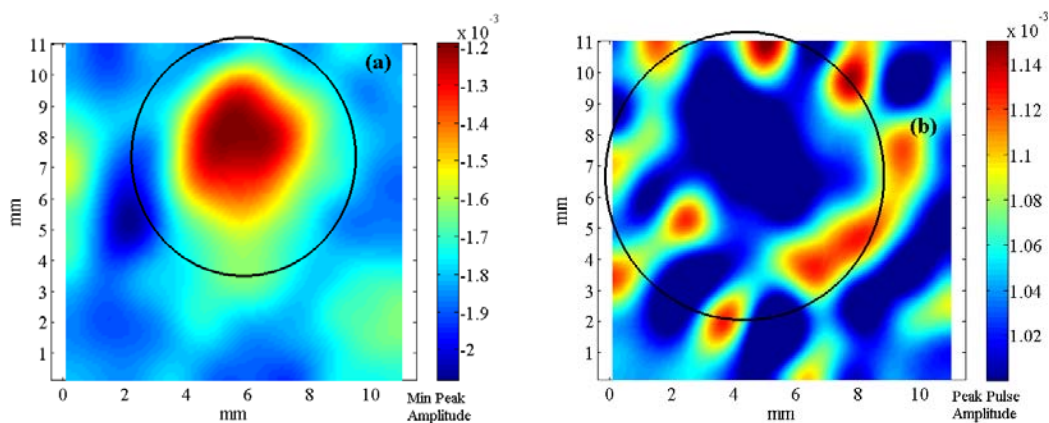


**Figure 57. THz TDS reflection images showing the (a) minimum peak amplitude for burning at 430°C for 6 minutes and the (b) peak pulse amplitude for burning at 425°C for 20 minutes.**

#### 4.5.2.2 Imaging of Bending Damage

Next, the sample having the mechanical damage caused by bending the glass fiber 6240 cycles was imaged in reflection setup. The image is shown in Figure 58. There is perhaps a slightly greater density of lower amplitude (1.2 – 1.4 THz) radiation around the bend axis, but it is difficult to categorize as conclusive. Further attempts were made to measure the thickness using a longer 40 psec scan time, but no additional detail was obtained.

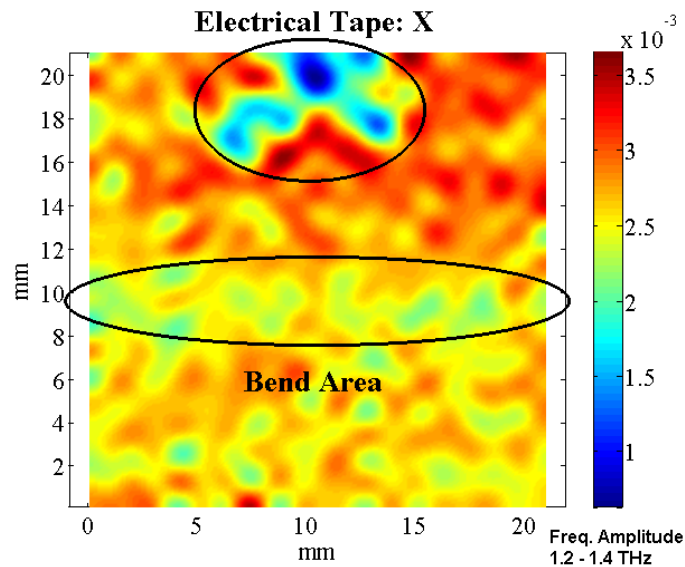
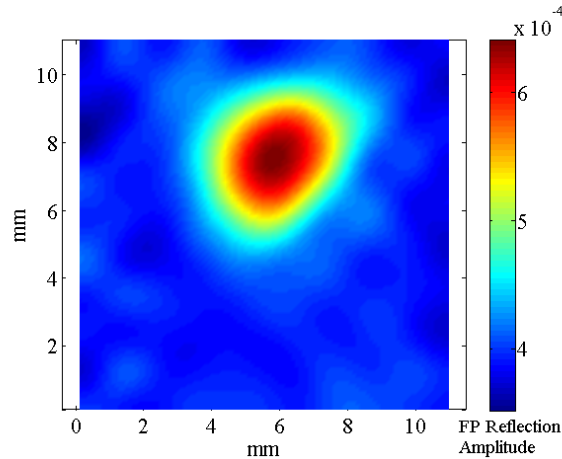


Figure 58. THz TDS reflection image using the amplitude of frequencies (1.2 – 1.4 THz) showing bend damage across the central bend axis.

#### 4.5.2.3 Imaging of Hidden Defects

The laminated glass fiber coupon with hidden defects was imaged next. The 3 mm diameter circular void was scanned first and shown in Figure 59. Since the void was hidden below the surface, a technique for imaging using the second THz pulse after the main pulse was used instead. This was in an effort to measure the first Fabry-Perot reflection located at the position of the adhesive and/or the air void. In this case the air

void had a larger index of refraction difference with the air than the glue, allowing it to appear in the image. Attempts were made to show an image of the linear slit void, but none of the techniques were successful in isolating its location.



**Figure 59. THz TDS reflection image showing 3 mm diameter milled area hidden between two glass fiber strips using the amplitude of the Fabry-Perot reflection from the void.**

#### 4.5.2.4 Imaging and Analysis of Entire Panels

Up to this point, all of the THz imaging has been on thin coupons of glass fiber with various forms of damage. On an aircraft, the glass fiber strips are attached to both sides of a much thicker honeycomb structure and attached to the external part of the aircraft. A THz TDS transmission scan was attempted on an entire panel (~3 cm thick), however, very little of the energy penetrated through. Obviously, TDS reflection mode would be required to detect damage in a panel. A couple of panels were prepared with burn damage, holes, and paint remover on their surface for imaging and analysis with THz radiation.

The first panel that was scanned had holes (4.5 mm diameter) punched through the glass fiber representing puncture damage and it also had burn damage between the

holes. The scanned area of the panel included one hole and two burn areas. A very noticeable burn area was on the right half. The other burn area was much less visibly noticeable; in fact, I didn't visibly notice it until it showed up on the THz TDS scan. Images of the panel can be seen in Figure 60, where the (a) minimum peak amplitude, (b) maximum peak position, and (c) amplitude spectrum (1.4 – 1.6 THz) are used to construct the images. Finally, a plot of the time domain pulse reflected from an undamaged, coated surface is compared to a pulse reflected from a partially uncoated, blistered portion of the panel in 60d.

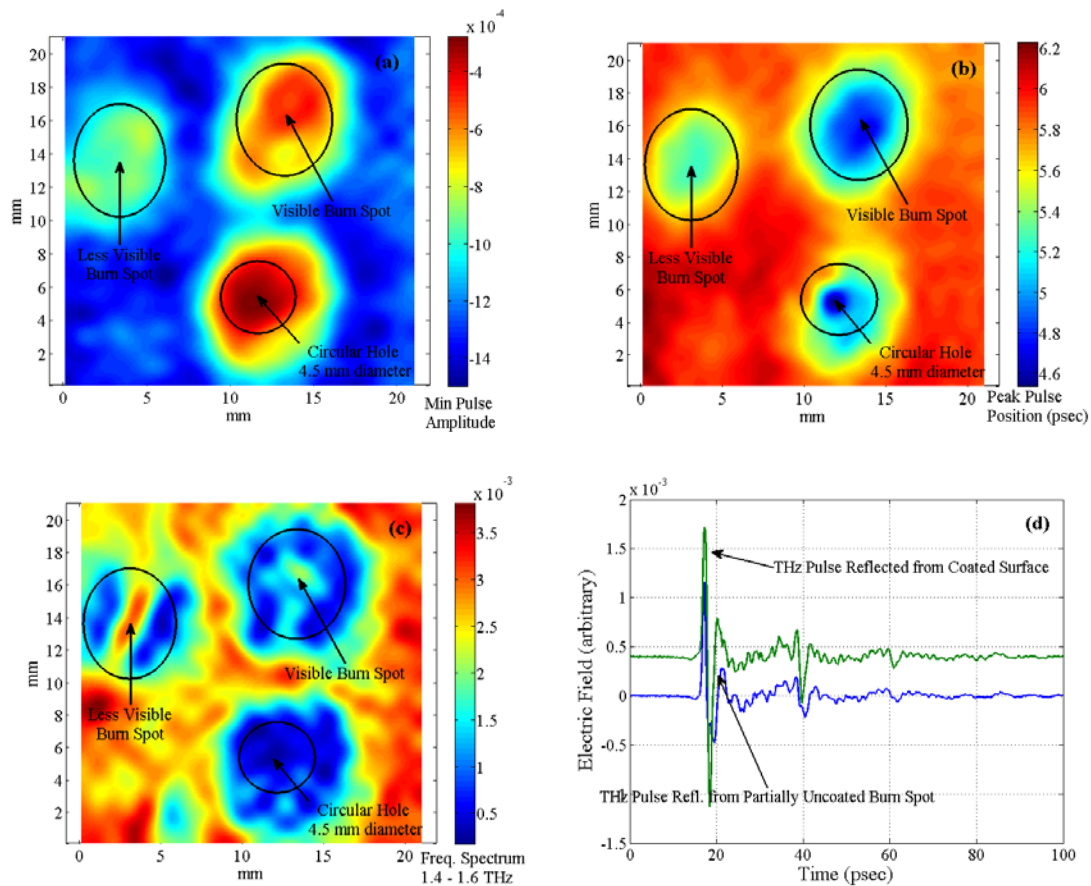


**Figure 60. THz TDS reflection setup scan on entire panel with puncture hole (4.5 mm diameter) and two burn blisters. Images were constructed using the (a) minimum peak pulse amplitude, (b) maximum peak pulse position, and (c) the frequency spectrum amplitude added under the curve (1.4 – 1.6 THz). THz pulses reflected from coated surface and partially uncoated burn blister (d).**



The next panel that was scanned had a solvent, called butanone, applied to the exterior surface of the panel to dissolve away the paint. The area that was dissolved was about 7 mm wide and can be seen on either of the images in Figure 61. One could also estimate the thickness of the paint that was dissolved away if the index of refraction for the paint coating was known.

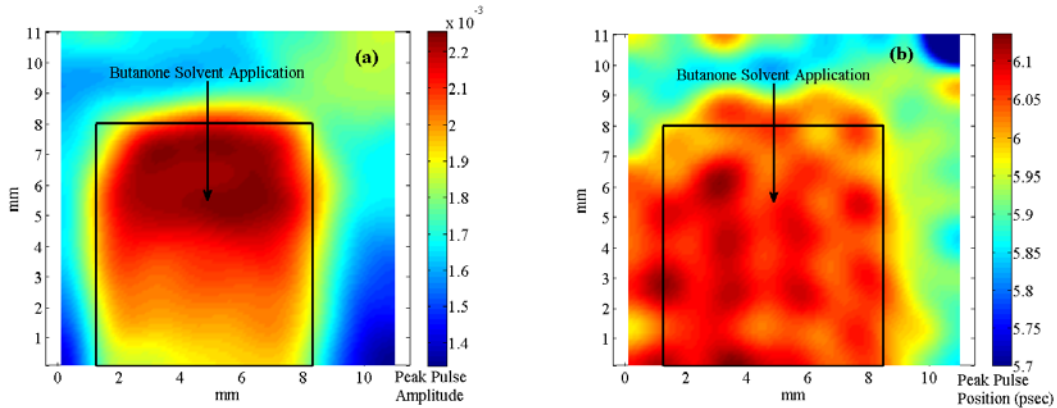


**Figure 61. THz images constructed using the (a) peak pulse amplitude and (b) peak pulse position of a panel with its coating dissolved away by butanone.**

The two past panels show that THz TDS setup in reflection mode is capable of imaging changes to the exterior of glass fiber on a panel. For this research there were no samples available with known, hidden defects, but one could assume that hidden defects would reflect THz energy in the same way that the thin glass fiber coupons would. However, another important question was how the honeycomb structure under the glass fiber reflects the THz signal. Long, time duration scans were taken of an entire panel to see whether there were any reflections within the honeycomb. A typical plot of the first half of a long scan is shown in Figure 62a where the time domain reflections off of a coated and uncoated glass fiber surface are shown. Apart from the ZnTe etalon effect, there is nothing remarkable about the pulse characteristics even when it was extended to

200 psec. Apparently, the honeycomb either traps the energy or it gets attenuated sufficiently so that it is not detected. There is also no back reflection off of the back side of the glass fiber, indicating a smooth transition from the glass fiber to the honeycomb. A graph of the corresponding frequency spectra are shown in Figure 62b.

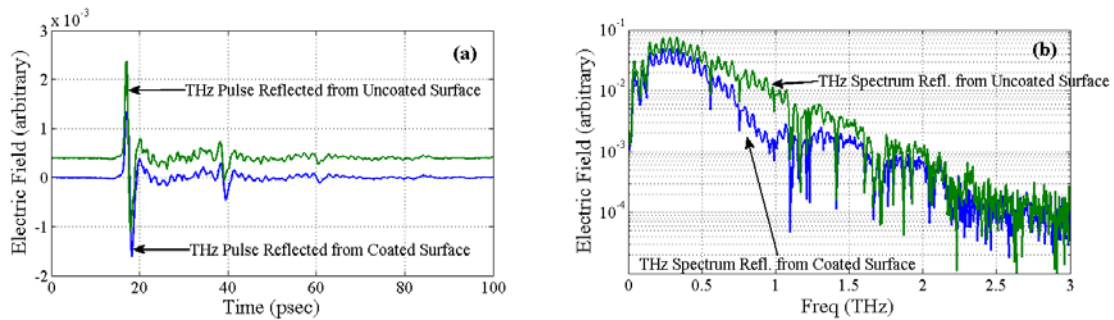


**Figure 62. THz TDS (a) time domain plots and (b) frequency spectra for a coated and uncoated surface of an aircraft panel.**

#### 4.5.2.5 Paint Thickness Approximations

An observation that was noticed was that the coating on the glass fiber caused a double reflection of the THz pulse on the front surface. A time domain plot of this can be seen in Figure 63a where there is a double peak in the positive polarity of the pulse. It is also apparent that the back reflection of the coated glass fiber sample is non-existent, making any attempt to measure the material properties with the back pulse to be impossible. A plot of the THz frequency spectrum is shown in 63b, where the spectrum shows a fast roll-off after 0.4 THz and 1.6 THz due to the Fabry-Perot effect with the paint. One could use the time domain plot to determine the thickness of the coating given the index of refraction of the coating or vice versa. Since the index of refraction for the coating was estimated to be around 2.05, the thickness of the coating on the glass fiber samples was 55  $\mu\text{m}$ .

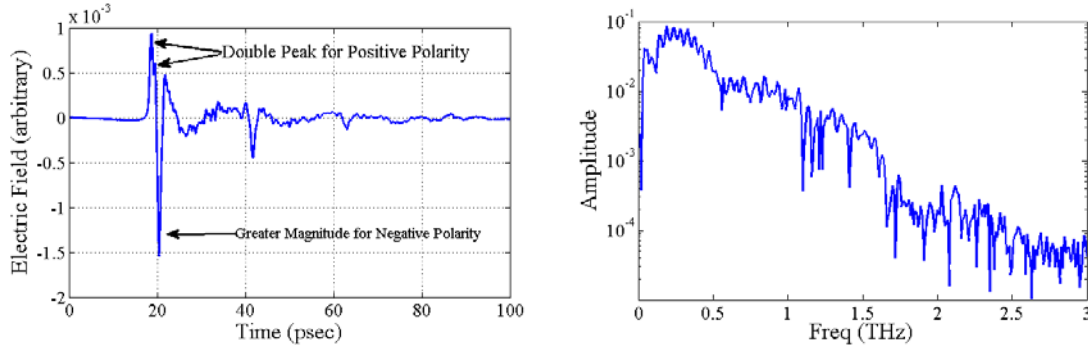


**Figure 63. THz TDS reflection configuration plots showing the (a) time domain pulse with a double peak and the (b) THz amplitude spectrum.**

### 4.5.3 Depth of Delaminations Analysis

Similar to the transmission configuration, an analysis was performed on data collected on the depth of delaminations for reflection configuration. During the data collections it was quickly apparent that the adhesive – glass fiber interface provided a large enough index discontinuity to create a back reflection. The air – glass fiber interface was even better for reflections because the greater  $\Delta n$  resulted in a higher reflection coefficient. A diagram of the reflection configuration is shown again in Figure 64a. To show the relative strength of the first Fabry-Perot etalon reflection to the surface reflection, we used the following equation:

$$\frac{E_{FP\_Ref}}{E_{sam}} = \frac{t_{12}(\theta_1)t_{21}(\theta_1)r_{23}(\theta_1)}{r_{12}(\theta_1)} \exp\left(-\frac{\alpha(\omega)}{2}(2d)\right) \quad (86)$$

where the Fresnel coefficients were shown previously in Equations 83 and 84. The graph in Figure 64b shows the relative strength of the first Fabry-Perot reflection at various depths off of an air - glass fiber discontinuity to the strength of the front pulse. A similar chart is shown for a glue – glass fiber interface in Figure 64c, including an air gap delamination at 0.93 mm and the back side interface at 1.25 mm. These relative

amplitudes of the Fabry-Perot reflections compared favorably with the amplitudes of the measured data from the laminate sample.

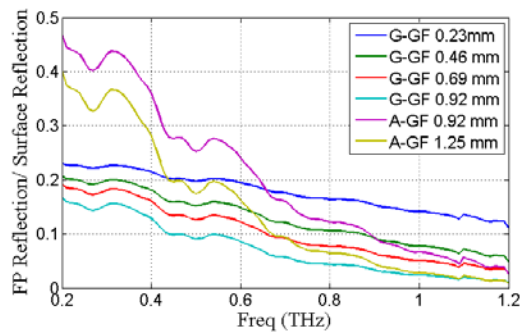
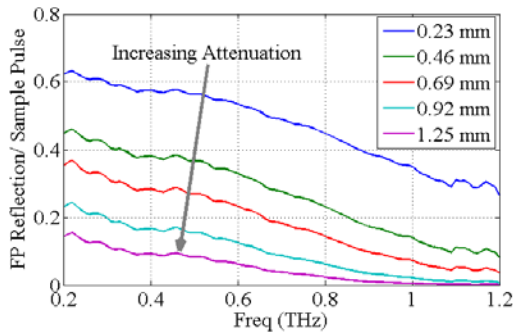
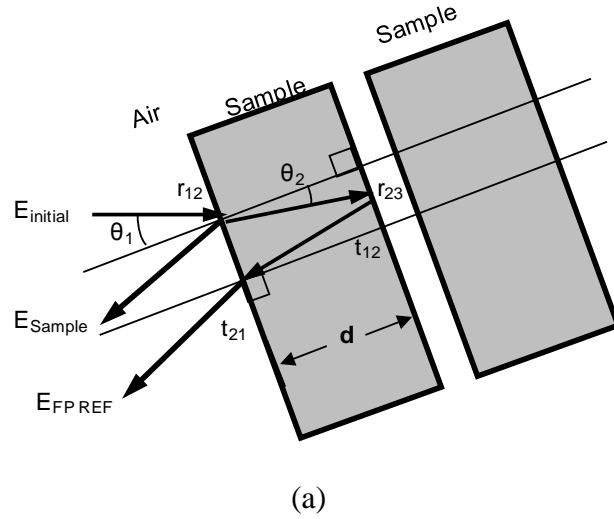


**Figure 64. (a) Diagram of a delaminated sample showing the first Fabry-Perot reflection in reflection configuration. (b) A chart showing the relative strength of the first Fabry-Perot reflection after traveling through various thicknesses of glass fiber composite before the delamination. (c) A chart showing the relative strength of the first Fabry-Perot reflection from discontinuities including both glue-glass fiber (G-GF) and air-glass fiber (A-GF).**

The next step was to analyze data that was collected at the various depths.

Examples of TDS time domain scans in reflection mode are shown in Figure 65. The scan in 65a shows the very distinct reflections that occur when the THz pulse reflects

from the delaminated air-glass fiber interface and also the back air – glass fiber interface. The scan in 65b shows an example of a Fabry-Perot reflection from a glue – glass fiber interface. Both discontinuities were located at 0.23 mm below the sample surface and the back side reflection can also be seen in both.

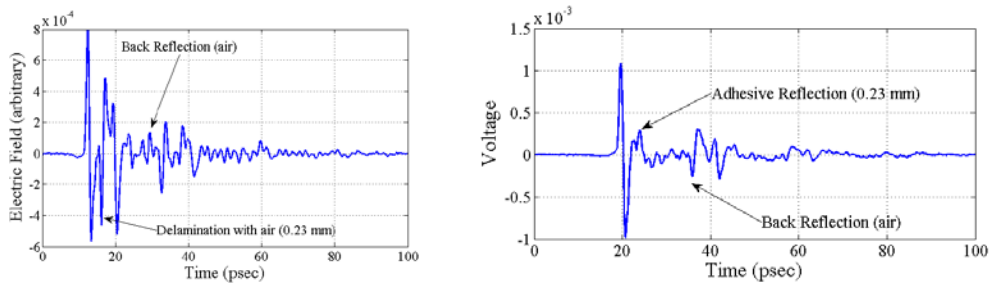


**Figure 65. THz TDS time domain plots showing reflections from discontinuities: (a) air and (b) adhesive.**

The technique that was used for depth determination was to use a Fourier deconvolution  $D(t)$  in the time domain instead of the autocorrelation used for transmission mode. This is demonstrated in the following equation:

$$D(t) = \left| \text{ifft} \left| \text{fft} (E(t)) \right| \right| \quad (87)$$

in which  $\text{fft}$  is the fast Fourier transform and  $\text{ifft}$  is the inverse fast Fourier transform. A comparison of the returns from discontinuities at various depths is shown in Figure 66 a-f. The dashed lines were added to show the similarity of the backside reflections in each scan along with the pulse reflection from the ZnTe etalon effect. A separate calculation was made to remove the TDS system effects from the deconvolution. This was accomplished by making a separate measurement of the THz pulse reflection from aluminum and then subtracting out the aluminum from the sample. This removed most of the main pulse and the ZnTe reflection. A series of depth measurements can be seen in Figure 66 g-l for the various thicknesses. Each series of plots was measured from a

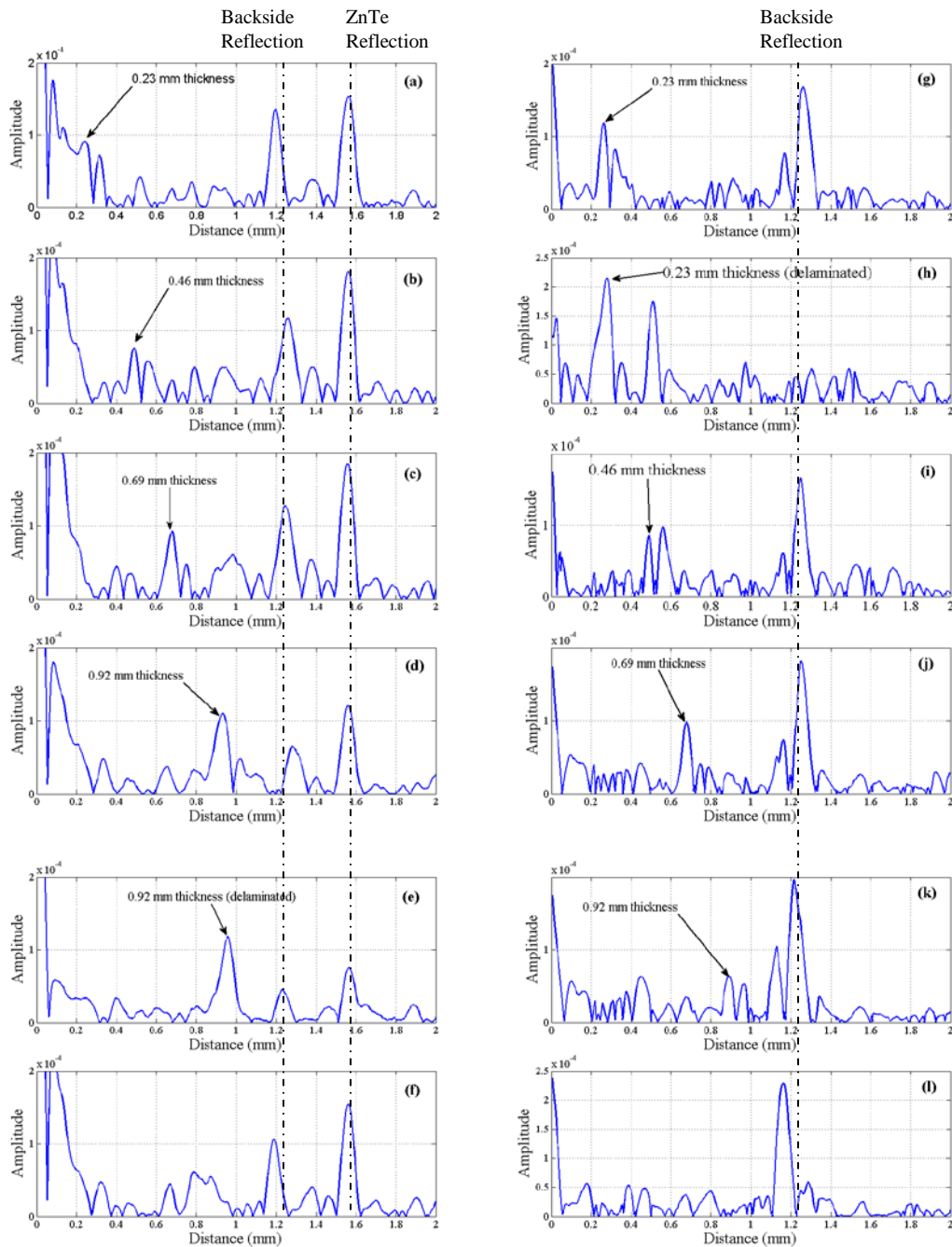


**Figure 66. Fourier deconvolution of the discontinuities present in a glass fiber sample laminated at various thicknesses: (a) 0.23 mm, (b) 0.46 mm, (c) 0.69 mm, (d) 0.92 mm, (e) 0.92 mm delaminated, and (f) no lamination. Fourier deconvolution with the TDS system characteristics subtracted are shown next. The various thicknesses were measured in the opposite direction: (g) 0.23 mm, (h) 0.23 mm delaminated, (i) 0.46 mm, (j) 0.69 mm, (k) 0.92 mm, and (l) no lamination.**

different side of the sample, showing minimal difference from each side. A plot of the calculated times and the autocorrelation times for the depth of delaminations measured with transmission and reflection configuration is shown in Figure 67. The measured autocorrelation time for transmission configuration is questionable beyond a depth of 0.23 mm. Both of the techniques are capable of imaging defects on the order of magnitude of a THz wavelength. A comparison of THz images between transmission and reflection configuration is shown in Figure 67.

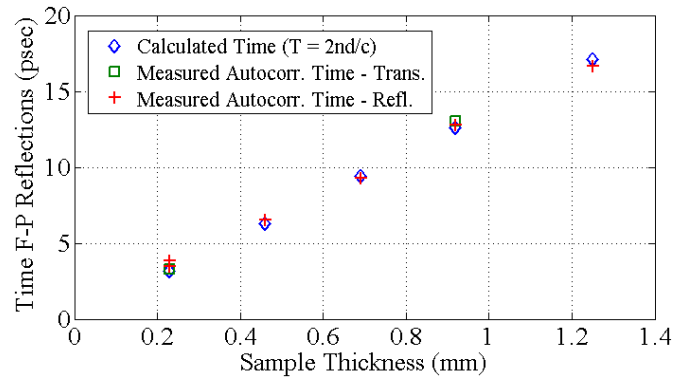


**Figure 67. Comparison of the calculated time for F-P reflections through glass fiber to the measured autocorrelation values measured in both transmission and reflection configuration.**

## 5. Conclusions and Recommendations

This chapter provides a summary of the research that was presented in the previous chapters followed by directions for future research. It explains how THz TDS has the potential to be a superior NDE technique for glass fiber composites over other NDE techniques. It then compares and contrasts the advantages and disadvantages of the TDS transmission or reflection setup. Finally, it provides recommendations for follow-on research projects.

### 5.1 Major Research Contributions

This research was novel in a variety of different aspects. First, it is one of the first research efforts that uses THz TDS as an NDE technique to inspect glass fiber aircraft composite samples with representative forms of damage. Second, it demonstrates how to use THz TDS to measure the material properties of a burn damage area on a composite in an effort to determine if the material has been chemically altered. Third, it shows how various types of surface and subsurface defects can be imaged and detected by either a transmissive or reflective TDS configuration. Fourth, it also provides an analysis on how effective each configuration would be at isolating the depth of discontinuities within the composite. Finally, it also presents a technique for measuring material parameters in reflection mode.

### 5.2 Conclusions

THz TDS has several potential advantages over other nondestructive evaluation methods for inspection of aircraft glass fiber composites. Both ultrasound and eddy



current techniques require that the source and detector remain in contact with the aircraft. In addition, eddy current testing requires that the material is conductive, which is not applicable to glass fiber. X-ray techniques use ionizing radiation to penetrate the sample which can cause safety issues for operators. X-rays can also require the use of penetrates to help detect delaminations. Video inspection can be time consuming and prone to human error. Microwaves have the ability to penetrate composites, but their resolution is more limited due to their longer wavelengths. Infrared techniques can have better resolution, but less penetration depth. THz can penetrate glass fiber without contacting it, with submillimeter transverse resolution, and can detect surface defects, hidden voids, delaminations, and bending damage in composites. The depth resolution for defects is potentially much better than the transverse resolution, and thin composite samples can be analyzed with THz TDS. Additionally, it can also be used to evaluate whether the aircraft composite has been chemically altered from engine burn damage by measurement of its index of refraction and absorption coefficient spectrum.

Material parameter measurements were made with both transmission setup and reflection setup. The dielectric properties of low resistivity silicon wafers were modeled with the Drude model and showed a close comparison with measured results. Fabry-Perot etalon removal techniques were moderately effective in removing the oscillations from the index of refraction and absorption spectra. It was more difficult to measure material parameters with reflection configuration because the technique of comparing the sample pulse to a reference pulse did not provide accurate results. For thicker samples, a time domain separation of the front and back reflections provides a useful technique, if

one assumes a flat refractive index response. It becomes more difficult when the samples are thinner and their absorption coefficients are higher.

Effective medium approximations were used to estimate the refractive index and absorption coefficient spectrum of the glass weave after measuring the polyimide and glass fiber composite separately. These indices of refraction were then used to calculate the scattering properties of the composite and estimates of the scattering coefficient were low for the THz spectrum due to the similarity of the indices of refraction for the two composite materials and the density of inclusions.

An aircraft glass fiber composite with various forms of damage was examined using both a transmissive and a reflective THz TDS system for NDE. Indices of refraction and absorption coefficients in the terahertz frequency range were measured using THz TDS in transmission configuration for comparison of damaged and undamaged material states. Results showed that localized heat damage did not change the material properties of the composite sample noticeably; however, changes in the terahertz signal were observed due to material blistering and/or residue deposited. The approximate depth of a delaminations could be determined in the time domain by measuring the timing of a Fabry-Perot reflection through a thin slice of the composite. Reflection configuration was much more effective in showing discontinuities, even between an adhesive layer and the glass fiber. A hidden circular void was imaged and there was also evidence that areas of damage from mechanical bending stress and simulated hidden cracks could be detected with terahertz TDS imaging in both configurations.

THz TDS in transmission setup was effective in locating voids at any depth or thickness, but had difficulty in finding damage that was smaller than THz wavelengths. Burn spots could be detected, but the dielectric properties of polyimide appeared to remain unaltered at burn temperatures below 480°C. Additional burn tests at temperatures approaching 480°C would have to be attempted to see if and when the material properties of the composite would change. A THz TDS system in reflection mode would be a more likely candidate for inspection of glass fiber composites on aircraft and would likely be more effective in determining the depth of damage areas. The glass fiber composite absorbs a significant amount of the THz radiation, attenuating a transmission signal, and limiting the use of Fabry-Perot reflections for depth measurements. In reflection mode, the magnitude of the first surface reflection and subsequent reflections were more similar, which enabled a greater ability to locate the depth of a void.

There were advantages and disadvantages to using either the TDS transmission or reflection configuration. It was easier to get a smaller THz spot size onto the sample using a transmission configuration. This was primarily due to the large ratio of focal length to diameter in the parabolic mirrors and the cumbersome stages used to steer them. Custom optical parts could alleviate this problem for reflection configurations. Reflection mode is certainly a more likely candidate for a maintenance technique, as was mentioned earlier, but transmission setup could aid in the design and quality control of glass fiber composites. Reflection mode would also be a more effective technique in determining the depth of delaminations. This is due to reflection mode signals traveling a shorter distance through the attenuating glass fiber and due to the relative similarity in the

amplitude of Fresnel reflections between a void and the initial pulse. This can be easily seen when one compares the results in Figure 64 to Figure 54, which is shown again as a comparison in Figure 68. The relative amplitude of the first Fabry-Perot reflection is calculated to be an order of magnitude larger in reflection configuration than in transmission.

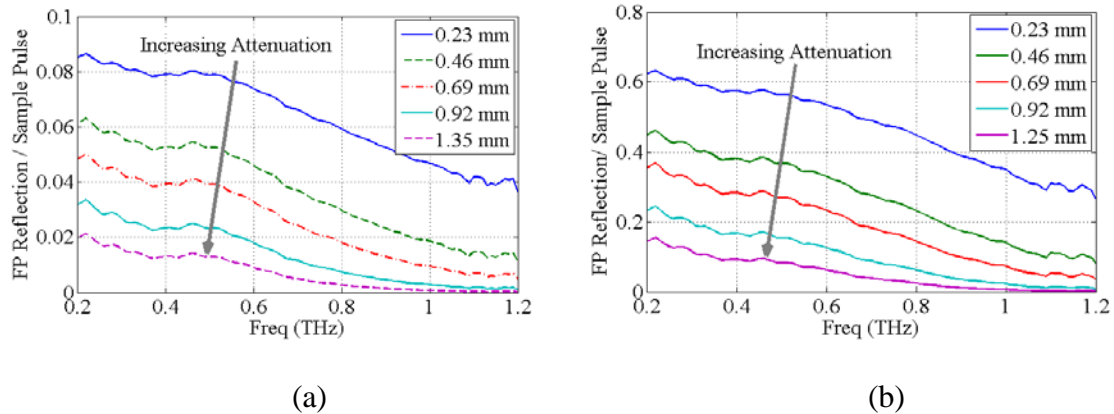


**Figure 68. Summary charts showing the relative amplitude of the first Fabry-Perot reflection to the main pulse after traveling through various thicknesses of glass fiber composite in (a) transmission configuration and (b) reflection configuration.**

Finally, a comparison of the transmission and reflection configuration images are shown next to a photograph of the damage sample in Figure 69. THz images are shown for the hidden circular void, the calibration sample using both phase and amplitude techniques, and the three burn damage areas.

### 5.3 Future Work

One of the areas of research that is currently on-going is to compare the results of THz TDS on a set of glass fiber composites samples to other NDE techniques, such as ultrasound, x-ray tomography, and thermography. This comparison could be very

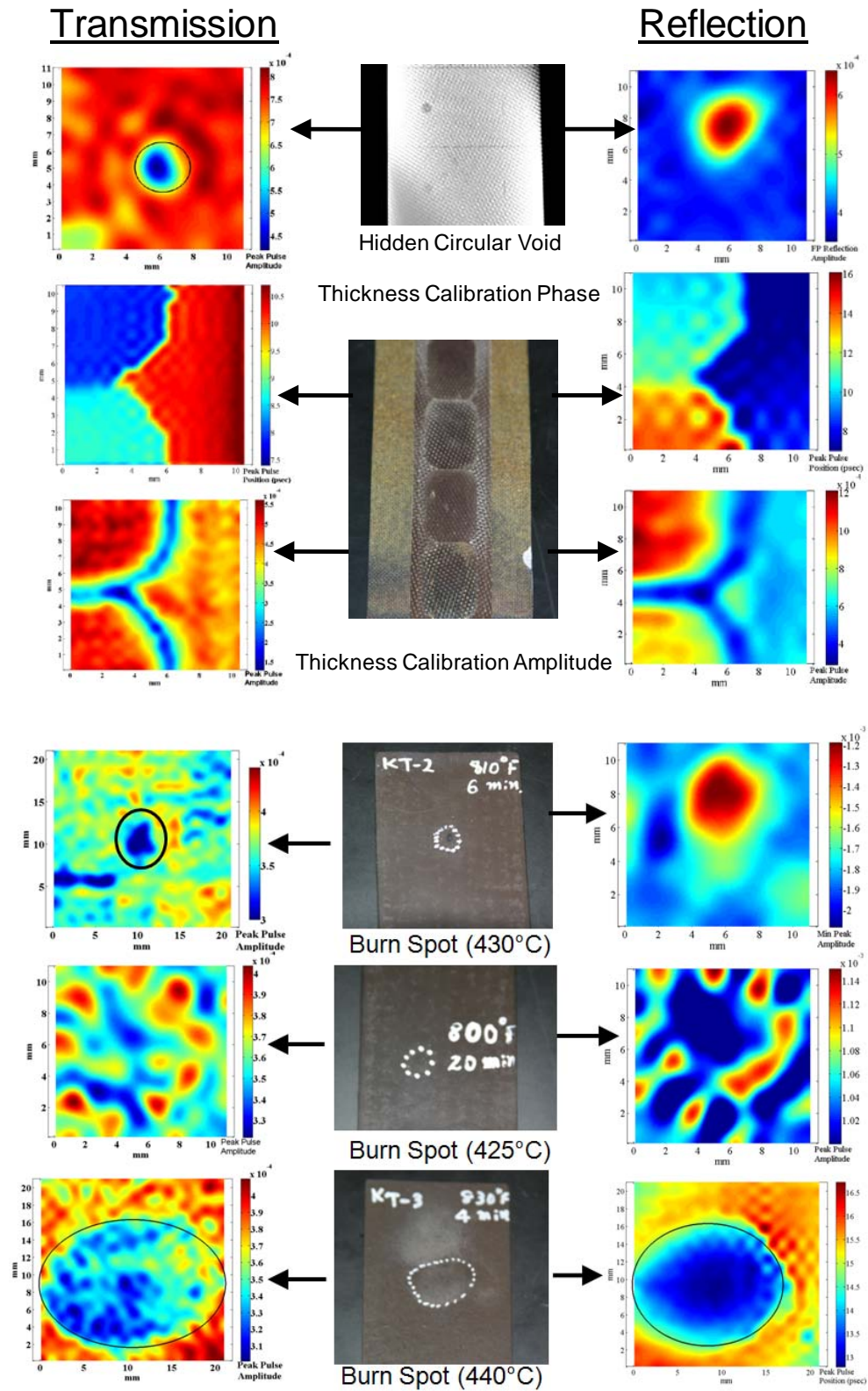


Figure 69. Comparison of various types of glass fiber damage/alterations between transmission and reflection configuration.

valuable in defining the potential strengths and weaknesses of using THz TDS for NDE of glass fiber composites. THz TDS could also be investigated as an NDE technique for two other types of composites: Kevlar and carbon fiber. The ability of THz to penetrate carbon fiber would probably be limited due to its higher conductivity, but it could be useful to determine the penetration depth and surface defects. Kevlar and glass fiber samples, with various forms of damage, are also available from AFRL/RXLP.

Another task that could be performed in future research would be to calibrate the absorption coefficient measurements with the THz TDS transmission setup. The measurements on the absorption coefficient in this dissertation appeared to be accurate, but did not explore coefficients much larger than  $0 \text{ cm}^{-1}$ . The silicon wafer or other semiconductor could be measured with THz TDS and compared to the Drude Model prediction. For this dissertation, the only types of wafers that were obtained in single quantities were those with a high resistivity. An attempt was made to find a semiconductor with a higher doping level that could be purchased in small quantities economically, but none could be located.

An area that could be explored in more detail would be the modeling of the THz pulse shape. In the laboratory, the pulse shape characteristics could be changed drastically by altering the position of any of the optics, including the parabolic mirrors and hemispherical lenses, and the alignment of the pump or probe beam on either the emitter or detector. One could characterize the effects that each of the parts of the THz quasi-optical system has on the final pulse shape and frequency spectrum. One would have to be able to isolate each component, vary the alignment, and measure the output. These measurements could then be compared to a model of the THz Gaussian pulse

shape in space and time. Perhaps the most difficult items to characterize would be the emitter and detector, and a special arrangement with their manufacturer may be required.

The analysis of the effective medium approximations could be expanded. A solid piece of the glass used in the composite would have to be obtained so that it could be accurately measured with the THz TDS transmission configuration. Then various volume concentrations of the glass and polyimide could be mixed to form different composite mixtures. The material properties of each composite mixture could then be measured and compared directly to the effective medium approximations.

One of the quantitative NDE analyses used to assess the value of the technique is to measure its resolution in detecting and identifying both surface and hidden damage. Another area of future research would be to measure damage of various sizes, shapes, and depths to define the limits of either a THz TDS transmission or reflection setup. The THz spot size would have to be minimized in either case, using short focal length optics and small translation stages. Samples would have to be prepared with defects that have been carefully manufactured and measured, and with those defects varying in size from the largest THz wavelengths down to a fraction of the smallest THz wavelengths.

Finally, the last area of suggested future research would be to design a setup in reflection mode which could accurately measure the index of refraction and absorption coefficient. The reflection technique that was used in this research was not robust or precise enough to consistently measure material parameters accurately. One would have to use an alignment system to ensure that the sample and reference were within  $1\ \mu\text{m}$  across their entire reflected surface, if the setup in Figure 29 was used. An alternate technique would be to use ellipsometry to measure the material properties in which no

reference measurement is needed. One would place a wire grid polarizer after the emitter to split the THz into s- and p- polarizations followed by a wire grid analyzer before the detector to detect the two polarizations with equal sensitivity. The sample would then be placed at an angle near the Brewster angle for a good signal-to-noise ratio, the ellipsometric angles measured and fitted, and the complex refractive index determined.



## BIBLIOGRAPHY

1. Ahn, J. S., Kim, K. H., Noh, T. W., Riu, D., Boo, K., & Kim, H. (1995). Effective-medium theories for spheroidal particles randomly oriented on a plane: application to the optical properties of a SiC whisker-Al<sub>2</sub>O<sub>3</sub> composite. *Physical Review B (Condensed Matter)*, 52(21), 15244-52.
2. Altan, H., Huang, F., Federici, J. F., Lan, A., & Grebel, H. (2004). Optical and electronic characteristics of single walled carbon nanotubes and silicon nanoclusters by terahertz spectroscopy. *Journal of Applied Physics*, 96(11), 6685-9.
3. *American Heritage Dictionary*. Second College Edition. (1982). Boston: Houghton Mifflin Company.
4. Anastasi, R. F., & Madaras, E. I. (2005). Application of hilbert-huang transform for improved defect detection in terahertz NDE of shuttle tiles. *Nondestructive Evaluation and Health Monitoring of Aerospace Materials, Composites, and Civil Infrastructure IV*, 5767 356-362. from <http://dx.doi.org/10.1117/12.600570>
5. Anastasi, R. F., & Madaras, E. I. (2006). Terahertz NDE for metallic surface roughness evaluation. *Nondestructive Evaluation and Health Monitoring of Aerospace Materials, Composites, and Civil Infrastructure V*, 6176 61760. from <http://dx.doi.org/10.1117/12.659463>
6. Aspnes, D. (1985). The accurate determination of optical properties by ellipsometry. *Handbook of Optical Constants of Solids*, E. Palik, (ed.), Orlando: Academic Press, Inc.
7. Bartel, T., Gaal, P., Reimann, K., Woerner, M., & Elsaesser, T. (2005). Generation of single-cycle THz transients with high electric-field amplitudes. *Optics Letters*, 30(20), 2805-2807.
8. Baxter, J. & Schmuttenmaer, C. (2006). Conductivity of ZnO nanowires, nanoparticles, and their films using time-resolved terahertz spectroscopy. *Journal of Chemical Physics B*, 110( 25229-25239).
9. Bakker, H. J., Cho, G. C., Kurz, H., Wu, Q., & Zhang, X. C. (1998). Distortion of terahertz pulses in electro-optic sampling. *Journal of the Optical Society of America B*, 15(6), 1795-1801.
10. Beard, M. C., Turner, G. M., & Schmuttenmaer, C. A. (2002). Terahertz spectroscopy. *Journal of Physical Chemistry B*, 106(29), 7146-7159.
11. Bolivar, P. H., Brucherseifer, M., Rivas, J. G., Gonzalo, R., Ederra, I., Reynolds, A. L., et al. (2003). Measurement of the dielectric constant and loss tangent of high

- dielectric-constant materials at terahertz frequencies. *IEEE Transactions on Microwave Theory and Techniques*, 51(4), 1062-1066.
12. Chan, W., Deibel, J., Mittleman, D. (2007). Imaging with terahertz radiation. *Reports on Progress in Physics*, 70(8), 1325-1379.
  13. Chau, K. J., Mujumdar, S., & Elezzabi, A. Y. (2005). Terahertz propagation in non-homogeneous strongly scattering media. *Terahertz and Gigahertz Electronics and Photonics IV*, 5727(1) 177-85. from <http://dx.doi.org/10.1117/12.591279>
  14. Cheville, A., Zhang, X. C., Grischkowski, D., Reiten, M. T. (2007). *THz Tutorial*. CLEO 2007 THz Workshop.
  15. Clancy, T., Pieczenik S., (1996). *Games of State*. New York: Penguin Putnam.
  16. Cooney, A., & Blackshire, J. L. (2006). Advanced imaging of hidden damage under aircraft coatings. *Advanced Sensor Technologies for Nondestructive Evaluation and Structural Health Monitoring II*, 6179 617902. from <http://dx.doi.org/10.1117/12.659035>
  17. Dai, J., Zhang, J., Zhang, W., & Grischkowski, D. (2004). Terahertz time-domain spectroscopy characterization of the far-infrared absorption and index of refraction of high-resistivity, float-zone silicon. *Journal of the Optical Society of America B*. 21(7), 1379-85.
  18. Department of Defense. *Military Handbook: Polymer Matrix Composites Utilization of Data*. Mil-Hdbk-17-3D. Washington: GPO, 25 Feb 1994.
  19. Diels, J. C., & Rudolph, W. (2006). *Ultrashort Laser Pulse Phenomena*. New York: Academic Press.
  20. Dikmelik, Y., Spicer, J. B., Fitch, M. J., & Osiander, R. (2006). Effects of surface roughness on reflection spectra obtained by terahertz time-domain spectroscopy. *Optics Letters*, 31(24), 3653-5.
  21. Dobroiu, A., Yamashita, M., Ohshima, Y., Morita, Y., Otani, C., & Kawase, K. (2004). Terahertz imaging system based on a backward-wave oscillator. *Applied Optics*. 5637-5646.
  22. Dorney, T., Johnson, J., Mittleman, D., & Baraniuk, R. (2000). Imaging with THz pulses. *Proceedings of 7th IEEE International Conference on Image Processing*, 1 764-7. from <http://dx.doi.org/10.1109/ICIP.2000.901071>
  23. Dorney, T. D., Baraniuk, R. G., & Mittleman, D. M. (2001). Material parameter estimation with terahertz time-domain spectroscopy. *Journal of the Optical Society of America A (Optics, Image Science and Vision)*, 18(7), 1562-71.

24. Duvillaret, L., Garet, F., & Coutaz, J. L. (1999). Highly precise determination of optical constants and sample thickness in terahertz time-domain spectroscopy. *Applied Optics*, 38(2), 409-15.
25. Duvillaret, L., Garet, F., Coutaz, J. L., & Whitaker, J. F. (1997). A reliable method for the extraction of material parameters of thick and thin samples in THz time-domain spectroscopy. *13 (ISBN 1 55752 486 6)*, 248-51.
26. Ekspla. Laser Spectroscopy. (2007). Terahertz Spectroscopy Kit Brochure. Vilnius, Lithuania. <http://www.ekspla.com/en/main/products/84?pid=525>
27. Fletcher, J. R., Swift, G. P., Dai, D. C., Levitt, J. A., & Chamberlain, J. M. (2007). Propagation of terahertz radiation through random structures: An alternative theoretical approach and experimental validation. *Journal of Applied Physics*, 101(1), 013102.
28. Fletcher, J. R., Swift, G. P., Dai, D., & Chamberlain, J. M. (2007). Pulsed terahertz signal reconstruction. *Journal of Applied Physics*, 102(11), 113105-1.
29. Garcia-Vidal, F. J., Pitarke, J. M., & Pendry, J. B. (1997). Effective medium theory of the optical properties of aligned carbon nanotubes. *Physical Review Letters*, 78(22), 4289-92.
30. Gornov, E., Peiponen, K. E., Svirko, Y., Ino, Y., & Kuwata-Gonokami, M. (2006). Efficient dispersion relations for terahertz spectroscopy. *Applied Physics Letters*, 89(14), 142903-1.
31. Hoffmann, M. C., Yeh, K., Hwang, H. Y., Sosnowski, T. S., Prall, B. S., Hebling, J., & Nelson, K. A. (2008). Fiber laser pumped high average power single-cycle terahertz pulse source. *Applied Physics Letters*, 93(14), 141107-1.
32. Holst, G. C. (1998). *Sampling, Aliasing, and Data Fidelity for Electronic Imaging Systems, Communications, and Data Acquisition*. Winter Park, FL: JCD Publishing.
33. Hu, B. B., & Nuss, M. C. (1995). Imaging with terahertz waves. *Optics Letters*, 20(16), 1716-18.
34. Jackson, J. B., Mourou, M., Whitaker, J. F., Duling III, I. N., Williamson, S. L., Menu, M., & Mourou, G. A. (2007). Terahertz imaging for non-destructive evaluation of mural paintings. *Optics Communications* 281 527-532.
35. Jepsen, P. U., Fischer, B. M. (2005). Dynamic range in terahertz time-domain transmission and reflection spectroscopy. *Optics Letters*. 30(1). 29-31.
36. Jepsen, P. U., Jensen, J. K., & Moller, U. (2008). Characterization of aqueous alcohol solutions in bottles with thz reflection spectroscopy. *Optics Express*, 16(13), 9318-9331.

37. Jian, Z., & Mittleman, D. M. (2006). Characterization of guided resonances in photonic crystal slabs using terahertz time-domain spectroscopy. *Journal of Applied Physics*, 100(12), 123113-1.
38. Jian, Z., Pearce, J., & Mittleman, D. M. (2005). Two-dimensional photonic crystal slabs in parallel-plate metal waveguides studied with terahertz time-domain spectroscopy. *Semiconductor Science and Technology*, 20(7), 300-6.
39. Jian, Z., Pearce, J., & Mittleman, D. M. (2004). Defect modes in photonic crystal slabs studied using terahertz time-domain spectroscopy. *Optics Letters*, 29(17), 2067-2069.
40. Jordens, C., Koch, M. (2008). Detection of foreign bodies in chocolate with pulsed terahertz spectroscopy. *Optical Engineering* 47(3),037003-1.
41. Kang, C., Maeng, I. H., Oh, S. J., Lim, S. C., An, K. H., Lee, Y. H., et al. (2007). Terahertz optical and electrical properties of hydrogen-functionalized carbon nanotubes. *Physical Review B (Condensed Matter and Materials Physics)*, 75(8), 85410-1.
42. Kerker, M. (1969). *The Scattering of Light and other Electromagnetic Radiation*. London: Academic Press.
43. Kubota, T., Talekar, P., Sudarshan, T. S., Ma, X., Parker, M., & Ma, Y. (2002). An automated defect detection system for silicon carbide wafers. *IEEE SoutheastCon 2002*, 42-47. from <http://dx.doi.org/10.1109/SECON.2002.995555>
44. Kuzel, P., Nemeč, H., Kadlec, F., Duvillaret, L., & Coutaz, J. L. (2006). Independent determination of the complex refractive index and wave impedance by time-domain terahertz spectroscopy. *Optics Communications*, 260(1), 175-83.
45. Lee, S. (2008). Scattering by a dense layer of infinite cylinders at normal incidence. *Journal of the Optical Society of America A*, 25(5), 1022-1029.
46. Ma, X., Parker, M., & Sudarshan, T. S. (2002). Nondestructive defect delineation in SiC wafers based on an optical stress technique. *Applied Physics Letters*, 80(18), 3298-300.
47. Maeng, I., Kang, C., Oh, S. J., Son, J. H., An, K. H., & Lee, Y. H. (2007). Terahertz electrical and optical characteristics of double-walled carbon nanotubes and their comparison with single-walled carbon nanotubes. *Applied Physics Letters*, 90(5), 51914-1.
48. Mittleman, D. (2003). Terahertz imaging. *Sensing with terahertz radiation*. D. Mittleman (ed.), New York: Springer.

49. Myroshnychenko, V. & Brosseau, C. (2008). Effective complex permittivity of two-phase random composite media: a test of the two exponent phenomenological percolation equation. *Journal of Applied Physics*, 103(8), 084112-1.
50. Na, J. K. (2005). Ultrasonic inspection of thin high performance composite structures. *Review of Progress in Quantitative Nondestructive Evaluation*, 28, AIP Conference Proceedings.
51. Naftaly, M. & Miles, R. H. (2007). Terahertz time-domain spectroscopy of silicate glasses and the relationship to material properties. *Journal of Applied Physics*. 102(043517), 1-6.
52. Naftaly, M. & Miles, R. E. (2007). A method for removing etalon oscillations from thz time-domain spectra. *Optics Communications*, 280, 291-295.
53. Nemec, H., Kuzel, P., Garet, F., & DuVillaret, L. (2004). Time-domain terahertz study of defect formation in one-dimensional photonic crystals. *Applied Optics*, 43(9), 1965-1970.
54. Oh, S. J., Kang, C., Maeng, I., Son, J., Cho, N. K., Song, J. D., et al. (2007). Measurement of carrier concentration captured by InAs/GaAs quantum dots using terahertz time-domain spectroscopy. *Applied Physics Letters*, 90(13), 131906.
55. Pearce, J. & Mittleman, D. (2002). Scale model experimentation: using terahertz pulses to study light scattering. *Physics in Medicine and Biology*. 47, 3823-30.
56. Pearce, J., Jian, Z., & Mittleman, D. M. (2004). Propagation of terahertz pulses in random media. *Philosophical Transactions of the Royal Society London, Series A (Mathematical, Physical and Engineering Sciences)*, 362(1815), 301-14.
57. Pearce, J., Jian, Z., & Mittleman, D. M. (2005). Bayesian approach to non-Gaussian field statistics for diffusive broadband terahertz pulses. *Optics Letters*. 30(21), 2843-5.
58. Pearce, J., Doyle, K., Jian, Z., Deibel, J., & Mittleman, D. M. (2006). Nonstationary time-domain statistics of multiply scattered broadband terahertz pulses. *Journal of the Optical Society of America B*, 23(8), 1506-10.
59. Piesiewicz, R., Kleine-Ostmann, T., Krumbholz, N., Mittleman, D., Koch, M., & Kurner, T. (2005). Terahertz characterisation of building materials. *Electronics Letters*, 41(18), 1002-4.
60. Piesiewicz, R., Jansen, C., Mittleman, D., Kleine-Ostman, T., Koch, M., Kurner, T. (2007). Scattering analysis for the modeling of thz communication systems. *IEEE Transactions on Antennas and Propagation*, 55(11), 3002-3009.

61. Pupeza, I., Wilk, R., & Koch, M. (2007). Highly accurate optical material parameter determination with THz time-domain spectroscopy. *Optics Express*, 15(7), 4335-4350.
62. Redo-Sanchez, A., Karpowicz, N., Xu, J., Zhang, X.C. (2006). Damage and defect inspection with terahertz waves. *The 4<sup>th</sup> Annual Workshop on Ultrasonic and Advanced Methods for Nondestructive Testing and Material Characterization*, 67-77. from [www.ndt.net](http://www.ndt.net)
63. Reiten, M. T., Hess, L., & Cheville, R. A. (2006). Nondestructive evaluation of ceramic materials using terahertz impulse ranging. *Advanced Sensor Technologies for Nondestructive Evaluation and Structural Health Monitoring II*, 6179-617905. from <http://dx.doi.org/10.1117/12.657734>
64. Rutz, F., Koch, M., Khare, S., & Moneke, M. (2005). Quality control of polymeric compounds using terahertz imaging. *Terahertz and Gigahertz Electronics and Photonics IV*, 5727(1) 115-22. from <http://dx.doi.org/10.1117/12.590301>
65. Rutz, F., Hasek, T., Koch, M., Richter, H., Ewert, U. (2006). Terahertz birefringence of liquid crystal polymers. *Applied Physics Letters* 89(22), 221911.
66. Rutz, F., Koch, M., Khare, S., Moneke, M., Richter, H., & Ewert, U. (2006). Terahertz quality control of polymeric products. *International Journal of Infrared and Millimeter Waves*, 27(4), 547-56.
67. Sakai, K. (2005). *Terahertz optoelectronics*. Berlin; Kobe: Springer; NiCT, National Institute of Information and Communications Technology.
68. Selig, H., Khazan, M., & Wilke, I. (2000). Optical properties of glasses and ceramics for terahertz-technology. *2000 Conference on Lasers and Electro-Optics Europe*, 1. from <http://dx.doi.org/10.1109/CLEOE.2000.909935>
69. Sengupta, A., Bandyopadhyay, A., Bowden, B. F., Harrington, J. A., & Federici, J. F. (2006). Characterization of olefin copolymers using terahertz spectroscopy. *Electronics Letters*, 42(25), 1477-1479.
70. Seo, M. A., Lee, J. W., & Kim, D. S. (2006). Dielectric constant engineering with polymethylmethacrylate-graphite metastate composites in the terahertz region. *Journal of Applied Physics*, 99(6), 66103-1.
71. Shen, Y. C., Taday, P. F., Pepper, M. (2008). Elimination of scattering effects in spectral measurement of granulated materials using terahertz time domain spectroscopy. *Journal of Applied Physics*, 92(5), 051103-1.
72. Siegman, A. M., (1986). *Lasers*. Stanford University: University Science Books.

73. Sze, S. M., (1985). *Semiconductor Devices: Physics and Technology*. Hoboken, NJ: John Wiley & Sons, Inc.
74. Tuncer, E., Bowler, N., & Youngs, I. J. (2006). Application of the spectral density function method to a composite system. *Physica B*, 373(2), 306-12.
75. Wang, S., & Zhang, X. C. (2004). Pulsed terahertz tomography. *Journal of Physics D: Applied Physics*, 37(4), 1-36.
76. Wietzke, S., Jansen, C., Rutz, F., Mittleman, D., Koch, M. (2007). Determination of additive content in polymeric compounds with terahertz time-domain spectroscopy. *Polymer Testing*, 26, 614-618.
77. Wietzke, S., Jordens, C., Krumbholz, N., Baudrit, B., Bastian, M., Koch, M. (2007). Terahertz imaging: a new non-destructive technique for the quality control of plastic weld joints. *Journal of the European Optical Society*, 2, 07013-1.
78. Wikipedia. <http://en.wikipedia.org/wiki>
79. Withayachumnankul, W., Ferguson, B., Rainsford, T., Mickan, S. P., & Abbott, D. (2005). Material parameter extraction for terahertz time-domain spectroscopy using fixed-point iteration. *Photonic Materials, Devices, and Applications*, 5840(1) 221-31. from <http://dx.doi.org/10.1117/12.612946>
80. Withayachumnankul, W., Ferguson, B., Rainsford, T., Mickan, S. P., & Abbott, D. (2005). Simple material parameter estimation via terahertz time-domain spectroscopy. *Electronics Letters*, 41(14), 800-1.
81. Wu, D.H., & Meyer, J.R. (2004). Terahertz emission, detection and military applications. *Terahertz for Military and Security Applications II*, 5411 187-195.
82. Xin, X., Altan, H., Saint, A., Matten, D., & Alfano, R. R. (2006). Terahertz absorption spectrum of para and ortho water vapors at different humidities at room temperature. *Journal of Applied Physics*, 100(9), 094905-1.
83. Xu, J., Plaxco, K. W., Allen, S. J. (2006). Absorption spectra of liquid water and aqueous buffers between 0.3 and 3.72 THz. *The Journal of Chemical Physics*. 124(036101), 1-3.
84. Xu, J., Zhong, H., Yuan, T., Xie, X., Wang, S., Zhang, X. C., et al. (2004). T-rays identify defects in insulating-materials. *Conference on Lasers and Electro-Optics (CLEO)*, 1 2 pp. vol.1.
85. Xu, X., Wang, X., & Wang, L. (2006). Deviation of optical constants extracted in terahertz transmission spectroscopy. *Applied Optics*, 45(4), 648-652.

86. Yariv, A., & Yeh, P., (1984). *Optical Waves in Crystals, Propagation and Control of Laser Radiation*. Wiley-Interscience.
87. Yasui, T., Yasuda, T., Sawanaka, K., & Araki, T. (2005). Terahertz paintmeter for noncontact monitoring of thickness and drying progress in paint film. *Applied Optics*, 44(32), 6849-56.
88. You, D., Jones, R.R., Bucksbaum, P.H., & Dykaar, D.R., "Generation of High-Power Sub-Single-Cycle 500-Fs Electromagnetic Pulses," *Optics Letters* **18**, 290-292 (1993).
89. Younossi, O., Kennedy, M., Graser, J.C., Military Airframe Costs: The Effects of Advanced Materials and Manufacturing Process. RAND Corporation, 2001.
90. Yuan, T., Liu, H. B., Xu, J. Z., Al-Douseri, F., Hu, Y., & Zhan, X. C. (2003). THz time-domain spectroscopy of atmosphere with different humidity. *Terahertz for Military and Security Applications. Proceedings of SPIE*. 5070, 28-57.
91. Zhang, J. & Grischkowski, D. (2004). Terahertz time-domain spectroscopy study of silica aerogels and adsorbed molecular vapors. *Journal of Physical Chemistry B*. 108, 18590-18600.
92. Zhong, H., Xu, J., Xie, X., Yuan, T., Reightler, R., Madaras, E., et al. (2005). Nondestructive defect identification with terahertz time-of-flight tomography. *IEEE Sensors Journal*, 5(2), 203-8.
93. Zimdars, D., White, J., Stuk, G., Chernovsky, A., Fichter, G., & Williamson, S. (2006). Large area terahertz imaging and non-destructive evaluation applications. *The 4<sup>th</sup> Annual Workshop on Ultrasonic and Advanced Methods for Nondestructive Testing and Material Characterization*, UMass Dartmouth, N. Dartmouth, MA.



## Vita

Christopher D. Stoik graduated from Rice Lake High School in Rice Lake, Wisconsin in 1989. He attended the United States Air Force Academy and graduated with a BS Physics in 1993. He was immediately commissioned a second lieutenant in the U.S. Air Force and attended the Air Force Institute of Technology (AFIT) at Wright Patterson AFB, OH, receiving an MS Electrical Engineering in 1995. Lt Stoik then moved to Offutt AFB, NE and joined the 513<sup>th</sup> Engineering and Test Squadron as an electronic warfare reprogramming engineer for the B-1B. His unit was dissolved and relocated to Eglin AFB, FL as the 36<sup>th</sup> Electronic Warfare Squadron in 1997, where he continued producing operational electronic warfare mission data for the B-1 and B-2 defensive systems.

In 2000, Captain Stoik joined the Joint STARS program office at Hanscom AFB, MA as the chief of the advanced technology section. He joined the AWACS program office at Hanscom in 2002, becoming the chief of the advanced surveillance sensors branch. In 2004, Major Stoik moved to Wright Patterson AFB, OH, where he joined AFRL Sensors Directorate as the Signature Center Lead for the automatic target recognition division. He returned to AFIT in 2005 to complete his PhD Physics.

<b>REPORT DOCUMENTATION PAGE</b>				<i>Form Approved OMB No. 074-0188</i>	
<p>The public reporting burden for this collection of information is estimated to average 1 hour per response, including the time for reviewing instructions, searching existing data sources, gathering and maintaining the data needed, and completing and reviewing the collection of information. Send comments regarding this burden estimate or any other aspect of the collection of information, including suggestions for reducing this burden to Department of Defense, Washington Headquarters Services, Directorate for Information Operations and Reports (0704-0188), 1215 Jefferson Davis Highway, Suite 1204, Arlington, VA 22202-4302. Respondents should be aware that notwithstanding any other provision of law, no person shall be subject to a penalty for failing to comply with a collection of information if it does not display a currently valid OMB control number.</p> <p><b>PLEASE DO NOT RETURN YOUR FORM TO THE ABOVE ADDRESS.</b></p>					
<b>1. REPORT DATE (DD-MM-YYYY)</b> 12-10-2008		<b>2. REPORT TYPE</b> AFIT PhD Dissertation		<b>3. DATES COVERED (From – To)</b> 25 Aug 2005 – 28 Dec 2008	
<b>4. TITLE AND SUBTITLE</b>  <b>Nondestructive Evaluation of Aircraft Composites Using Terahertz Time Domain Spectroscopy</b>				<b>5a. CONTRACT NUMBER</b>	
				<b>5b. GRANT NUMBER</b>	
				<b>5c. PROGRAM ELEMENT NUMBER</b>	
<b>6. AUTHOR(S)</b>  Christopher D. Stoik, Lt Col, USAF				<b>5d. PROJECT NUMBER</b>	
				<b>5e. TASK NUMBER</b>	
				<b>5f. WORK UNIT NUMBER</b>	
<b>7. PERFORMING ORGANIZATION NAMES(S) AND ADDRESS(S)</b> Air Force Institute of Technology Graduate School of Engineering and Management (AFIT/EN) 2950 Hobson Way Wright Patterson AFB OH 45433-7765				<b>8. PERFORMING ORGANIZATION REPORT NUMBER</b>  AFIT/DS/ENP/09-D02	
<b>9. SPONSORING/MONITORING AGENCY NAME(S) AND ADDRESS(ES)</b> James L. Blackshire, Ph.D. Nondestructive Evaluation Branch Air Force Research Laboratory Materials and Manufacturing Directorate Wright Patterson AFB, OH 45433-7750				<b>10. SPONSOR/MONITOR'S ACRONYM(S)</b>	
				<b>11. SPONSOR/MONITOR'S REPORT NUMBER(S)</b>	
<b>12. DISTRIBUTION/AVAILABILITY STATEMENT</b> APPROVED FOR PUBLIC RELEASE; DISTRIBUTION UNLIMITED					
<b>13. SUPPLEMENTARY NOTES</b>					
<b>14. ABSTRACT</b> Terahertz (THz) time domain spectroscopy (TDS) was assessed as a nondestructive evaluation technique for aircraft composites. Material properties of glass fiber composite were measured using both transmission and reflection configuration. The interaction of THz with a glass fiber composite was then analyzed, including the effects of scattering, absorption, and the index of refraction, as well as effective medium approximations. THz TDS, in both transmission and reflection configuration, was used to study composite damage, including voids, delaminations, mechanical damage, and heat damage. Measurement of the material properties on samples with localized heat damage showed that burning did not change the refractive index or absorption coefficient noticeably; however, material blistering was detected. Voids were located by THz TDS transmission and reflection imaging using amplitude and phase techniques. The depth of delaminations was measured via the timing of Fabry-Perot reflections after the main pulse. Evidence of bending stress damage and simulated hidden cracks was also detected with terahertz imaging.					
<b>15. SUBJECT TERMS</b>					
<b>16. SECURITY CLASSIFICATION OF:</b>		<b>17. LIMITATION OF ABSTRACT</b>  UU	<b>18. NUMBER OF PAGES</b>  161	<b>19a. NAME OF RESPONSIBLE PERSON</b> Matthew J. Bohn, Lt Col, USAF	
REPORT U	ABSTRACT U			c. THIS PAGE U	<b>19b. TELEPHONE NUMBER (Include area code)</b> (937) 255-3636 x4573 Matthew.Bohn@afit.edu

**Standard Form 298 (Rev. 8-98)**

Prescribed by ANSI Std. Z39-18